
# Investigating the exoplanetary atmosphere of HAT-P-30 b

**Nandini Jain**
University of Potsdam

A thesis submitted for the degree of
Master of Science
in Astrophysics

Supervised by:
**Dr. Henri M. J. Boffin**
**Dr. Jiri Zak**
**Prof. Dr. Katja Poppenhaeger**

# Declaration

I hereby declare that the submitted Master's thesis is my work and that, to the best of my knowledge, it contains no sources or resources other than the ones mentioned and acknowledged. During the writing of the thesis, I indicated all quotes, citations, and references that were taken from published or unpublished publications, such as books, journals, academic articles, newspapers, reports, etc. Furthermore, the research described in this thesis is based on work conducted at the European Southern Observatory (ESO) and no part of this thesis has been submitted elsewhere for any other degree or qualification.

# Acknowledgements

I want to express my heartfelt gratitude to my supervisors, Dr. Henri M. J. Boffin, Dr. Jiri Zak, and Prof. Dr. Katja Poppenhaeger, for their invaluable guidance and encouragement throughout this journey. Thank you to Dr. Jiri Zak for his unwavering support and mentorship, which have significantly shaped my progress. His patience and insightful advice have meant so much to me.

My deepest appreciation goes to my parents and Ronak. Your trust, constant support, and unconditional love have been my strength at every step. You are my foundation, and I am endlessly thankful for all you do. I love you!

To Joy, thank you for being my family away from home. Your presence through all my highs and lows has been a source of immense comfort, and I truly cannot express my gratitude enough. I also want to thank Shital Di and Shubham Jiju for being my other family in Germany. Your kindness and affection have made a profound impact on my life, and I feel incredibly fortunate to have you.

Bhavesh, I am grateful for your friendship and encouragement over the years. From our undergraduate days to now, you have always been there to motivate and support me, and I deeply appreciate everything you have done.

I owe much to my incredible friends who made my time in Munich unforgettable. To Akashi, Dhairya, Khyati, Darshana, Neeraj, Surya, Prabhanjan, Simran, and the Gujarati Gang, as well as the Garba Group – thank you for filling this chapter of my life with laughter. And Khushi, thank you for literally bringing "khushi" into my life. I'm so lucky to have found such wonderful people to share this journey with.

A big thank you to Dr. Nikoloy for helping me with the WASP-96 b analysis and to Dr. Eva Maria for your guidance on using Tiberius through email. While our interactions were brief, your insights were valuable and much appreciated.

Finally, to everyone who has been a part of this journey, whether directly or indirectly, thank you. This thesis would not have been possible without you all, and I am deeply grateful.

There are infinite worlds both like and unlike this world of ours. For the atoms being infinite in number are borne on far out into space.

– **Epicurus, 341 - 270 BC**

# Zusammenfassung

Die Charakterisierung der Atmosphären von Exoplaneten ist entscheidend, um ihre Natur zu verstehen und Hinweise auf ihre Entstehung und Entwicklung zu erhalten. Die Transmissionsspektroskopie vergleicht Spektren, die innerhalb und außerhalb von Transits aufgenommen wurden, um planetare Signale zu extrahieren. Die niederauflösende Transmissionsspektroskopie ($R \leq 1000$ - 2000) liefert hochfrequente Spektren mit einem hohen Signal-Rausch-Verhältnis. Durch die Untersuchung der Abhängigkeit der Transit-Tiefe von der Wellenlänge können atmosphärische Absorber identifiziert und die Zusammensetzung bestimmt werden, während die Steigung des Spektrums auf das Vorhandensein von Dunst hinweisen kann.

Ich präsentiere eine spektrophotometrische Analyse der Atmosphäre von HAT-P-30 b unter Verwendung von archivierten FORS2-Daten des Very Large Telescope, um mit einem niederauflösenden Transmissionsspektrum nach starken Absorbern oder Rayleigh-Streuung zu suchen. HAT-P-30 b ist ein Hot Jupiter mit geringer Dichte und großer Skalenhöhe und daher ein ideales Ziel für die Transmissionsspektroskopie aufgrund des erwarteten starken atmosphärischen Signals. Die Daten von WASP-96 b aus FORS2 wurden ebenfalls analysiert, um als Referenz für die Untersuchung von HAT-P-30 b zu dienen. Die atmosphärische Charakterisierung wurde mithilfe theoretischer Modelle aus dem PetitRADTRANS durchgeführt.

Diese Studie ergab ein relativ strukturloses Transmissionsspektrum, ohne signifikante Nachweise für Natrium- (Na) oder Kalium- (K) Absorptionsmerkmale, entgegen vorheriger Annahmen. Das Fehlen starker Absorber deutet auf das Vorhandensein hoch gelegener Wolken in der Atmosphäre hin. Während die von Modellen vorhergesagten Hauptmerkmale nicht beobachtet wurden, zeigen diese Ergebnisse, dass Exoplanetenatmosphären komplexer sind als erwartet, und unterstreichen die Notwendigkeit präziserer Beobachtungen. Tiefere Einblicke in die Atmosphäre von HAT-P-30 b werden durch zukünftige Forschungen mit Weltraumteleskopen wie JWST und Ariel möglich sein. Dies wird unser Verständnis von Exoplanetenatmosphären vorantreiben und letztendlich helfen, die Ursprünge von Hot Jupiters besser zu verstehen.

# Abstract

Characterizing the atmospheres of exoplanets is essential to understanding their nature and providing clues about their formation and evolution. Transmission spectroscopy compares spectra taken inside and outside transits to extract planetary signals. Low-resolution transmission spectroscopy ($R \leq 1000$ - 2000) provides high-cadence, signal-to-noise spectra. By studying the transit depth's dependence on wavelength, we can identify atmospheric absorbers and determine the composition, while the spectrum slope can indicate the presence of haze.

I present a spectrophotometric analysis of HAT-P-30 b's atmosphere using archival FORS2 data from the Very Large Telescope using a low-resolution transmission spectrum to search for strong absorbers or Rayleigh scattering. HAT-P-30 b is a hot Jupiter with low density and a large scale height, making it an ideal target for transmission spectroscopy due to its expected strong atmospheric signal. WASP-96 b data from FORS2 was also analyzed as a reference for the analysis of HAT-P-30 b. The atmospheric characterization was performed using theoretical models from the PetitRADTRANS.

This study revealed a relatively featureless transmission spectrum, with no significant detection of sodium (Na) or potassium (K) absorption features, contrary to previous assumptions. The absence of strong absorbers suggests the presence of high-altitude clouds in the atmosphere. While major spectral features predicted by models were not observed, these results show that exoplanetary atmospheres are more complex than expected and highlight the need for more precise observations. Deeper insights into the atmosphere of HAT-P-30 b will be possible through future research using space telescopes like JWST and Ariel. This will advance our understanding of exoplanet atmospheres and, ultimately, help us understand the origins of hot Jupiters.

# Contents

# Abbreviations/Acronymns

| | |
|---|---|
| **AO** | adaptive optics |
| **cdd** | cross-dispersion displacement |
| **CoRoT** | Convection, Rotation and planetary Transits |
| **DO** | Data Organiser |
| **ELT** | Extremely Large Telescope |
| **ESA** | European Space Agency |
| **ESO** | European Southern Observatory |
| **EsoReflex** | ESO Recipe flexible execution workbench |
| **FORS2** | FOcal Reducer/low dispersion Spectrograph 2 |
| **FoV** | Field of View |
| **FWHM** | full width at half maximum |
| **GIARPS** | GIAno (0.97-2.4 micron) and haRPS (0.38-0.70 micron) |
| **GP** | Gaussian processes |
| **HARPS** | High Accuracy Radial velocity Planet Searcher |
| **HAT** | Hungarian-made Automated Telescope |
| **HATNet** | Hungarian-made Automated Telescope Network |
| **HST** | Hubble Space Telescope |
| **IAU** | International Astronomical Union |
| **JWST** | James Webb Space Telescope |
| **MCMC** | Markov chain Monte Carlo |
| **METIS** | Mid-infrared ElT Imager and Spectrograph |
| **OCA** | OrganisationClassificationAssociation |
| **PDI** | polarimetric differential imaging |
| **PI** | Principal Investigator |
| **PSF** | point spread function |
| **ras** | rotation angle axis |
| **RV** | radial velocity |

| | |
|---|---|
| **SNR** | signal-to-noise ratio |
| **SPECULOOS** | Search for habitable Planets EClipsing ULtra-cOOl Stars |
| **SPHERE** | Spectro-Polarimetric High-contrast Exoplanet Research |
| **STIS** | Space Telescope Imaging Spectrograph |
| **TESS** | Transiting Exoplanet Survey Satellite |
| **TNG** | Telescopio Nazionale Galileo |
| **VLT** | Very Large Telescope |
| **WASP** | Wide Angle Search for Planets |

# Chapter 1

# Introduction

## 1.1 Definition of a planet

For an object to be considered a planet, it needs to meet the following conditions according to the International Astronomical Union (IAU) (Ekers, 2018):

- orbits the Sun,
- has sufficient mass to assume a nearly spherical shape and
- has cleared its orbit of other objects in the neighbourhood[1].

However, exoplanets - planets that orbit stars other than the Sun - do not yet have an official IAU definition. When an object

- has a mass or maximum mass up to 13 times that of Jupiter (based on the burning of deuterium),
- is not freely floating,
- has a mass ratio with the central object below the $L_4/L_5$ instability
- has been confirmed by sufficient observational data, and
- has findings published in peer-reviewed journals,

it is considered an exoplanet, according to the IAU (Des Etangs and Lissauer, 2022), (see also Schneider et al., 2011).

## 1.2 The First Discovery

Since the earliest days of civilization, humans have been driven by an innate desire to explore the unknown and to venture into uncharted territories. This spirit of discovery has propelled us beyond the boundaries of our home planet, inspiring us to reach for the celestial bodies that dot the night sky. Reflecting this quest, the European Space Agency (ESA)'s Cosmic Vision[2] campaign includes four key scientific questions (Clavel, 2009):

[1] IAU 2006 General Assembly: Result of the IAU Resolution votes, accessed October 31, 2024
[2] https://www.esa.int/Science_Exploration/Space_Science/ESA_s_Cosmic_Vision

- What are the conditions for planet formation and the emergence of life?
- How does the Solar System work?
- What are the fundamental physical laws of the universe?
- How did the universe originate, and what is it made of?

Two of these are directly linked to planetary science, emphasizing the central role of exoplanets in understanding the broader mysteries of the universe.

The first discovery of extra-solar planets was made by Wolszczan and Frail (1992) using the pulsar timing method. They discovered not one, but two planets orbiting the pulsar **PSR B1257+12**. The first exoplanet (**51 Pegasi b**) orbiting around a main sequence star was discovered by using the radial velocity (RV) method, which searches for fluctuations in a star's motion caused by the gravitational attraction of a neighboring planet (Mayor and Queloz, 1995)[3]. 51 Pegasi b is a gas giant comparable in size to Jupiter, with an orbital period of four days (see Figure 1.3). These aforementioned findings challenged the prevailing belief that planets could only exist around main-sequence stars and that giant planets could only exist in larger orbits. Interestingly, the latter discovery supported the idea that gas giants could be discovered close to their sun (Phillips, 1963). Four more years later, Henry et al. (1999) and Charbonneau et al. (1999) observed the first exoplanet transit of HD 209458 b, which turned out again to be a Jupiter-like exoplanet, but with an orbit of only 3.5 years. This not only set a new milestone in exoplanet detection but also firmly confirmed that the gas giants can be found orbiting their host stats very closely. Following these breakthroughs, the exploration of exoplanets has emerged as one of the most exciting and pivotal areas of research in modern astronomy.

Since this initial detection, exoplanet research has flourished with more than 5000 confirmed exoplanets in almost three decades[4]. Accessible data has led to rapid growth in various subfields like planetary formation theories, population studies, climate modelling, atmospheric analysis, etc.

The transit method has become the most effective way to find exoplanets, accounting for about 75% of all detections as of August 2024. This success is largely due to ground-based surveys like (Wide Angle Search for Planets (WASP), Pollacco et al., 2006), (Hungarian-made Automated Telescope Network (HATNet), Bakos et al., 2004), and space missions such as Kepler (Borucki et al., 2010), and (Transiting Exoplanet Survey Satellite (TESS), Ricker et al., 2015). Interestingly, with about 2,778 confirmed exoplanets to date[5] — compared to about 190 from WASP[6] - Kepler has dominated transit detections. The Kepler mission led to a significant increase in exoplanet discoveries around 2016, as seen in Figure 1.1. This figure shows the cumulative number of discoveries over time, categorized by detec-

[3]This led to half of the 2019 Nobel Prize in Physics, shared with James Peebles
[4]As of August 16, 2024, the NASA Exoplanet Archive reports over 5,747 confirmed exoplanets.
[5]Kepler candidates, accessed January 10, 2025
[6]WASP discoveries

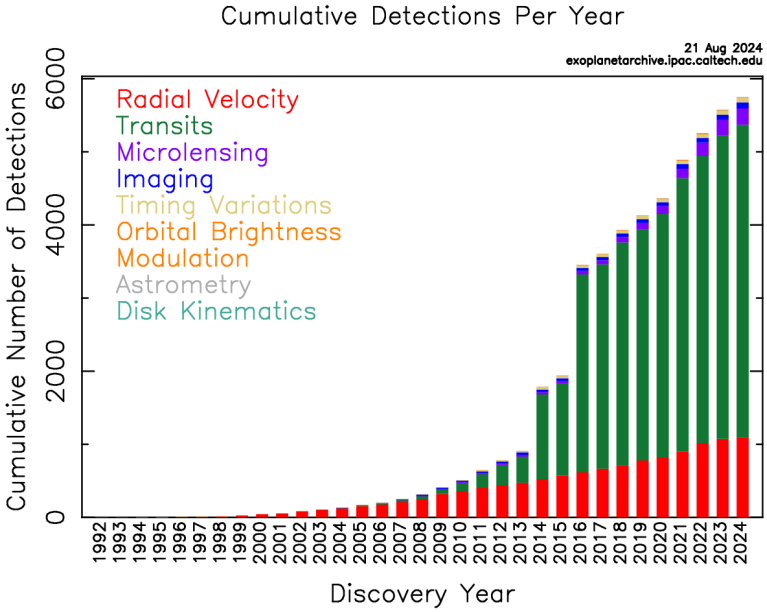


Figure 1.1: Cumulative number of exoplanets detected per year, split up by individual detection methods. Early exoplanet detections were dominated by the RV method, but the Kepler mission shifted the focus to the transit method, enabling the discovery of thousands of distant planets.
**Note:** 'Timing Variations' includes transit, pulsar, and pulsation timing variations.
©NASA Exoplanet Archive (August 21, 2024)

tion method. The following sections introduce each detection method in more detail.

## 1.3 Planet Types

Gas giants like Jupiter (318 Earth masses/$M_\oplus$) have an uppermost layer of a thick hydrogen-helium (H/He) envelope that was accumulated from the protoplanetary nebula (Fortney, 2024). Exoplanet detection also shows the existence of "sub-Saturns" or "super-Neptunes" (about 20-75 $M_\oplus$), where the mass of the H/He envelope is equivalent to the total metallic content (including the core and the envelope). H/He only makes up around 10–20% of the mass of Neptune and Uranus, which are around 15 $M_\oplus$. Even smaller planets, referred to as "sub-Neptunes" or "mini-Neptunes", have a H/He envelope that makes up only 0.1–5% of their mass, making them roughly 2-3 $R_\oplus$ (Earth radius) in size and 5–10 $M_\oplus$ in mass. The Kepler mission discovered that sub-Neptunes are more common than Neptune-mass or Jupiter-mass planets, at least for orbits shorter than 100 days. Furthermore, according to planet formation theory, the metallicity of a planet's H/He atmosphere is inversely related to its mass. This is in line with what we see in the four giant planets of the solar system (Fortney et al., 2013), with Jupiter having the lowest metallicity, at about three times that of the Sun.

The primary H-dominated atmospheres of planets evolve to atmospheres rich in $H_2O$ (possibly with liquid water layers underneath, creating "water worlds"), $CO_2$

(like Venus and Mars), or $N_2$ (like Earth). This transformation happens at specific points in the mass-temperature spectrum (mainly around 5 $M_\oplus$, though this varies) (Madhusudhan et al., 2014). In contrast to primary H/He atmospheres, these "secondary atmospheres" are frequently outgassed from the planet's interior. The boundary between primary and secondary atmospheres is well-defined in the solar system, but they may not be as clear among sub-Neptunes, which may have hybrid atmospheres or none at all. Irrespectively, they are also called as "Super-Earths." Understanding the diversity of exoplanetary atmospheres helps us better understand how planets form and put our solar system in a broader cosmic context.

There are now several different types of exoplanetary atmospheres accessible for study: Hot Jupiters with equilibrium temperatures (T) $\approx$ 1500 K, ultra-hot Jupiters (T $>$ 2000 K) with 10–100 times the radiation of normal hot Jupiters (Baxter et al., 2020), hot Neptunes (T $\approx$ 700–1200 K), and cooler Super-Earths (T $\approx$ 500 K). Despite having orbits different from those of the planets in our solar system, many of these exoplanets provide useful comparison points for elemental composition (e.g., hydrogen, carbon, oxygen). Interestingly, the ratios of carbon to oxygen (C/O) and oxygen to hydrogen (O/H) are hard to measure for the gas giants in our solar system due to cooler temperatures causing condensation and cloud cover obscuring key molecules (Madhusudhan, 2012). In contrast, these ratios are more straightforward to determine for hot Jupiters, where high temperatures keep the molecules in gaseous form, making them more accessible to spectroscopic detection and providing information on elemental distributions outside our planetary neighborhood.

## 1.4 Planet Formation and Evolution

Planets are formed from the star's protoplanetary disk. Thus, the composition of the disk, as well as the location and evolution of its formation, are intrinsically linked to the interior as well as atmospheric composition of exoplanets. The nebular theory, which was first put forth by Kant in 1755, postulates that planets are formed from circumstellar material. During the first 10 million years of the formation of the Sun 4.57 billion years ago[7] (Connelly et al., 2012), before the circumstellar disc dissipated, gas giants formed, and approximately 100 million years later, terrestrial planets formed (Montmerle et al., 2006)

According to core accretion, planet formation is a bottom-up process in which tiny planetesimals combine within the protoplanetary disk. Runaway gas accretion starts when a core reaches about 10 $M_\oplus$ and lasts until the disk dissipates or the surrounding gas is exhausted (Pollack et al., 1996; Ikoma et al., 2000; Inaba et al., 2003). With larger gas giants located farther from the Sun and more minor rocky planets closer to it, this model describes well how the planets are arranged in the

[7]This age is derived from meteorite radioactive dating.

solar system (Pollack et al., 1996). Nonetheless, there are challenges in understanding the early creation of rings and gaps seen in young systems like IRS 63 due to the long durations needed in core accretion (Segura-Cox et al., 2020).

Gravitational instability is a scenario of rapid planet formation in which massive regions of a protoplanetary disk split apart into clumps due to instability. Without the more prolonged gas accretion phase needed in core accretion models, these fragments produce massive planets by contraction of these clumps under their gravity. This process only takes place in sufficiently massive disks, based on the Toomre stability criterion (Toomre, 1964; Boss, 1997). Gravitational instability allows planet formation in a few thousand years, as compared to millions of years for core accretion (Mamajek, 2009; Gammie, 2001). It can explain the eventual migration of enormous gas giants to shorter orbits and is particularly helpful in explaining their existence at large orbital distances.

The discovery of exoplanets, such as hot Jupiters, super-Earths, and warm Neptunes, was not only surprising as it challenged our earlier beliefs of planet formation, but also gave us the opportunity to broaden our planet formation understanding. In order to contemplate the origins of hot Jupiters, three main theories were put forward to explain the origins of hot Jupiters: disc migration, in-situ formation, or eccentric migration through tidal interactions (Dawson and Johnson, 2018) (see Figure 1.2).

### 1.4.1 Disc migration

Disc migration occurs as planets interact with the protoplanetary disc, causing shifts in their orbits due to angular momentum exchange with the gas. Due to this exchange through stellar tides or the presence of a magnetocavity formed by the stellar magnetic field (Lin et al., 1996; Rice et al., 2008), migrating planets can halt in the hot Jupiter region before being tidally disrupted or absorbed by the star. The final location is determined by the conditions of the disc, such as the magnetic field, mass loss, tidal interactions, viscosity, scale height, etc. (Ahrer, 2023).

Type I migration plays a crucial role for less massive planets, such as Earth-sized or Neptune-sized, which create density waves in the disc. Usually, this leads to migration inwards, although, under certain circumstances, outward migration is possible. Type II migration is fuelled by the disc's viscous evolution and involves massive planets capable of carving gaps due to the exchange of angular momentum with the disc, and they migrate more slowly. The transition between these two modes is not sharply defined (D'Angelo et al., 2006). The orbital locations of planets such as hot Jupiters can be explained by disk migration since their observed semi-major axes match those predicted by migration models (Nelson et al., 2017). However, disc migration requires precise initial conditions to align with observations (Dawson

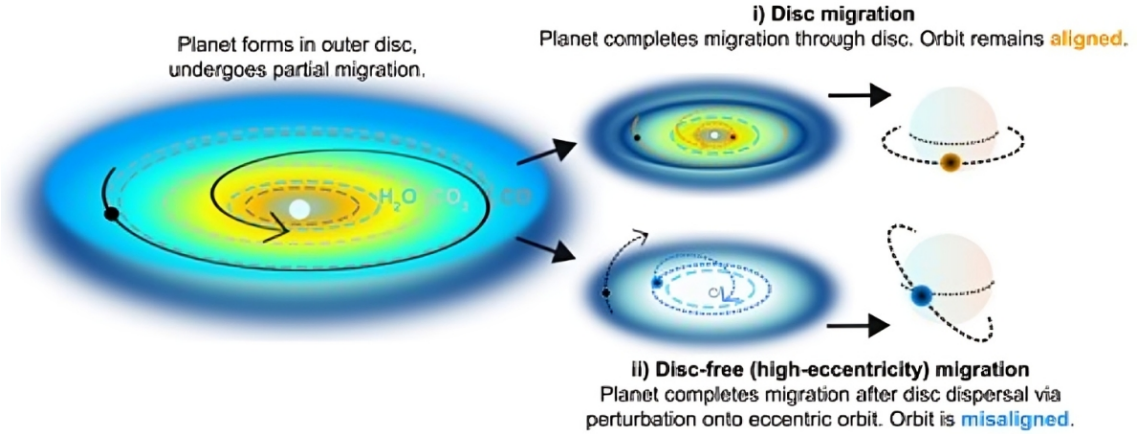


Figure 1.2: The schematic illustrates that a planet may follow one of two migration pathways after disc dispersal: **Disc Migration**, where it is formed in the outer disc, migrates inward through ice lines, and accretes oxygen-rich solids from the inner disc; or **High-Eccentricity Migration**, where it is perturbed into an eccentric orbit and later circularized by tidal forces, without accreting inner-disc material. These mechanisms account for variations in atmospheric composition and orbital alignment. Image taken from Kirk et al. (2024).

and Johnson, 2018).

### 1.4.2 In-situ formation

In-situ formation proposes that hot Jupiters form in their current, short-period orbits. The process is theoretically supported by core accretion, but forming the planetary core requires a significant accumulation of material. This is considered challenging because the solid formation is more efficient beyond the snow lines in the protoplanetary disc, where conditions favor the condensation of ice and other materials (Schlichting, 2014; Lee and Chiang, 2016). As a result, there is no firm agreement on whether hot Jupiters may form in situ through core accretion; this question might be resolved by a more thorough understanding of solids in the planetary disk (Dawson and Johnson, 2018). Gravitational instability is not possible in such close-in orbits. In some regions, the gas cannot cool sufficiently to allow fragment formation without rotational disruption. Furthermore, the gas would escape the star's gravity due to the high temperatures and gas densities needed (Rafikov, 2005). These challenges make in-situ formation a debated and uncertain process.

### 1.4.3 Disc-free migration

After the protoplanetary disc disperses, gravitational interactions with another body, such as a planet, star, or disc remnants, drive high-eccentricity migration. A planet may be forced into an extremely eccentric orbit by these interactions. Over time, tidal forces during close approaches to the host star dissipate orbital energy, circularizing the orbit and bringing the planet closer to the star. The existence of hot Jupiters with tight orbits can be explained by this mechanism (Wu and Murray,

2003; Dawson and Johnson, 2018). While disk migration happens over the disc's lifetime, high-eccentricity migration can happen at any stage, even later on, when an external event like a stellar fly-by triggers it. As demonstrated by observations of hot Jupiters like WASP-94 Ab, this process can also cause initially aligned orbits to become misaligned, producing planets with retrograde or misaligned trajectories (Neveu-VanMalle et al., 2014).

### 1.4.4 Carbon-to-Oxygen (C/O) ratio

The carbon-to-oxygen (C/O) ratio, combined with metallicity, hints towards the understanding of planet formation and migration (Öberg et al., 2011). For molecules like $H_2O$, $CO_2$, and CO in the protoplanetary disk, it reflects the influence of snow lines. A higher C/O ratio often suggests formation beyond the CO snow line, while a lower ratio indicates formation closer to the $H_2O$ snow line, where oxygen-rich material dominates (Öberg et al., 2011).

Interpreting C/O ratios can be challenging due to processes that alter atmospheric composition, such as photochemistry and disequilibrium chemistry processes (e.g., Moses et al., 2011; Baeyens et al., 2022; Drummond et al., 2020). These effects can change the observed ratio, making it difficult to link directly to formation conditions. Additionally, the ratio of $CO/CH_4$ is beneficial in the study of gas giants as the transition is highly temperature dependent and affected by other atmospheric processes (Fortney et al., 2020). Turrini et al. (2021); Cridland et al. (2019) highlight the significance of molecules that contain C, O, and N in understanding the interior and evolution of a planet.

## 1.5 Exoplanet Detection Techniques

Finding an exoplanet is indeed a challenging task, like trying to find a shooting star in daylight since planets are extremely dim compared to their host stars. However, astronomers have developed several excellent techniques to detect these alien worlds. This section provides an overview of various exoplanet detection techniques, with a detailed focus on the transit method (see 1.5.6), which was used to discover the target exoplanets HAT-P-30 b and WASP-96 b.

### 1.5.1 Radial Velocity Method

The RV method, sometimes referred to as the Doppler technique, is an indirect technique that gauges a star's subtle wobble caused by an orbiting planet's gravitational attraction. As the star and planet orbit their common center of mass, the star's spectrum shifts periodically towards the blue or red end, depending on its motion relative to Earth. The relationship between the observed wavelength shift and the

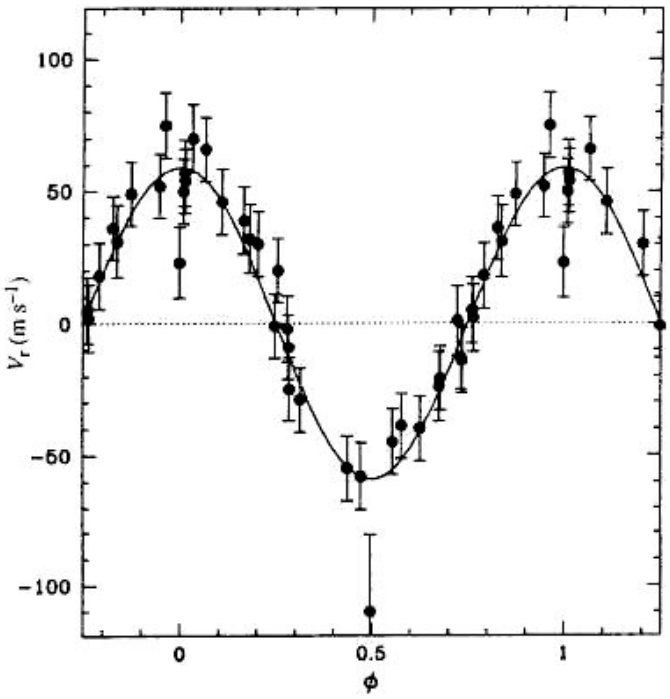


Figure 1.3: Radial velocity measurements of 51 Pegasi, folded to a 4.23 day period, obtained using the ELODIE spectrograph (Mayor and Queloz, 1995). This groundbreaking data revealed the presence of a 0.47 $M_{\rm Jup}$ minimum mass companion, marking the first detection of an exoplanet orbiting a Sun-like star.

star's radial velocity are related to each other by

$$\frac{\Delta\lambda(t)}{\lambda} = \frac{v(t)}{c}$$

where, $\Delta\lambda(t)$ is the wavelength shift, $\lambda$ is the original wavelength, $v(t)$ is the radial velocity, and $c$ is the speed of light. The radial velocity curve reveals the planet's orbital period ($P$), and the curve's shape indicates the orbital eccentricity ($e$).

The semi-amplitude ($K$) of the radial velocity curve is related to these orbital parameters through the following equation:

$$K = \left(\frac{2\pi G}{P}\right)^{\frac{1}{3}} \frac{M_{\rm P}\sin(i)}{(M_* + M_{\rm P})^{\frac{2}{3}}} \frac{1}{\sqrt{1-e^2}} \tag{1.1}$$

Here $M_{\rm P}$ is the planetary mass, $M_*$ is the stellar mass, and $G$ is the gravitational constant. If the orbital inclination ($i$) of a planet is known, we can directly calculate $M_{\rm P}$, *or* else we get constraints on $M_{\rm P}\sin(i)$. This method's ability to constrain planetary masses complements the transit technique, which measures planetary radii. Combined, these techniques allow for the computation of quantities necessary for atmospheric characterization investigations, such as surface gravity and planetary density.

1094 exoplanets have been detected with the RV method as of November 9, 2024[8]. Exoplanets, especially those with longer orbital periods and beyond 1 au, have been found using the RV technique. However, it is difficult to find smaller exoplanets because of stellar activity and rotational variability, such as spots and plages that can imitate planetary signals (Dumusque et al., 2011). Proxima Centauri b is a close Earth-like planet that has been discovered using high-resolution spectrographs like (High Accuracy Radial velocity Planet Searcher (HARPS), PHASE, 2003) in spite of difficulties (Dumusque et al., 2011; Anglada-Escudé et al., 2016). RV measurements are necessary for verifying planet candidates initially detected by the transit method, especially for planetary mass determination (Pont et al., 2005; Mayor et al., 2014). RV signals range widely, from 10 cm/s for Earth-like planets to 10–100 m/s for big planets. However, comparable RV shifts can also be caused by stellar activity, making identification more difficult and needing advanced techniques to differentiate between planetary and stellar signals (Rajpaul et al., 2015; Barragán et al., 2019). More than 400 exoplanets have been found so far, thanks to RV, including ones with long orbits like HD 222155b at 5.1 au (Boisse et al., 2012).

### 1.5.2 Direct Imaging

The most difficult yet sole technique that provides visible evidence is direct imaging, which captures snapshots of exoplanets orbiting distant stars. Planets are comparatively cooler than their parent stars and absorb light from their parent star, which they re-emit mostly as infrared waves at longer wavelengths than the star. This difference between the peak wavelengths of the light emitted from the host star and a planet helps astronomers differentiate the radiative signal between them and capture an image. The extreme contrast in brightness between exoplanets and their host stars makes direct imaging of these objects extremely difficult. The contrast between Jupiter-like planets and Sun-like stars can reach up to $10^{-9}$ in optical wavelengths and roughly $10^{-8}$ in the infrared (Traub and Oppenheimer, 2010), while brightness contrast in the infrared reaches about $10^{-5}$ to $10^{-6}$ for younger exoplanets as they still contain residual heat after formation. Therefore, even to detect nearby, young, hot, and massive exoplanets that are in the late phases of planet formation, very high spatial resolution and high contrast imaging techniques are required. In spite of these challenges, methods like point spread function (PSF) subtraction (Lagrange et al., 2009), (polarimetric differential imaging (PDI) Quanz et al., 2011) to improve planet visibility, or coronagraphy (physically blocking out starlight) with adaptive optics (AO) to account for atmospheric distortion are used, allowing us to observe faint planets at large angular separations.

Till today 82 exoplanets have been successfully imaged using this technique[9], including the first successful direct imaging of a planetary-mass object around a brown dwarf in 2004 (Chauvin et al., 2004). A significant milestone was reached

[8] NASA Exoplanet Archive
[9] November 9, 2024, NASA Exoplanet Archive

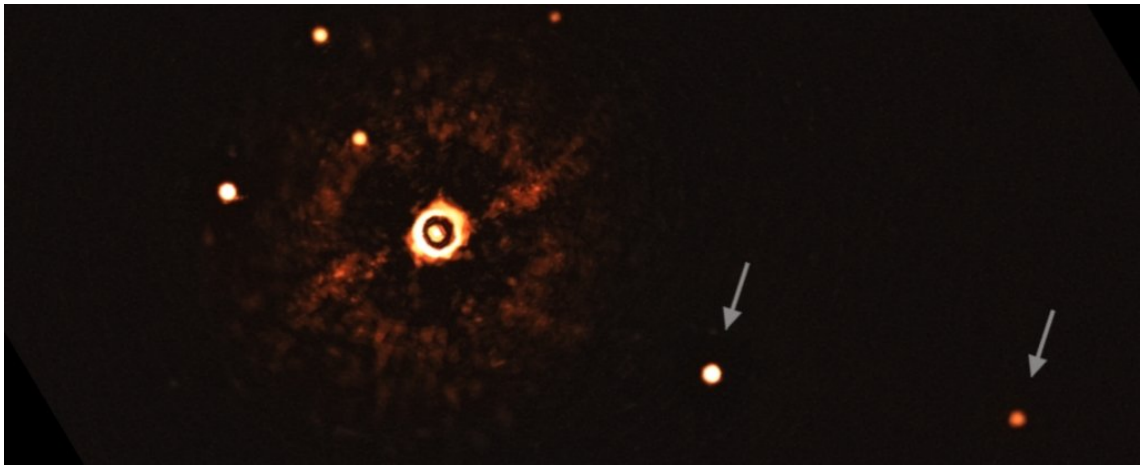

Figure 1.4: Direct image of the TYC 8998-760-1 system, captured by the VLT's Spectro-Polarimetric High-contrast Exoplanet Research (SPHERE) instrument. This image reveals two giant exoplanets TYC 8998-760-1 b and c, orbiting a Sun-like star 300 light-years away, with the star's light blocked by a coronagraph (center left). Background stars are faintly visible throughout the image. ©ESO/Bohn et al. (2020)

when the Subaru Telescope took the first image of GJ 504b, a giant planet that resembles Jupiter and orbits a G-type star that resembles the Sun (Kuzuhara et al., 2013). In the meantime, the Very Large Telescope (VLT) pushed the boundaries by imaging several planets in the same system around the young star TYC 8998-760-1 (see Figure 1.4 Bohn et al., 2020), setting a new record for precision in direct imaging of exoplanets. Further developments — like the upcoming Mid-infrared ElT Imager and Spectrograph (METIS) instrument on the Extremely Large Telescope (ELT) — promise significant improvements to detect and thoroughly investigate these far-off worlds (Quanz et al., 2015).

### 1.5.3 Gravitational Microlensing

The phenomenon of light bending as it passes through a gravitational field is used in this method. Thus, an exoplanet's gravitational field distorting a background star's light can be used to detect the exoplanet, even if it is too faint to be directly detected. Imagine that we are looking at light from a far-off source star through the lens of a foreground star. A planet orbiting this lensing star may produce a brief, extra variation in the light from the background star, resulting in a noticeable change in the flux of the source (Mao and Paczynski, 1991). The mass of the planet, the relative motion of the stars, and the angular size of the background star are some of the variables that affect this variation (Einstein, 1936), which can be seen in Figure 1.5. OGLE 2003-BLG-235/MOA 2003-BLG-53, a planet with mass 1.5 $M_{\rm Jup}$, was the first exoplanet discovered through microlensing, orbiting its star at a distance of approximately 3 au (Bond et al., 2004). This bending allows us to determine the mass of the planet .

One of the main advantages of the microlensing technique is that it can detect

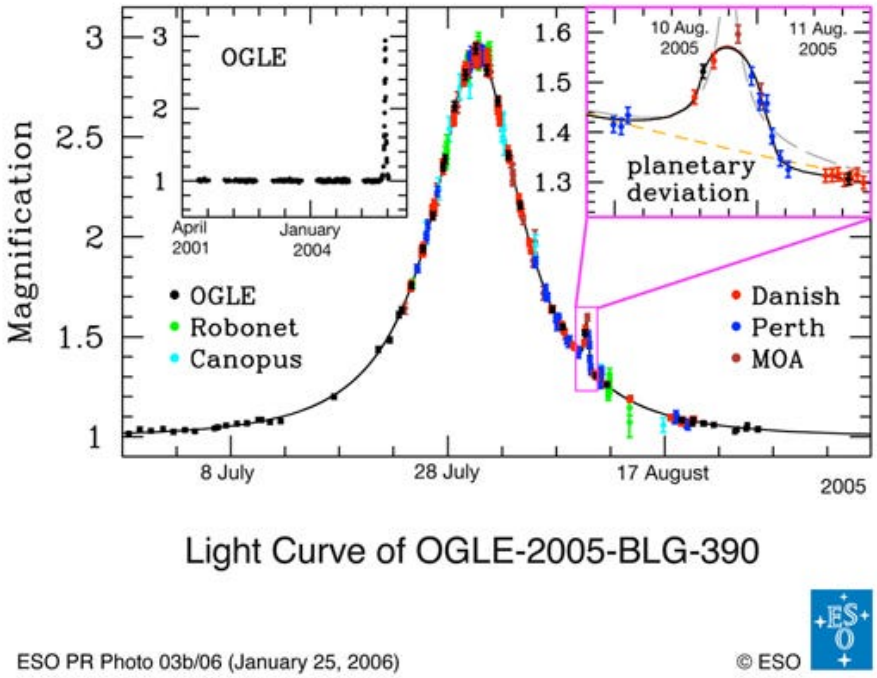


Figure 1.5: Figure displays the observed light curve of the microlensing event of planet OGLE-2005-BLG-390, using data from various global observatories. The planetary deviation and the OGLE data over a 4-year period are displayed on the top right and top left, respectively. Plot from Beaulieu et al. (2006)

planets at semi-major axes of 1 to 5 au (Beaulieu et al., 2006), which is challenging for other widely used techniques like transits or RV. It can reveal planets at long distances from the Earth, even kilo-parsecs away and along the galactic center line of sight (Tsapras, 2018). 230 exoplanets have been found by this method to date[10]. This method's disadvantage is that follow-up observations are extremely challenging because gravitational lensing events are typically non-repeatable, based on the rare alignment of a host-star-planet system in the foreground (the lens) and a background star (the source). Furthermore, degeneracies in the microlensing models can make it difficult to isolate specific parameters of the detected planet.

### 1.5.4 Astrometry

Similar to the RV method, astrometry depends on identifying a star's faint wobble brought on by an orbiting exoplanet. Astrometry measures the actual positional shift of the star on the night sky surface, whereas the RV method (section 1.5.1) detects this wobble mainly in the radial direction through changes in the star's spectral lines.

Astrometry has been very successful in supporting other detection techniques, even though it has only been used to directly discover 3 exoplanets so far[11]. The inclination of an exoplanetary system can be determined using astrometry, which

[10]November 9, 2024, NASA Exoplanet Archive
[11]November 9, 2024, NASA Exoplanet Archive

enables more accurate mass calculations of planets detected by RV measurements (e.g., McArthur et al., 2004; Benedict et al., 2006; Snellen and Brown, 2018; Benedict et al., 2022). The number of planets discovered by astrometry is projected to increase significantly with future developments, especially due to the Gaia mission (Prusti et al., 2016). During its nominal five-year mission, Gaia is/was expected to detect thousands of exoplanets up to 500 parsecs away (Perryman et al., 2014). When paired with previous RV data, data from Gaia's second data release (DR2) has already been used to improve the properties of known exoplanets (Llop-Sayson et al., 2021).

### 1.5.5 Pulsar timing

Pulsars emit extremely regular radio pulses, acting like precise cosmic clocks. When a planet orbits a pulsar, its gravity causes the pulsar to wobble slightly. This wobble affects the arrival times of the pulsar's radio pulses at Earth, making them arrive slightly earlier or later than expected. By measuring these timing variations, astronomers can infer the presence and properties of orbiting planets. In 1992, the pulsar timing technique was used to detect the first exoplanet (Wolszczan and Frail, 1992). Their formation around a neutron star indicates the survival of their host star's catastrophic formation/demise, making these planets intriguing to study. The pulsar timing method is highly sensitive and can detect planets far from their host stars. However, it requires very precise observations over long periods and can only detect relatively massive planets that cause noticeable wobbles. Despite these constraints, this technique has successfully detected 8 planets[12].

### 1.5.6 Transit method

A transit occurs when an object occults across the face of the star from our point of view. Transiting objects (planets in our case, but it can also be a stellar eclipsing binary) can overlap with a small fraction of the disc of the star, causing the star's apparent brightness to decrease slightly, as seen in Figure 1.6. This change can be measured to construct a light curve. The drop in brightness, i.e., the ratio of the observed change in flux, to that of the nominal stellar flux, is known as transit depth $\delta$ and it is proportional to the planet's size in relation to the star - in other words, the ratio of the radius of planet $R_{\rm P}$ to the stellar radius $R_{\rm S}$ squared

$$\delta \simeq \left(\frac{R_p}{R_s}\right)^2. \tag{1.2}$$

The geometry of exoplanetary systems can be better understood through transit observations. Transit durations, i.e., ingress and egress time, allow us to calculate two important parameters: the semi-major axis to star radius ratio ($a/R_{\rm S}$) and the inclination of the orbital plane ($i$) for light curve analysis. The impact parameter ($b$) (expressed as eq: 1.3) - the projected distance between the center of the star and

[12] NASA Exoplanet Archive

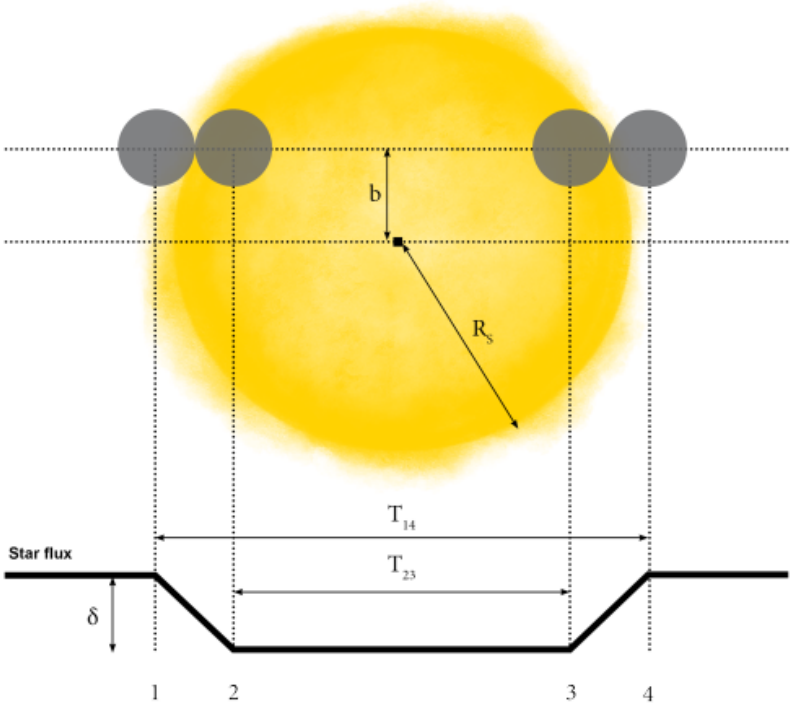


Figure 1.6: The transit light curve illustrates the characteristic dip in stellar brightness as an exoplanet passes in front of its host star. The graph depicts normalized flux over time. Points 1 and 4 mark the start of the transit as the planet begins to enter or fully exit the stellar disk. Points 2 and 3 denote the moments when the planet is fully superimposed on the stellar disk. Image taken from Ahrer (2023)

the center of the planetary disc in conjunction, is a significant factor affecting these times (see Figure 1.7). Transit durations are longer for transits with lower impact parameters (near the stellar core).

Geometrically, the impact parameter for circular orbits is defined as follows:

$$b = \frac{a\cos(i)}{R_s}. \tag{1.3}$$

The length that a planet has to travel across the disk of the star from point 1 to 4 can be written as (Figure 1.8):

$$L_{14} = 2\sqrt{(R_S + R_p)^2 - (bR_S)^2} = 2R_s\sqrt{(1+\delta)^2 - b^2}, \tag{1.4}$$

and from points 2 to 3 can be written as:

$$L_{23} = 2\sqrt{(R_S - R_p)^2 - (bR_S)^2} = 2R_s\sqrt{(1-\delta)^2 - b^2}, \tag{1.5}$$

For circular orbits, we can relate the transit duration to the orbital period using the angle traversed by the planet during transit. This angle, when compared to a full orbit, is proportional to the ratio of transit duration to orbital period:

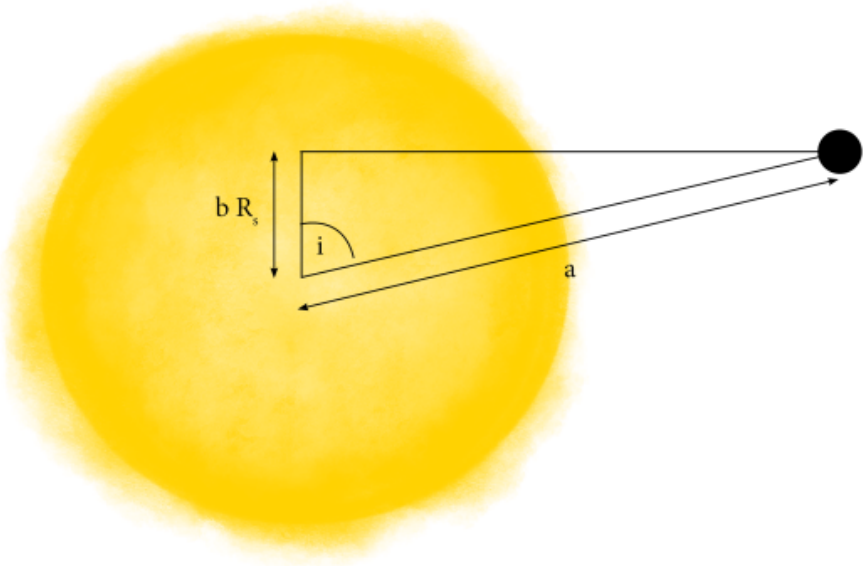


Figure 1.7: This schematic diagram illustrates the relation between the semi-major axis of the planetary orbit $a$, impact parameter $b$, and system inclination $i$. Image taken from Ahrer (2023)

$$\frac{\alpha}{2\pi} = \frac{T_{14}}{P}, \tag{1.6}$$

Here, $\alpha$ represents the angle swept by the planet between the first and fourth contact points, $T_{14}$ is the total transit duration and $P$ is the orbital period.

Geometrically, we can express $\alpha$ in terms of the chord length $L_{14}$ (the projected distance traveled by the planet across the stellar disk) and the orbital semi-major axis $a$:

$$\sin\left(\frac{\alpha}{2\pi}\right) = \frac{L_{14}}{2a}, \tag{1.7}$$

Combining these relationships and applying trigonometric identities, we can derive expressions for the transit duration $T_{14}$ (between the first and fourth contact):

$$T_{14} = \frac{P}{\pi}\arcsin\left(\frac{L_{14}/2}{a}\right) = \frac{P}{\pi}\arcsin\left(\frac{R_s}{a}\sqrt{(1+\delta)^2 - b^2}\right), \tag{1.8}$$

Similarly for the duration between the second and third contact $T_{23}$:

$$T_{23} = \frac{P}{\pi}\arcsin\left(\frac{L_{23}/2}{a}\right) = \frac{P}{\pi}\arcsin\left(\frac{R_s}{a}\sqrt{(1-\delta)^2 - b^2}\right), \tag{1.9}$$

For systems where the planetary radius is much smaller than both the stellar radius and orbital distance, we can derive an approximate formula for the scaled stellar radius:

$$\frac{a}{R_s} = \frac{2\delta^{1/4}}{\pi}\frac{P}{\sqrt{T_{14}^2 - T_{23}^2}}. \tag{1.10}$$

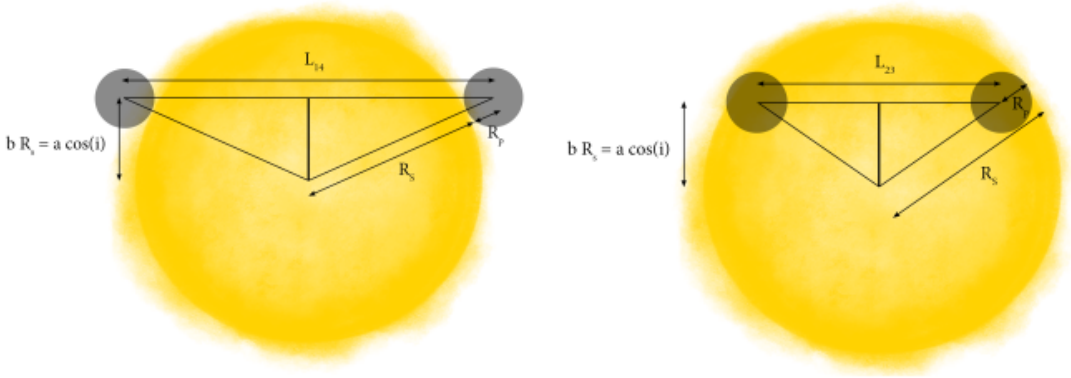


Figure 1.8: The diagram illustrates the projected transit distances $L_{14}$ and $L_{23}$ between the contact points of a transiting planet, alongside the geometric relationships between the stellar radius $R_s$, planetary radius $R_p$, and impact parameter $b$. This visual representation aids in understanding the dynamics of exoplanet transits. Image taken from Ahrer (2023)

This expression, combined with the impact parameter equation 1.3, allows us to estimate the orbital inclination. These relationships form the foundation of transit modeling, which can be further refined by incorporating stellar limb darkening effects (Ahrer, 2023).

## 1.6 Limb darkening

Let us assume a uniformly bright stellar disc, where $F$ is the stellar flux, $L_\star^{IT}$ and $L_\star^{OT}$ are the in-transit and out-of-transit luminosity, respectively, and $R_\star$ and $R_p$ are the stellar and planetary radii, $T_\star$ is the temperature of the star and $\sigma_{SB}$ denotes the Stefan-Boltzmann constant. Under this simplified model of stellar flux during a planetary transit, the transit depth $\delta$ can be approximated as:

$$\delta \simeq \left(\frac{\Delta F^2}{F^2}\right)^2 \simeq \frac{L_\star^{OT} - L_\star^{IT}}{L_\star^{OT}} \simeq \frac{4\pi R_\star^2 \sigma_{SB} T_\star^4 - 4\pi\left(R_\star^2 - R_p^2\right)\sigma_{SB} T_\star^4}{4\pi R_\star^2 \sigma_{SB} T_\star^4} \simeq \left(\frac{R_p}{R_s}\right)^2. \tag{1.11}$$

this simplification fails to capture the true nature of stellar brightness distribution. In reality, stars exhibit a phenomenon known as limb darkening, where the apparent brightness decreases from the center towards the edge of the stellar disc (Hellier et al., 2014; Heller, 2019).

Limb darkening occurs when an observer's line of sight encounters the stellar atmosphere at varying angles. Near the limb, the line of sight passes through shallower regions of the stellar atmosphere, reaching optical depth unity sooner than at the center. Consequently, we observe cooler, dimmer regions at the star's edge compared to its center (seen in Figure 1.9 with an example of the Sun). This effect is especially noticeable at shorter wavelengths due to the steeper gradient of the

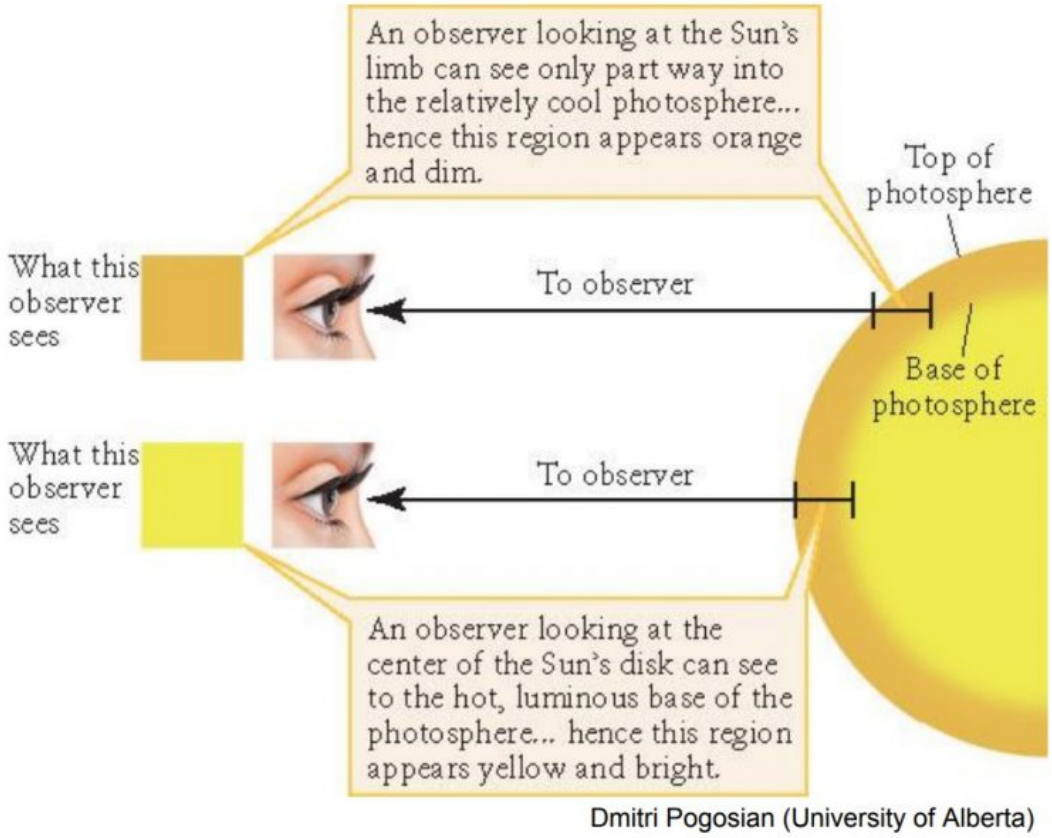


Figure 1.9: Diagram shows the observed limb darkening effect at the edge of the Sun. ©Dmitri Pogosian, University of Alberta.

blackbody spectrum. Spectroscopic light curves of the transit of WASP-39 b, as captured by JWST's NIRSpec/PRISM are shown in Figure 1.10 taken from Rustamkulov et al. (2023), indicating variations in limb darkening across the wavelength range from 0.46 to 5.71 µm.

The star's limb darkening must be taken into account when modeling the planetary transits. To account for limb darkening, various mathematical models or simple parameterized "limb-darkening laws" are typically used, and these are fitted alongside the transit light curve. Common laws include the linear, quadratic, square-root, and non-linear (four-parameter) formulations. The intensity due to limb darkening is typically expressed as a function of the angle $\theta$, which represents the angle between the observer's line of sight and the normal to the stellar surface. This intensity, $I(\theta)$, is defined relative to the intensity at the center of the stellar disk, $I(0)$, and is influenced by wavelength-dependent coefficients (denoted $u_1$ through $u_4$). These coefficients modify the brightness as follows:

1. Linear law:
$$I(\theta) = I(0)\,(1 - u_1(1 - \mu))$$

2. Quadratic law:
$$I(\theta) = I(0)\left(1 - u_1(1 - \mu) - u_2(1 - \mu^2)\right)$$

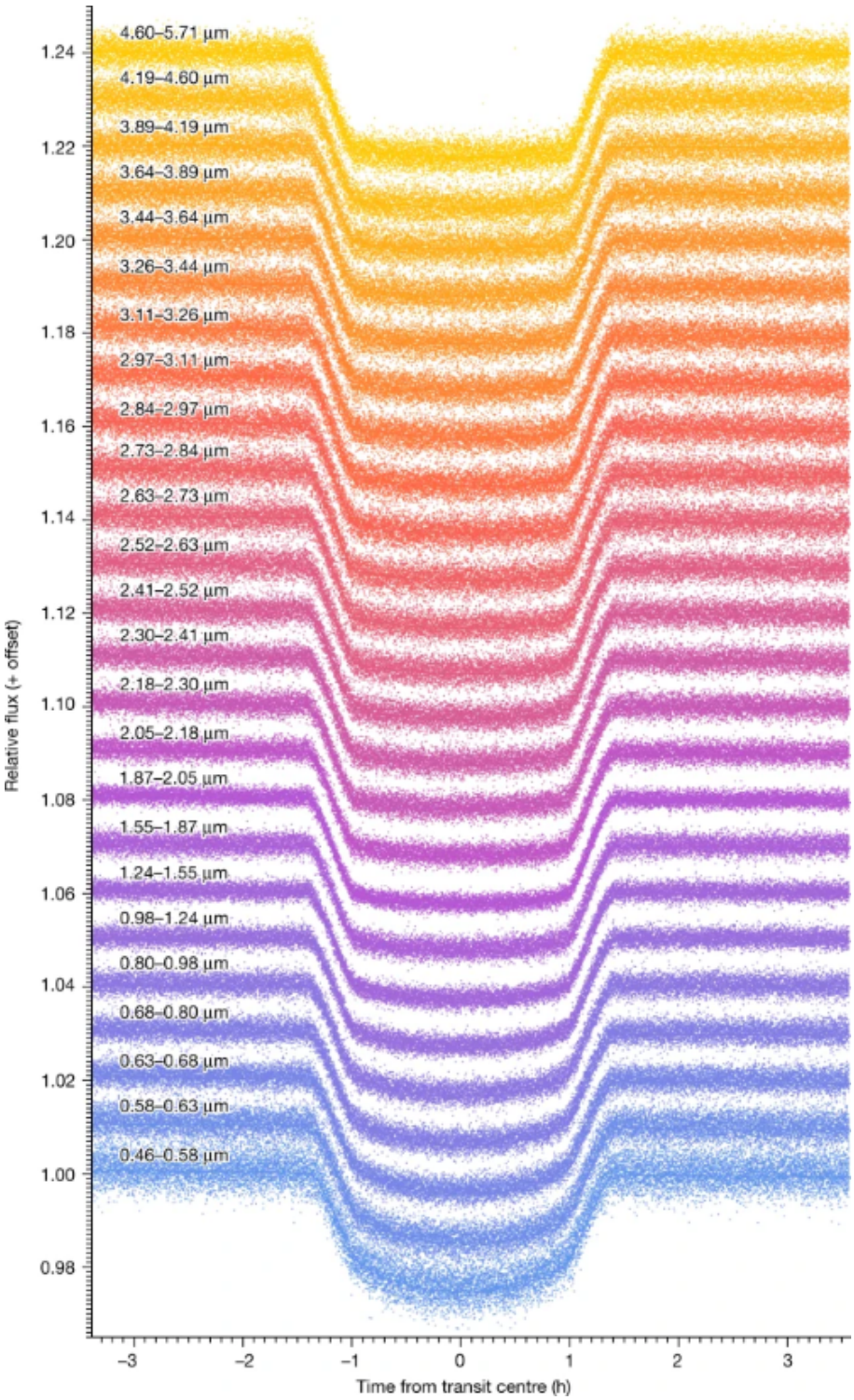


Figure 1.10: Figure taken from Rustamkulov et al. (2023) illustrates the effects of stellar limb darkening on transit observations on the individual spectroscopic transit light curves of the hot Jupiter WASP-39 b, observed across a broad wavelength range (0.46 to 5.71 µm) using JWST's NIRSpec/PRISM instrument. At shorter (bluer) wavelengths, the transit light curves exhibit more noticeable bending during the ingress and egress phases. This is due to the stronger limb-darkening effect at these wavelengths, where the star appears brighter at its center and darker at its edges. In contrast, the light curves at longer (redder) wavelengths show a more box-like shape with steeper ingress and egress slopes.

3. Square-root law:

$$I(\theta) = I(0)\left(1 - u_1(1-\mu) - u_2(1-\sqrt{\mu})\right)$$

4. Non-linear law:

$$I(\theta) = I(0)\left(1 - u_1(1-\mu) - u_2(1-\sqrt{\mu}) - u_3(1-\mu^{2/3}) - u_4(1-\mu^2)\right)$$

Here $\mu = \cos\theta$ and the coefficients ($u_1$ to $u_4$) are used to fit the observed brightness variations across the star's disk. When selecting a limb-darkening model, a key consideration is computational efficiency. For instance, the non-linear and square-root models are more computationally intensive than the simpler quadratic model. As a result, the quadratic law is often favored for its balance of simplicity and accuracy, although it is essential to monitor any correlations between the chosen limb-darkening model and the transit depth to ensure accuracy.

In practice, limb-darkening coefficients are often generated using stellar atmosphere models, and these values can be used to inform the fitting process. This can involve using uniform or Gaussian priors based on the generated values, or even fixing certain coefficients during the fitting process, as was done in some of the studies presented in this work. However, fixing all limb-darkening parameters can lead to inaccuracies, as pointed out by Csizmadia et al. (2013); Espinoza and Jordán (2015). Another useful approach to fitting limb-darkening parameters is the Kipping parametrization (Kipping, 2013). This method reformulates the quadratic limb-darkening law to reduce the risk of non-physical parameter combinations and minimize degeneracies between the two parameters, $u_1$ and $u_2$. The new parameters are defined as:

$$q_1 = (u_1 + u_2)^2 \quad \text{and} \quad q_2 = 0.5u_1(u_1 + u_2)$$

Rustamkulov et al. (2023) successfully applied this parametrization in the study of the exoplanet WASP-39 b.

## 1.7 Exoatmospheres and their characterization

Exoatmospheres/Exoplanetary atmospheres are a gaseous envelope of the planet. The study of exoatmospheres was initially proposed as a way to find life before the first exoplanet around a main sequence star was discovered (Léger et al., 1994). According to Seager and Sasselov (2000), an observer positioned on Earth could deduce the existence of an atmosphere on a transiting planet by looking at the imprint of absorption superimposed on the stellar flux that passes through the planet's atmosphere. The hypothesis was fueled by transit observations of HD 209458 b, a hot Jupiter planet (Henry et al., 1999), where detectable changes in the transit depth could result from the increased absorbing capacity of certain species, indicating their potential presence. Since then, this topic has (section 1.8) evolved

into a branch of exoplanetary research and it is also the fundamental topic of this work. Spectroscopic measurements made during transits of exoplanets have been used in several of these studies. However, researchers additionally use alternative techniques, like direct imaging and the analysis of variations in light's emission and reflection brought on by orbital motions to understand the planet's atmospheres. These different approaches can work together, as they probe various layers of the atmosphere at different wavelengths.

Three potential temperature profiles resulting from various atmospheric processes are shown in Figure 1.11. A profile of a highly irradiated planet with thermal inversion — where temperature rises with altitude - is represented by the red line. Thermal inversions can also be observed in Earth's atmosphere. Temperatures in Earth's troposphere typically drop with altitude, but under some circumstances, like quiet nights with little wind, a layer of cooler air can be trapped beneath a layer of warmer air. This prevents vertical mixing and may cause pollutants to accumulate, which causes smog in cities. Chemicals such as TiO and VO are believed to absorb visible and ultraviolet light from the host star strongly. This heats the upper atmosphere, causing thermal inversions in hot Jupiters (Madhusudhan, 2019; Hubeny et al., 2003). In contrast, there are also weakly irradiated planets or irradiated planets without thermal inversion.

High radiation exposure causes atmospheric escape at the outermost, low-pressure layers, leaking away lighter elements into space. The low-density environment directly below promotes photochemical reactions, including the formation of new compounds and the photo-dissociation of molecules into atomic components. Clouds and hazes, as well as areas where temperature inversions take place, are found farther into the atmosphere and are both strongly related to the atmospheric composition. Exoplanetary transmission spectra are affected by clouds and hazes in two main ways:

- they tend to reduce the spectral features of prominent chemical species (Deming et al., 2013), and
- they produce detectable slopes in the visible to near-infrared part.

This happens because short wavelengths are more efficiently scattered by small haze particles, producing a slope that either resembles or differs from Rayleigh scattering. Furthermore, cloud influence has been determined in some reflection spectra (Evans et al., 2013; Martins et al., 2015) and optical phase curves of transiting exoplanets (e.g., Demory et al., 2013; Shporer and Hu, 2015; Muñoz and Isaak, 2015; Parmentier et al., 2016).

Finally, because of the high temperature and pressure at the innermost areas of the atmosphere, the conditions are favorable for chemical equilibrium. Equilibrium chemistry is a commonly accepted assumption for exoplanetary atmospheres, though studies like Baxter et al. (2020) have pointed out exceptions. This equilib-

rium mainly arises from the atmosphere's attempt to minimize its potential energy, which, with enough time and stable conditions, leads to a stable chemical composition unless it is impacted by external factors. Every layer and chemical species in an exoplanet's atmosphere can be seen in different electromagnetic spectrum regions. Because of their rotational and vibrational transitions, molecules like $H_2O$, CO, $CO_2$, and $CH_4$ absorb light mainly in the infrared. Atomic species, such as Na, K, Fe, and O, have a tendency to absorb in the ultraviolet and optical spectrum, especially in the uppermost layers of the atmosphere (Madhusudhan, 2019). For a more thorough understanding of the chemical and physical composition of exoplanetary atmospheres, multiwavelength observations offer a useful means of investigating these environments.

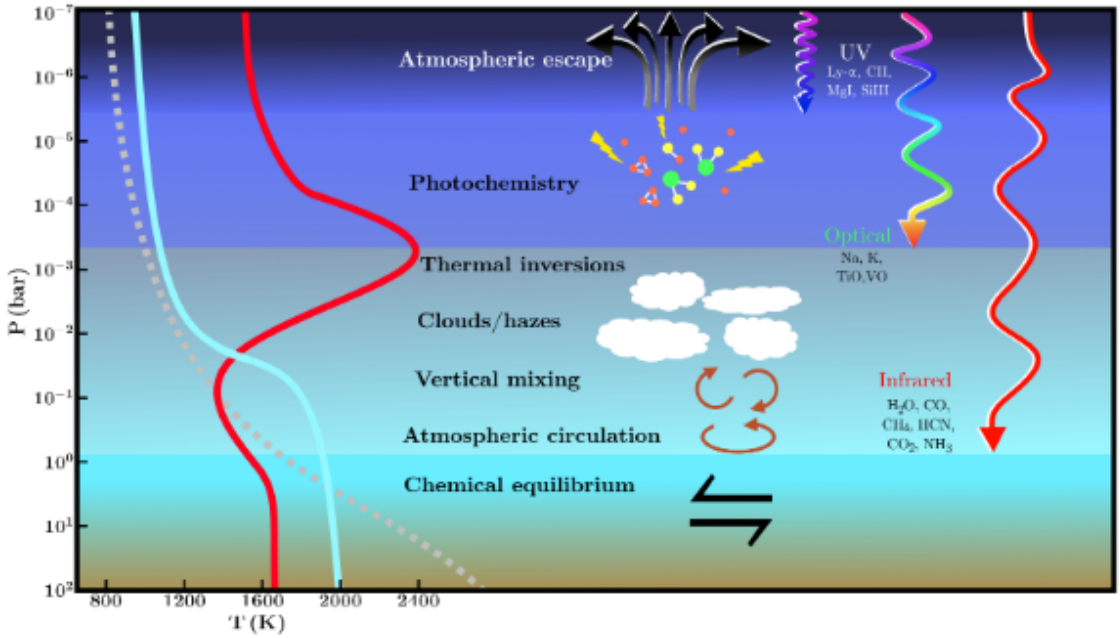


Figure 1.11: This diagram illustrates the processes occurring in exoplanetary atmospheres across different altitudes, highlighting how various parts of the electromagnetic spectrum probe them. The penetration depths of UV, optical, and infrared light are shown, indicating the specific atmospheric regions and chemical species detectable within each wavelength range. Additionally, three distinct temperature profiles are depicted: a highly irradiated planet with a thermal inversion (red), an irradiated planet without thermal inversion (cyan), and a poorly irradiated planet (grey, dashed). These profiles reflect the influence of stellar radiation on atmospheric dynamics and chemical compositions. Image from Madhusudhan (2019).

We are currently in an exciting phase of exoplanet research where precise studies of these far-off worlds' mass loss, temperature structures, aerosol properties, and atmospheric composition are now possible (Kempton and Knutson, 2024). We are able to observe smaller, colder exoplanets thanks to the (James Webb Space Telescope (JWST) Gardner et al., 2006). Additionally, JWST 's high signal-to-noise ratio (SNR) spectra for hotter and larger planets allow for the analysis of processes like photochemistry (Tsai et al., 2023) and inhomogeneous cloud formation (Fein-

stein et al., 2023) that were previously obscured in previous datasets. Scientists could look into atmospheric characteristics of a wide variety of exoplanet types because to JWST's big aperture and infrared capabilities (Kempton et al., 2023; Zieba et al., 2023; Greene et al., 2023).

As a result of the discovery of thousands of transiting exoplanets by space-based missions like Convection, Rotation and planetary Transits (CoRoT), Kepler, JWST and TESS, as well as ground-based surveys like Hungarian-made Automated Telescope (HAT), WASP, and Search for habitable Planets EClipsing ULtra-cOOl Stars (SPECULOOS), atmospheric characterization studies have evolved. From our perspective, transiting exoplanets provide several chances for atmosphere study as they pass in front of their host stars - primary transits, which occur when the planet passes in front of the star and is the main focus of this work; secondary transits, which occurs when the planet moves behind the star; and phase curve observations, which examine changes in light over time as the planet orbits.

## 1.8 Transmission Spectroscopy

During primary transit, some wavelengths of the starlight, while traveling through optically thin layers of the exoplanet's atmosphere, pick up spectral characteristics of that atmosphere. By comparing the star's spectrum outside of transit with measurements of the superimposed planet's atmosphere and by measuring the amount of light absorbed at different wavelengths, we can determine the composition and structure of the atmosphere (Seager and Deming, 2010; Kreidberg, 2017). A noticeable dip in the transit depth at specific wavelength bins indicates the presence of particular molecules in the atmosphere. This effect demonstrates the wavelength dependency of the planet's apparent radius and atmospheric opacity. Thus, transmission spectroscopy allows us to calculate the transit depth as a function of wavelength on an exoplanet's transmission spectrum.

This first spectral signature of an exoplanet was achieved through transmission spectroscopy using the Hubble Space Telescope (HST)'s Space Telescope Imaging Spectrograph (STIS) instrument (Charbonneau et al., 2002). Over the past two decades, transmission spectroscopy observations from space- and ground-based telescopes have unveiled a diverse array of exoplanet atmospheres. These studies have detected signatures of water vapor, carbon monoxide, potassium, and potential biosignature gases like methane and oxygen (Lustig-Yaeger et al., 2023). The technique has also revealed the presence of clouds, hazes, and Rayleigh scattering in many exoplanet atmospheres (Helling, 2019; Ohno and Kawashima, 2020).

### 1.8.1 Atmospheric scale height

As discussed in the above section 1.8, we observe the noticeable dip (excessive depth) in the light curve due to the presence of specific molecules during the transit event;

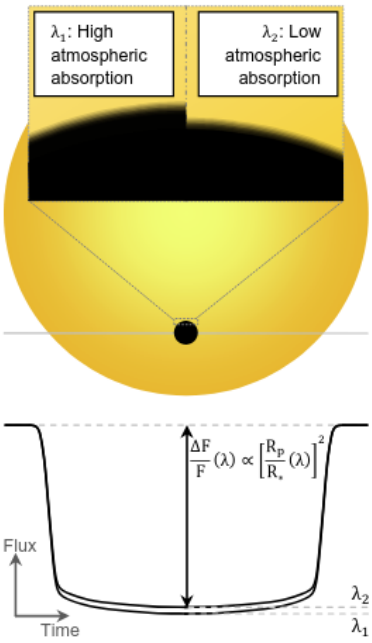


Figure 1.12: This figure illustrates the principle behind transmission spectroscopy. Atmospheric opacity sources at different altitudes lead to a wavelength-dependent variation in the transit depth. Image taken from De Wit and Seager (2013)

this is illustrated in Figure 1.12. We observe the night side of the exoplanet during primary transits, and the transmission spectrum gives us a cross-sectional view of the atmosphere from the planet's day-to-night boundary. The excessive depth of absorption is proportional to the ratio of the area of the star to that of the atmospheric annulus and can be expressed as (Sing, 2018):

$$\frac{\delta F}{F} = \frac{(R_P + nH)^2 - R_P^2}{R_*^2} \simeq \frac{2R_P nH}{R_*^2}. \tag{1.12}$$

Here, $\delta F$ represents the excess flux that the exoplanet's atmosphere absorbs, and $nH$ is the thickness of the atmospheric annulus, which is several times ($n \approx 5 - 10$) the atmospheric scale height $H$. The scale height represents the height over which pressure changes significantly with altitude in the exoplanet's atmosphere and can be derived using the ideal gas law and hydrostatic equilibrium.

$$H = \frac{k_B T}{\mu g}. \tag{1.13}$$

where, the Boltzmann constant is represented by $k_{\mathrm{B}}$, the temperature of the atmosphere is indicated by $T$, the mean molecular mass of the gases in the atmosphere is denoted by $\mu$, and the surface gravity of the planet is represented by $g$.

For giant exoplanets with an atmosphere dominated by H/He, the mean mass of the atmospheric molecules is typically estimated to be $\mu = 2.3$ atomic mass units (Sing, 2018). The atmospheric scale height, $H$, significantly influences the expected absorption signal from an exoplanet's atmosphere. Stronger absorption features in the transmission spectrum result from the atmosphere's farther-out extension, which

is indicated by larger scale heights. Strong surface gravity high-mass exoplanets, for example, typically have smaller scale heights and, thus, more modest absorption signals. However, because of their high temperatures, some hot Jupiters can display large-scale heights, which results in more pronounced signals in their transmission spectra. These hot Jupiters have inflated radii, which means they have low densities and surface gravities (Brown, 2001). A hot Jupiter's scale height is about 100 km, while that of an Earth-like planet is roughly 10 km. However, because Earth-like planets are also much smaller in radius, their atmospheric signal is further reduced. The expected variations in stellar flux due to atmospheric absorption are up to 0.1% for a hot Jupiter but only around 0.0001% for an Earth-like planet, making such detections significantly more challenging. This explains the reason for atmospheric characterizations of terrestrial exoplanets being rarer than those of hot Jupiters.

### 1.8.2 Equilibrium Temperature

Usually, the temperature of an exoplanet's atmosphere is approximated to its equilibrium temperature $T_{\rm eq}$, which represents the balance between the energy radiated back into space and the energy received from the host star. With zero albedo (fraction of light that is reflected by the planet's surface) assumed, $T_{\rm eq}$ can be computed as:

$$T_{\rm eq} = \left(\frac{1}{4}\right)^{1/4} T_{\rm eff} \sqrt{\frac{R_*}{a}} \tag{1.14}$$

where $R_*$ is the radius of the star, $a$ is the orbital semi-major axis of the planet, and $\rm T_{eff}$ is the effective temperature of the host star. The NASA Exoplanet Archive uses a relationship derived by Flower (1996) to determine the effective temperature based on the B–V color index. Alternatively, $\rm T_{eff}$ is typically estimated empirically or by fitting the blackbody curve to the star's spectral energy distribution.

## 1.9 Low-resolution transmission spectroscopy

A low resolving power[13] (R < 8,000) spectrograph is used to collect a large number of spectra in the case of low-resolution transmission spectroscopy. This method involves observing the target as well as one or more reference stars. The spectra are divided into different wavelength bands to produce color-dependent light curves. The gases or elements that are present in an exoplanet's atmosphere can be determined by measuring the transit's depth with wavelength dependency.

The primary advantage of low-resolution spectroscopy is that, under the same conditions, it requires less exposure time, allowing for greater SNRs even when observing fainter stars. Furthermore, a single device is capable of covering a large variety of wavelengths. For example, FORS2's ability to record data in the 330–1100 nm range enables researchers to analyze several spectral regions in different grism

[13]The resolving power R is defined as the smallest wavelength change $\Delta\lambda$ between two distinct spectral lines at wavelength $\lambda$. This can be expressed mathematically as $R = \frac{\Delta\lambda}{\lambda}$.

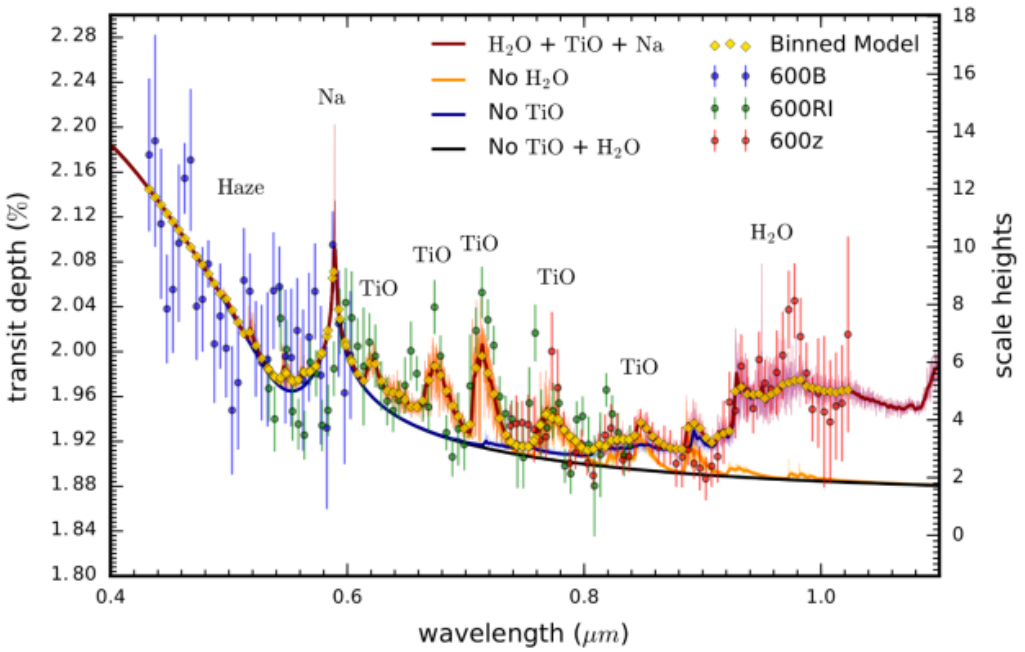


Figure 1.13: Transmission Spectrum of WASP-19 b: The plot displays transit depth (proportional to the square of the planet's radius) across various wavelengths. The colored solid lines represent atmospheric models with varying compositions. In the blue end of the optical spectrum, a scattering slope suggests the presence of haze, along with a sodium absorption signal. Molecular absorption from TiO and $H_2O$ can be identified in the green and red sections of the spectrum, respectively. Image taken from Sedaghati et al. (2017).

settings. Low-resolution transmission spectroscopy helps identify features in exoplanet atmospheres, such as clouds or hazes, based on how light is scattered at different wavelengths. Hazy conditions in an atmosphere can be suggested by a scattering slope, which often appears in the blue part of the optical spectrum, while a featureless spectrum may indicate clouds. High-altitude clouds and hazes can partially or completely block specific atomic or molecular features in the spectrum. In atmospheres with minimal cloud cover, low-resolution transmission spectroscopy technique can detect key atoms and molecules, such as sodium (Na), potassium (K), titanium oxide (TiO), and water vapor ($H_2O$), as noted in studies by (Sedaghati et al., 2016, 2017; Pont et al., 2013; Sing et al., 2016).

Investigations of hot Jupiters, such as WASP-19 b, reveal diverse atmospheric compositions (see Figure 1.13). For example, when compared to model atmospheres, the spectra of WASP-19 b show absorption characteristics from water, titanium oxide, and sodium. Other useful insights are provided by this approach, such as determining the vertical temperature structure in lower atmospheric layers (Vidal-Madjar et al., 2011) and calculating average atmospheric temperatures (Huitson et al., 2012). Additionally, these methods help outline the general shape of an exoplanet's spectrum, contributing to a fuller understanding of the atmosphere's properties. Despite its limitations in terms of fine detail resolution, this method is helpful for identifying atmospheric properties.

Early studies on exoplanet atmospheres depended significantly on this technique, thanks to the availability of space-based, low-resolution spectroscopy. Because the instruments on the HST and Spitzer Space Telescope are not contaminated by Earth's atmospheric features, they are frequently employed. The atmospheres of around 50 exoplanets have been characterized thanks in large part to HST.

## 1.10 High-resolution transmission spectroscopy

High-resolution transmission spectroscopy makes use of spectrographs that are highly stable and have a resolving power of more than 30,000. This method filters away the star's signature and isolates the signal from the planet's atmosphere by comparing spectra taken before and after the transit with those taken during the transit. As there are no space-based instruments with such high resolution even today, the technique was initially applied in ground-based research by Snellen et al. (2008); Redfield et al. (2008). As a result, telluric (Earth's atmospheric) features are always present in the data and must be carefully removed. High-resolution spectroscopy does not require a comparison star, unlike low-resolution spectroscopy, enabling the precise measurement of detailed features in an individual star's spectrum. Because more light is required for better resolution, this technique is typically restricted to monitoring brighter stars. Additionally, precise radial velocity measurements are crucial to extract the planetary signal properly.

On the 3.6-meter Telescopio Nazionale Galileo (TNG), instruments such as GIAno (0.97-2.4 micron) and haRPS (0.38-0.70 micron) (GIARPS) provide wavelength coverage similar to that of low-resolution instruments (Claudi et al., 2016). The ability to resolve fine details of planetary atmospheres allows researchers to study features like atmospheric composition, planetary rotation (via rotational broadening), and winds (through Doppler shifts). This approach has been used to detect a wide range of elements and compounds in exoplanet atmospheres, including sodium (Na) (Wyttenbach et al., 2015; Casasayas-Barris et al., 2017), potassium (K) (Keles et al., 2019), helium (He) (Nortmann et al., 2018), scandium (Sc) (Astudillo-Defru and Rojo, 2013), and hydrogen (also allowing study of atmospheric escape) (Yan and Henning, 2018).

One particularly helpful technique for detecting molecules is the cross-correlation function (CCF) (Snellen et al., 2010), later developed by (Hoeijmakers et al., 2018), which compares the observed spectra with a template of expected molecular signatures to enhance molecular detection. The CCF approach has been used to successfully detect several molecules like $H_2O$ (Birkby et al., 2013), TiO (Nugroho et al., 2017), HCN (Hawker et al., 2018), CO (Snellen et al., 2010), as well as atomic species like iron (Fe) and titanium (Ti) (Hoeijmakers et al., 2019).

# Chapter 2

# Instrument & Data Reduction

For this study, I used archival time-series data of stellar spectra of HAT-P-30 obtained with the FORS2 instrument on the VLT. In this chapter, I provide an overview of the instrumentation and the data reduction methods used for obtaining and analyzing the data. The data were processed using the `EsoReflex` pipeline, and the general steps involved are discussed based on the official manual. The computational and statistical techniques used in this thesis are then discussed.

## 2.1 FORS2

> Of all the instruments at Paranal, this one is the Swiss Army knife.
> – **Dr. Henri M. J. Boffin, my supervisor**

The FOcal Reducer/low dispersion Spectrograph 2 (FORS2) instrument on the VLT of the European Southern Observatory (ESO) (Appenzeller et al., 1998; Sedaghati, 2017) is installed at the Cassegrain focus[1] of the 8.2 m Unit Telescope 1 (see Figure 2.1, and for schematic overview 2.2). This is an all-dioptric instrument at the standard readout mode that provides an image scale of 0.25''/pixel. This mode bins the data by 2 pixels on both CCD axes. FORS2 is equipped with two detectors with a mosaic of two 2k×4k MIT CCDs or E2V CCDs (pixel size of 15×15 µm). Both detectors are sensitive across the entire spectrum, but the MIT CCD is more sensitive in the red, and the E2V CCD is more sensitive in the blue.

FORS2 offers the following observing modes:

- multi-object spectroscopy with movable arms (MOS)
- multi-object spectroscopy with exchangeable masks (MXU)
- long-slit spectroscopy (LSS)
- imaging and polarimetry
- Spectro-polarimetry

[1]Focal point of the secondary mirror (M2) of the telescope, situated directly below the large primary mirror (M1).

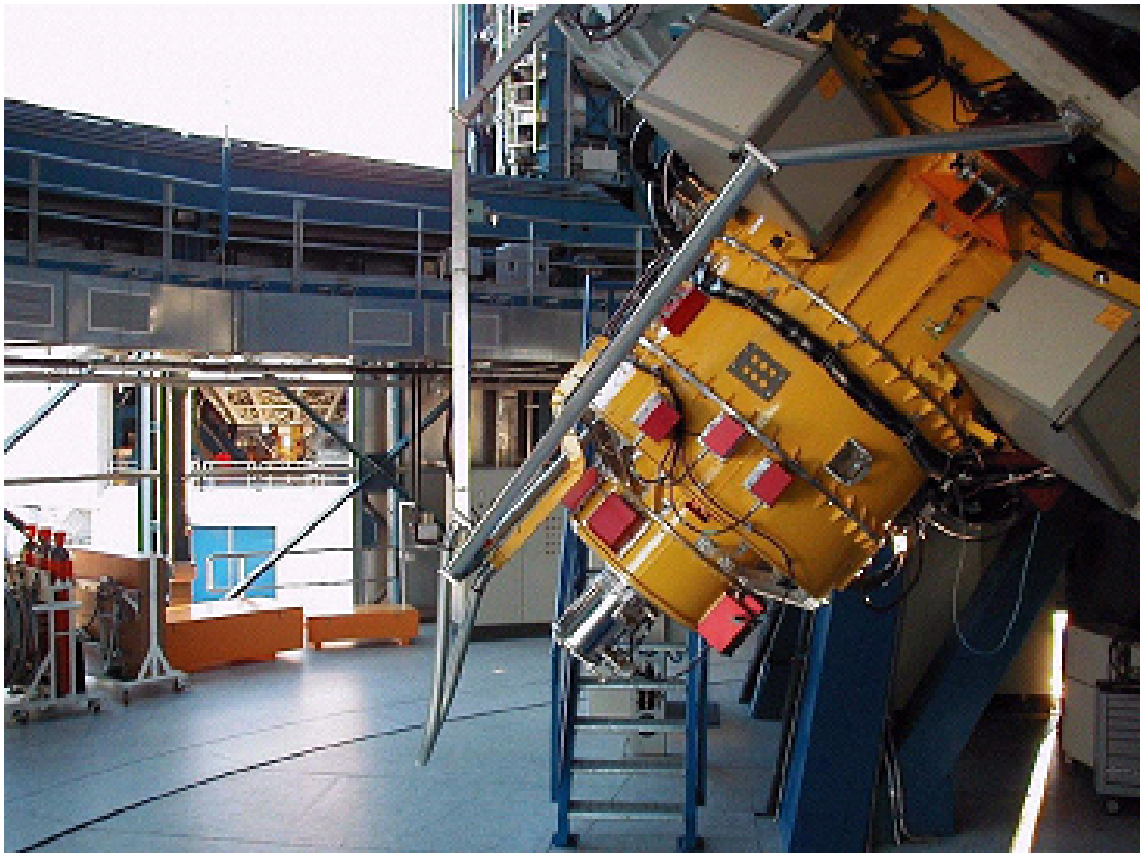

Figure 2.1: The two FORS instruments. The now-decommissioned FORS1 instrument can be seen in the background. The dismantling and storage of FORS1 happened in 2009 in order to make room for the second-generation instrument. ©ESO

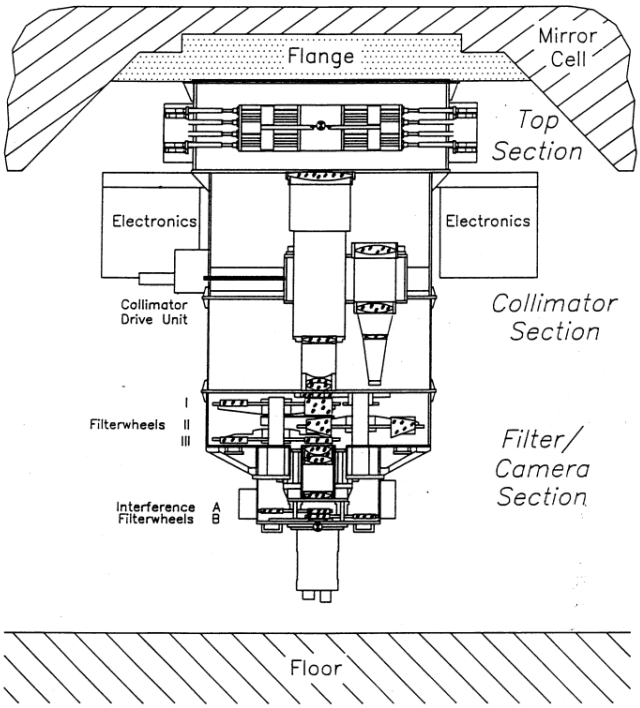


Figure 2.2: This schematic overview of the FORS2 shows the top section with the focal plane equipments, including the mask exchange unit for different types of observations, two collimators, the electronic cabinets, and various components like multiple filter wheels and grisms. Image taken from FORS2 User Manual.

The main scientific objective of FORS was to extend ground-based spectroscopy and photometry to significantly fainter objects. The field of view (FoV) of FORS2 with the standard resolution collimator is 6.8'×6.8', making it suitable for transmission spectroscopy as it allows the selection of multiple comparison stars.

The MXU mode is used for this work and transmission spectroscopy in general. In the MXU mode, the instrument also offers the possibility of inserting a custom-designed mask in the focal plane, where up to 470 slits of different lengths, widths, and shapes can be cut using a dedicated laser machine. This is the most preferred method for transmission spectroscopy because it allows for better selection of the areas of the Field of View (FoV) to be passed to the dispersing grisms.

### 2.1.1 Spectroscopy with FORS2

FORS2 can perform multi-object spectroscopy in 2 modes: MOS and MXU. By using motorized pairs of arms, the MOS mode enables simultaneous observations of up to 19 targets within the field of view. Slit lengths of 22.5'' and slit widths greater than 0.3'' are attainable with this configuration; by stacking the slits above one another, lengths that are integer multiples of this value can also be achieved (Boffin et al., 2015; Sedaghati, 2017). By mitigating the effects of atmospheric refraction up to an airmass of about 1.5, the 'Longitudinal Atmospheric Dispersion Corrector' allows for observations of the sky without experiencing flux losses.

## 2.2 EsoReflex

The ESO Recipe flexible execution workbench (EsoReflex) is a user-friendly environment developed by ESO to facilitate data reduction, with a particular focus on optimizing data quality and SNR. It provides a visual and intuitive interface for running ESO VLT pipelines, offering a clear, real-time representation of the data reduction process in the form of a workflow. Reflex is based on the Kepler Workflow engine[2], freely available under the BSD license, providing a graphical user interface using Java. This approach allows astronomers to easily follow the sequence of operations involved (Freudling et al., 2013). The general steps involved in the `EsoReflex` pipeline are based on the guidelines provided in the manual[3]. For more detailed information, it is recommended that you refer to the manual directly.

The workflow accepts science and calibration data downloaded from the archive using the CalSelector tool and automatically organizes them into 'DataSets', with each DataSet containing a single science object observation and all associated calibrations required for reduction. The workflow system is built to organize data into DataSets automatically. Thus, the user saves plenty of time and effort as the software organizes data automatically. The workflow leads a DataSet through the

[2] https://kepler-project.org
[3] FORS2 Reflex Tutorial

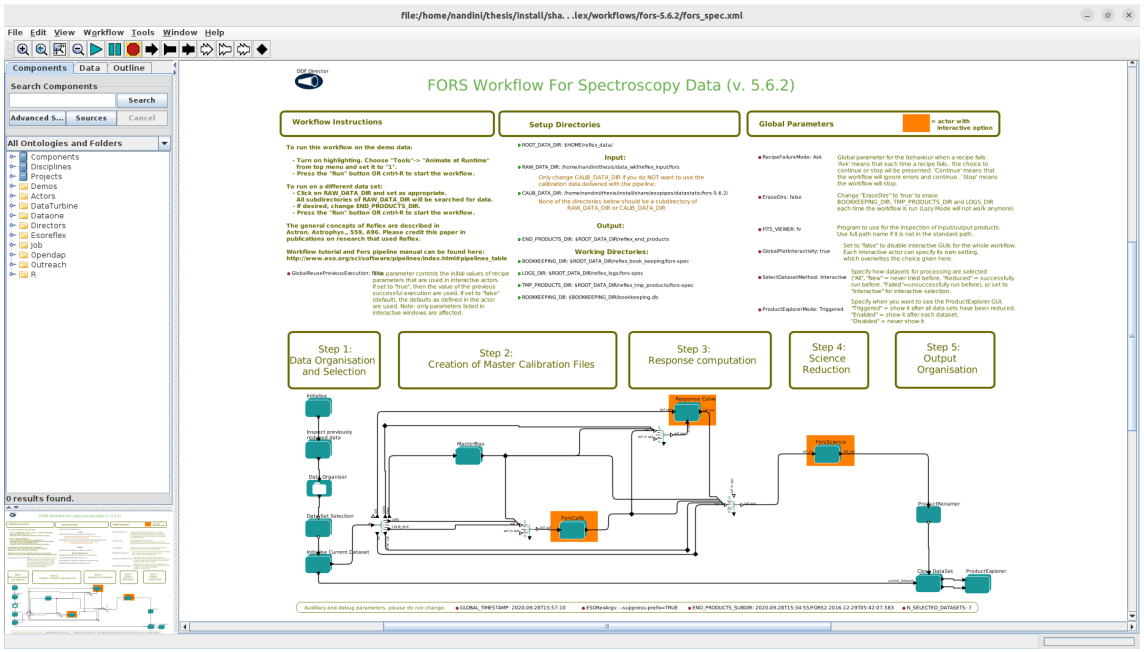


Figure 2.3: General layout of the FORS2 workflow for spectroscopic data.

proper pipeline recipes in the right order after it has been chosen for reduction. It allows users to modify recipe parameters fully, and conditional branches automatically handle any additional optional inputs. The final reduced data products are saved with user-configurable file names in a logically ordered directory structure. Even though the FORS2 pipeline typically produces high-quality results for the majority of spectroscopic data, some observations may need parameter adjustments to achieve optimal results, especially those with slits dispersed over a large range along the dispersion axis. This is supported by the workflow's interactive window for most recipes, which lets users check and adjust reduction parameters as necessary. Compared with standard techniques, this real-time visual and interactive method simplifies the data reduction process by allowing astronomers to monitor and optimize the procedure effectively. After the FORS2 pipeline was reassessed and finished in 2013–2014, significant improvements were made in areas like flux calibration, distortion correction, and error propagation.

An interactive window from this work for FORS workflow for spectroscopic data is shown in Figure 2.3. Let us understand the workflow steps that `EsoReflex` follows in detail.

## 2.2.1 Workflow steps

### 2.2.1.1 Data Organisation And Selection

The Data Organiser (DO) actor in the initial phase of the `EsoReflex` workflow takes input from specified directories containing raw and calibration data, detects and categorizes the files, and groups them into organized DataSets, a special Set of Files (SoF). Each DataSet includes the necessary files, such as science and calibration

data, that need to be processed together. Some files might be shared across several DataSets, especially calibration files. The DO keeps track of each file's name, category (such as raw science or raw calibration), and workflow-specific function. The OrganisationClassificationAssociation (OCA) rules, which assign categories and purposes based on header information in the files, are used for the classification. For every file, the workflow specifies a set of actions, each of which stands for a distinct processing phase. Following creation, the DataSets are displayed in the DataSet Chooser, where users can examine them and choose the ones that require processing. The DO, along with other components like the RecipeExecuter, ensures that files are properly categorized and directed to the relevant processing steps, enabling a smooth and efficient data reduction process.

For the data reduction of both the targets (HAT-P-30 b and WASP-96 b), preconfigured OCA files provided by the thesis supervisors were utilized.

#### 2.2.1.2 Data Chooser

The DataSetChooser in `EsoReflex` presents the available DataSets in a window where users can view relevant details such as the name, number of files, and reduction status, indicated by different flags: green (OK) for successful reductions, red (FAILED) for failed or aborted attempts, and black for new DataSets. Checkboxes let users to choose which DataSets to reduce; Figure 2.4 shows the filtering options available to select new, reduced, failed, or all DataSets. A single DataSet can be highlighted for detailed inspection, allowing users to examine the files it contains and their categories and even adjust the selection if necessary (e.g., to exclude poor-quality calibration frames). Additionally, the header information of any file can be viewed, and files can be opened in a FITS viewer (see Figure 2.5). In order to track particular reduction attempts, users may add custom descriptions. These descriptions can then be used to distinguish between different reduction strategies. With the flexibility and control provided by the DataSetChooser, users can tailor the data reduction and selection process to meet their particular needs.

#### 2.2.1.3 ProductExplorer

The final data products produced during the reduction process can be examined using the ProductExplorer actor. As shown in Figure 2.6, it offers an interactive interface of a list of all the datasets processed along with the corresponding reduction attempts. Users can easily monitor the status of each dataset as each reduction attempt is flagged as successful or failed. Additionally, the interface provides detailed information about every reduction, including user-added descriptions. Users can set up the ProductExplorer to appear either at the completion of the reduction process as a whole or following the processing of each DataSet separately. Because of this flexibility, users can process DataSets in batches or in real-time. Additionally, users can filter the displayed DataSets by their reduction status — successful, unsuccessful, or all datasets — making it easier to focus on specific subsets of data. The

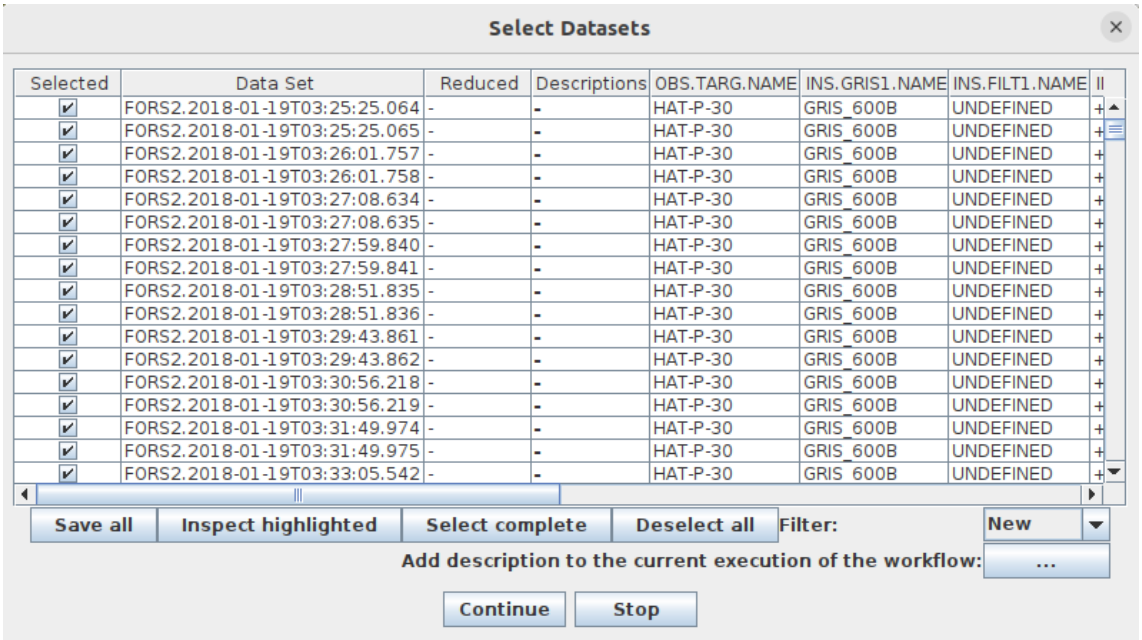


Figure 2.4: The "Select Frames" window displays every HAT-P-30 b raw input files that is awaiting reduction. After the successful run, in the "Reduced" column, files that have been successfully reduced are indicated as "OK" in green, and files that have not been reduced are indicated in red.

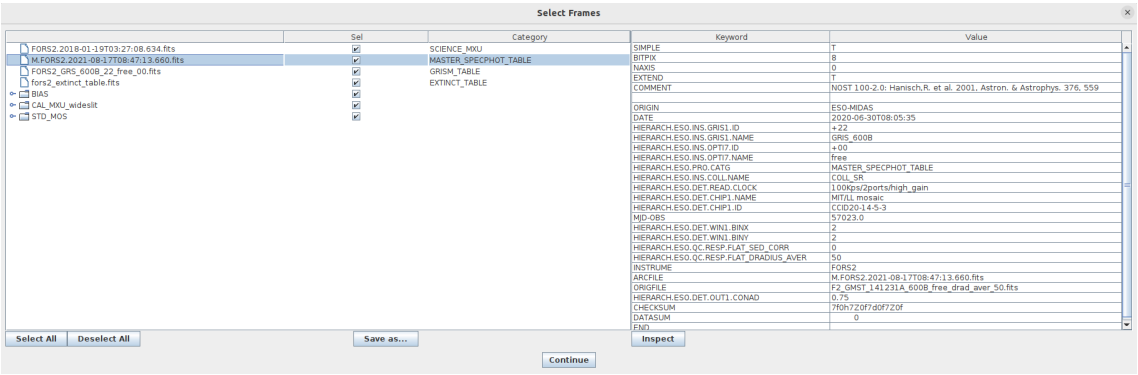


Figure 2.5: A single file from the current DataSet is highlighted in blue in the "Select Frames" window, and the text box on the right displays the matching FITS header.

ProductExplorer allows users to interact with the data products, including opening files in selected FITS viewers, inspecting file headers, and reviewing the processing steps that led to the final products. It provides a powerful tool for tracking, organizing, and validating the outputs of the data reduction workflow.

#### 2.2.1.4 Creation of Master Calibration Files

The creation of master calibration files is one of the most important steps in the workflow. These master files, such as bias or flat-field frames, are generated from raw calibration data and are used in subsequent steps of data reduction to correct the science data. The workflow ensures that the appropriate calibration files are processed in the correct order to produce reliable master calibration files.

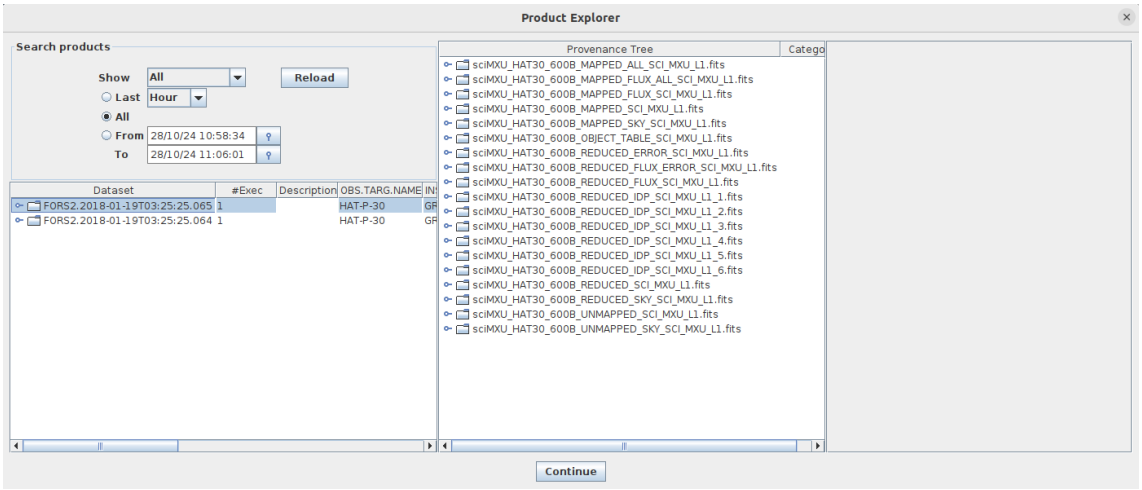


Figure 2.6: The ProductExplorer window displays the complete reduction chain for each pipeline product along with all the datasets that have been reduced in prior executions.

The fors_calib interactive window provides insight into the calibration data for the FORS2 instrument. It shows the quality of various steps, including wavelength calibration, spatial distortion correction, and flat-field normalization. Users can inspect the wavelength-calibrated arc lamp frames, ensuring that arc lines are straight and free from gaps, which can indicate issues with detection. In Figure 2.8, arc lines in the wavelength-calibrated arc lamp frame are shown in the top-left panel. Arc lines that have been detected and identified are compared in the center-left panel; matched lines are indicated by green. Residuals between the observed and predicted arc line positions are shown in the bottom-left plot, ideally they should be within $\pm 0.5$ pixels. To verify slitlet alignment, the top-right spatial map displays the distances of each pixel from the bottom of each slitlet. The raw and normalized flat fields are compared in the bottom-right and center-right panels to ensure uniform slitlet alignment and illumination. This tool allows for refinement of calibration procedures, essential for achieving accurate spectral data, by ensuring all detected lines are properly calibrated and corrected.

#### 2.2.1.5 Wavelength Calibration

In order to create the spectral extraction mask required for scientific data reduction, this step involved mapping spectral edges based on flat field exposures and matching reference lines from arc lamp exposures. `EsoReflex` produces a rebinned, 2D science frame after completing the wavelength calibration row by row. This method effectively eliminates instrumental line curvature, allowing the wavelength-calibrated spectra to be extracted without additional modification. The FORS2 pipeline provides flexibility for wavelength calibration by enabling different calibration lamps based on the necessary spectral resolution. He, HgCd, and Ar lamps are commonly used for lower-resolution setups, while the Ne lamp can be used for higher-resolution calibrations. The calibration library[4] contains a complete list of

[4] Calibration library

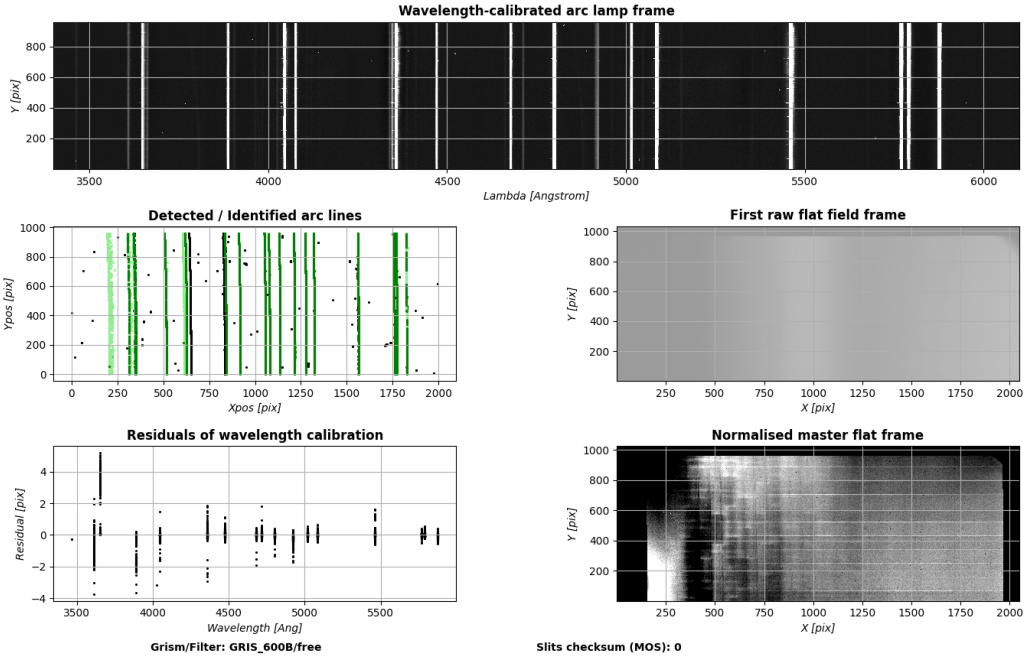


Figure 2.7: The fors_calib actor's interactive window for the HAT-P-30 b's DataSet's MXU calibrations. Initially, the calibration data of the flux standard star are processed.

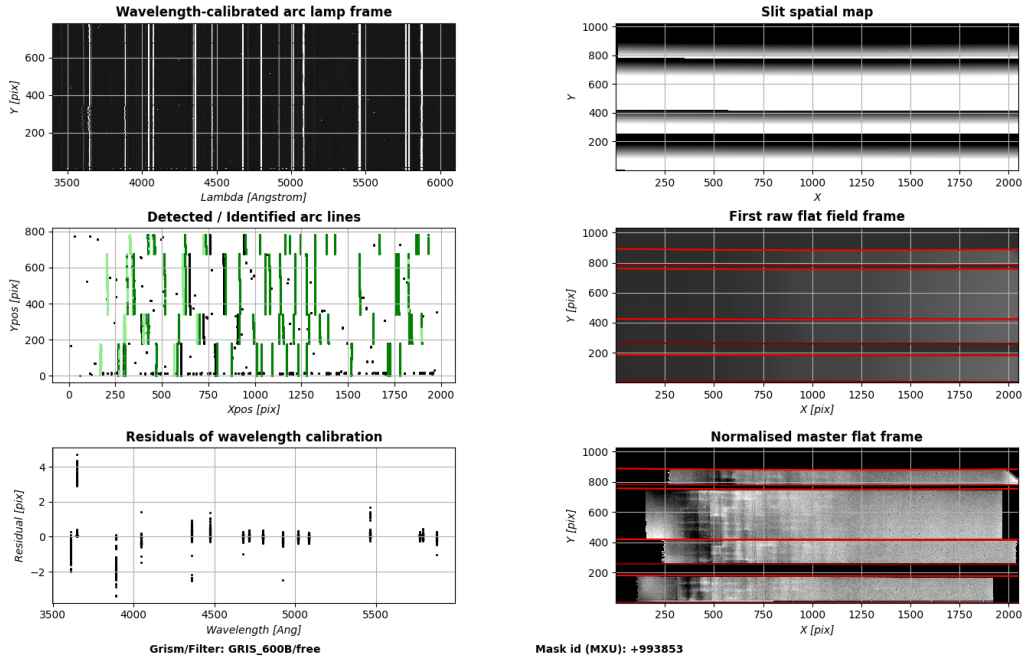


Figure 2.8: The fors_calib interactive windows display the calibration details.

lines that the pipeline uses. By fitting a 2nd-degree polynomial in the spatial direction and a 5th-degree polynomial in the dispersion direction, the pipeline can handle a range of grism and slit combinations.

#### 2.2.1.6 Response Computation

Response computation involves determining the instrument's sensitivity to light at different wavelengths. This step uses spectrophotometric standard stars to compute a response curve, which is later applied to the science data for accurate flux calibration. The response curve accounts for instrumental and atmospheric effects, ensuring that the final science spectra are properly calibrated in terms of flux. A quality assessment of the response fit is shown across multiple panels in Figure 2.9. The standard star's extracted spectrum is displayed in the top panel; it should be smooth and free of noticeable sky emission lines or abrupt jumps, as these could affect the accuracy of the response curve. The fitted response curve is shown in blue, and the raw response data is displayed as points in the center panel. Green points represent the unmasked data used for fitting, and the masked data is displayed in blue to help visualize areas that may require adjustments. The bottom panel compares the reference values (represented by green and blue points) with the flux-calibrated standard star spectrum (represented in red). The red curve should ideally be very close to the green points; any notable discrepancies could be a sign of calibration problems, particularly in areas where atmospheric absorption is present. Through this interface, users can fine-tune the response curve and improve the calibration accuracy of the final science spectra by adjusting fitting parameters like spline fit or polynomial degree.

#### 2.2.1.7 Science Reduction

The science reduction actor applies the calibration data (e.g., bias, flat-field, wavelength calibration) to the raw science data. This process includes correcting for instrumental distortions, removing the sky background, and calibrating the flux. The goal is to extract clean, scientifically useful spectra from the raw data with minimal noise and artifacts. HAT-P-30 b's extracted target and reference star spectrums are shown in Figures 2.10 and 2.11.

#### 2.2.1.8 Output Organization

Once the data reduction process is completed, the Product Renamer actor in the data processing workflow systematically renames and organizes the final output files within a directory structure based on key observation data, using metadata like the observation block (OB) name, and product type, making them easily accessible for further work.

In my work with MXU mode, this process generates two primary types of outputs: 1D extracted spectra and 2D wavelength-calibrated, distortion-corrected images. The 1D spectra capture essential details about each individual object observed,

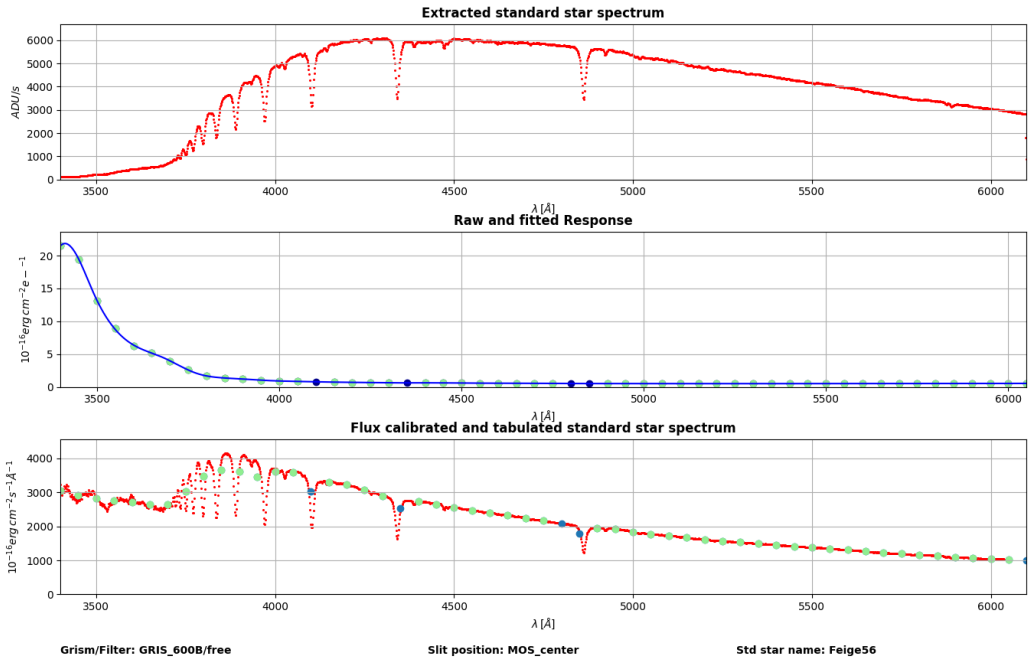


Figure 2.9: The interactive window of the Response Curve actor for the HAT-P-30 b DataSet. The top panel shows the extracted spectrum of the standard star. The middle panel displays the raw response data (points) and the fitted response curve (blue), with unmasked data in green. The bottom panel compares the flux-calibrated spectrum (red) to reference values (green/blue); deviations may indicate calibration issues, especially in regions of atmospheric absorption.

while the 2D frames represent fully processed images that have undergone corrections such as distortion removal.

The 2D images are especially important for the next phase of analysis, as they offer a clean and calibrated format that is ready for scientific study. I performed the Gaussian fitting to extract the stellar spectrum from the 2D files; refer section 3.3.1 for more details.

## 2.3 Tiberius

In my thesis, I utilized the Python package `Tiberius`, developed by Dr. James Kirk and Dr. Eva Maria Ahrer (Kirk et al., 2017, 2021). `Tiberius` is specialized for reducing time-series spectra and fitting exoplanet transit light curves, making it suitable for a range of spectral data sources, including JWST, ground-based long-slit spectrographs, and Keck/NIRSPEC echelle spectra (beta).

For my analysis, I developed my own Python code to extract spectra and generate both white-light and binned light curves. I then employed `Tiberius` for the light curve fitting, which performs Gaussian processes (GP) and Markov chain Monte Carlo (MCMC) to model the transit events and refine parameter estimates, and

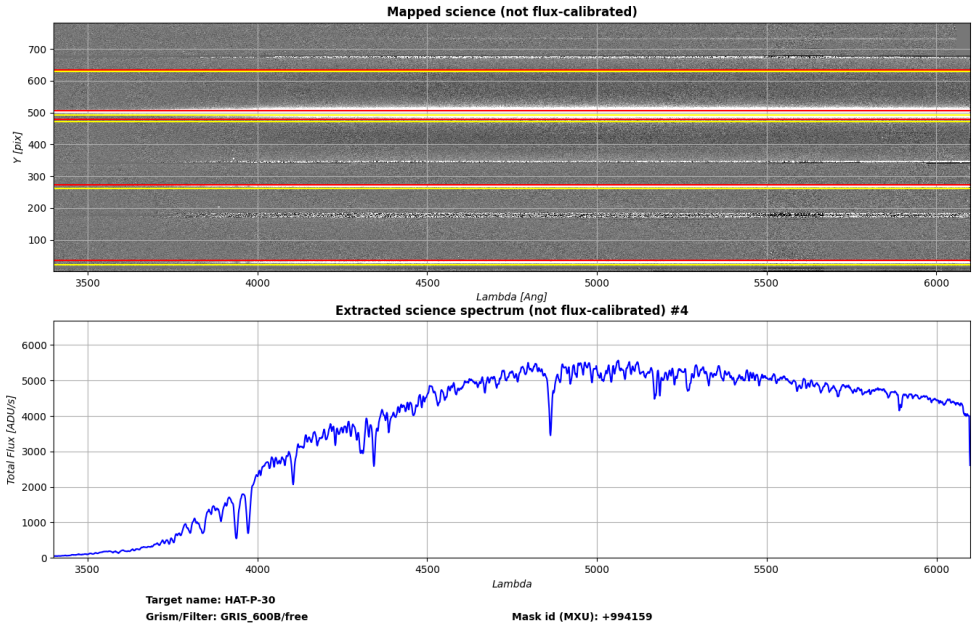


Figure 2.10: `EsoReflex`'s ForsScience actor's interactive window displaying the quality of HAT-P-30 b's target star spectrum extraction and sky subtraction in ADU/sec (not flux-calibrated). The sky-subtracted, wavelength-calibrated 2D spectrum is shown in the top panel, where red and yellow lines indicate the extraction limits for detected spectra. To ensure efficient sky subtraction, users can zoom in to confirm the spectra's horizontal alignment. The extracted science spectrum is displayed in the bottom panel, ideally with minimal skyline residuals for a smooth appearance.

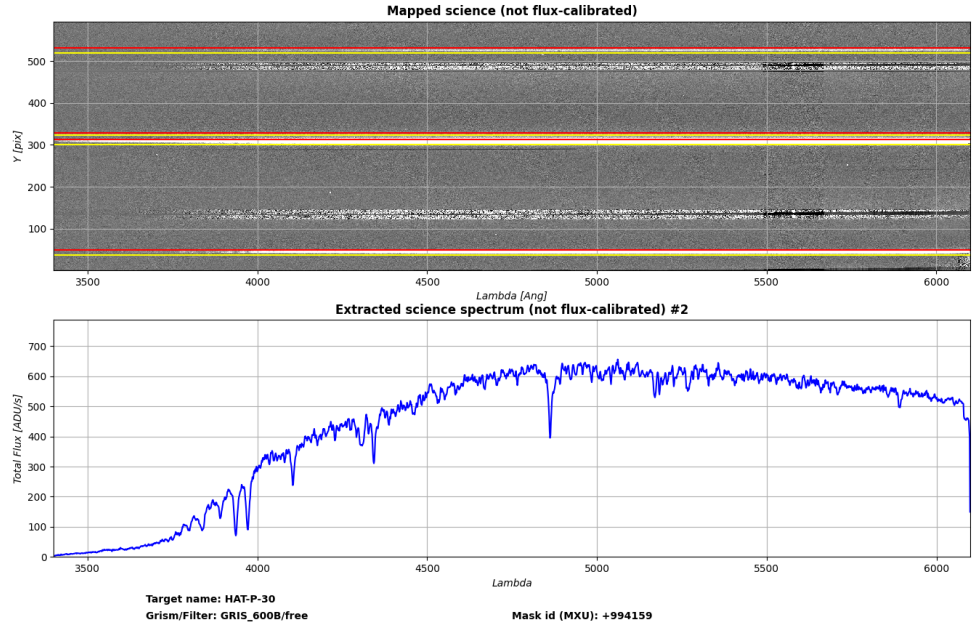


Figure 2.11: The interactive window of `EsoReflex`'s ForsScience actor showing the quality of sky subtraction and reference star spectrum extraction for HAT-P-30 b in ADU/sec (not flux-calibrated).

later to construct the transmission spectrum. Detailed process for each planet is described in chapters 3 and 4, but I describe Gaussian processes and MCMC below.

### 2.3.1 Gaussian Processes

GP refer to distribution over functions, such that instead of modeling a function $f(x)$ at just a few points, one can model $f(x)$ at all possible points, ensuring a smooth and continuous function, see Figure 2.12

Mathematically, a GP is defined as:

$$f(x) \sim \mathcal{GP}(\mu(x), \Sigma(x_i, x_j)) \tag{2.1}$$

where:

- $\mu(x)$ is the mean function (often assumed to be zero),
- $\Sigma(x_i, x_j)$ is the covariance matrix

If we select any finite set of points $X = \{x_1, x_2, ..., x_n\}$, the function values $f(X)$ follow a multivariate normal distribution:

$$f(X) \sim \mathcal{N}(\mu(X), \Sigma(X, X)) \tag{2.2}$$

When you observe some points, the GP updates its distribution of the function with a new mean and variance. GP are extremely useful in Bayesian inference as they also provide uncertainty estimates.

GPs are becoming increasingly important in the study of exoplanets, particularly when it comes to describing data that have intricate, correlated noise patterns that typical parametric models might find difficult to represent (Kirk, 2018). Their ability to characterize relationships in data without the need for strict formulas makes them particularly useful. They model how data points are connected by calculating a "covariance" between them. This feature makes GP particularly useful for separating the signals of interest from red noise, also known as correlated noise, which is prevalent in astronomical data. In practice, a GP models the covariance between data points with a kernel function and a set of hyperparameters describing each pairwise correlation. Typically, a GP's general log-likelihood function for $\mu$ observations is expressed as follows:

$$\ln P(y|\theta) = -\frac{1}{2}(\mu \ln 2\pi + \ln |\Sigma| + r^T \Sigma^{-1} r) \tag{2.3}$$

The residuals (observed data minus model prediction) are denoted by $r$, the covariance matrix by $\Sigma$, and the model parameters by $\theta$. The kernel $K(x_i, x_j)$ defines the correlation between data points $x_i$ and $x_j$ and is combined with a white noise term $\sigma^2$ applied to the diagonal elements to create the covariance matrix $\Sigma_{ij} = K(x_i, x_j) + \sigma^2 \delta_{ij}$. The kernel can also be redefined to incorporate the $\sigma$ term

within it.

Because the choice of kernel can affect the noise properties of the GP, a kernel function can be chosen based on the one that best describes the noise in the data. For instance, the squared exponential kernel and Matérn kernels are commonly used in exoplanet research.

The squared exponential kernel:

$$K_{SE}(x_i, x_j) = a^2 \exp\left(-\left(\frac{x_i - x_j}{\tau}\right)^2\right) \tag{2.4}$$

where, $a$ denotes the amplitude, and $\tau$ the length scale, is perfect for simulating smooth, continuous correlations. The strength and range of correlation are determined by the hyperparameters $a$ and $\tau$. In contrast to a squared exponential kernel, the Matérn class of kernels permit greater frequency variance. Because of its greater flexibility, this kernel can record data changes that are more abrupt or rough. Matérn 3/2 kernel is expressed by the equation:

$$K_M(x_i, x_j) = a^2 \left(1 + \frac{\sqrt{3(x_i - x_j)^2}}{\tau}\right) \exp\left(-\frac{\sqrt{3(x_i - x_j)^2}}{\tau}\right) \tag{2.5}$$

In addition to the squared exponential and Matérn kernels, there are several other kernels, such as periodic kernels. These can be especially helpful when modeling the impact of stellar activity on light curves. GPs have been successfully used in exoplanet science to deal with sources of noise that are difficult to model using fixed formulas, such as instrument effects and stellar activity. They are used, for example, in radial velocity measurements to distinguish planetary signals from stellar activity (Haywood et al., 2014; Rajpaul et al., 2015) or in transmission spectroscopy (Gibson et al., 2012; Evans et al., 2015) for detrending K2 data (Aigrain et al., 2016). Because of their ability to adjust to different kinds of noise, GPs are extremely useful for improving measurement accuracy and understanding uncertainties in exoplanet data. The transit model and a GP with one or more kernels are used to build the GP model in actual practice. Time or other parameters like the full width at half maximum (FWHM) of the extracted spectra, the airmass, or the rotation angle axis (ras), among others, are used as inputs by the kernels to capture the detrending of the light curve.

### 2.3.2 Markov Chain Monte Carlo

The MCMC is a method for finding the best possible values for a model when there are many unknowns. Points are generated such that after a sufficient number of iterations, the samples produced by the Markov chain approximate the true distribution. The MCMC algorithm explores parameter spaces, identifies best-fit models, and generates posterior distributions by combining Monte Carlo sampling with Markov chains. Thus, Monte Carlo sampling uses random sampling techniques

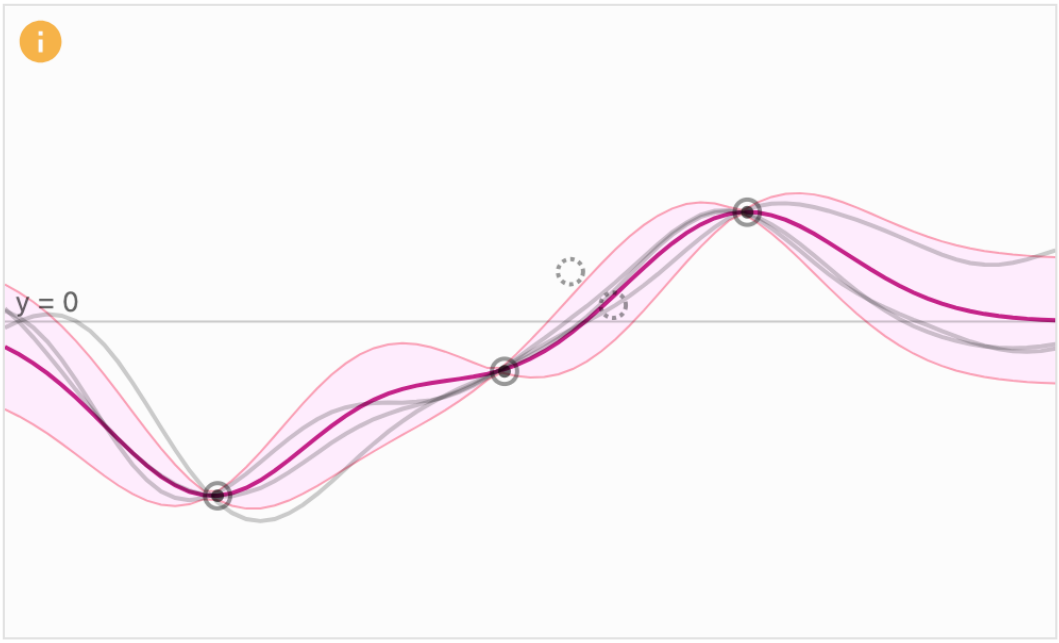


Figure 2.12: An example of a GP model using radial basis function kernel. Only dotted points are part of the Bayesian update. The non-dotted circled points aren't a part of the GP yet. The gray lines represent draws from the GP. The pink region corresponds to the $1\sigma$ region with the red line indicating the 'mean' function. Image taken from Görtler et al. (2019).

to approximate probability distributions, while Markov chains ensure that each new sample depends only on the previous one, allowing efficient exploration of parameter spaces. The algorithm goes through a "burn-in" phase that starts with initial values and is removed from the output. Users specify variables such as walkers, burn-in samples, and the number of steps. The `emcee` package is used to implement MCMC in the `Tiberius` package (Foreman-Mackey et al., 2013). `emcee` employs an ensemble of $n$ walkers, each sampling a different region of the parameter space at each time step, instead of evolving a single chain. Faster convergence results from this ensemble approach's effective reduction of autocorrelation time, which measures how many steps it takes for the samples to become statistically independent. In a poorly mixed chain, new samples remain correlated with previous ones, making convergence slow and inefficient. Reducing autocorrelation time allows the algorithm to explore the parameter space more effectively and produce reliable posterior distributions with fewer iterations. The walkers investigate the parameter space during the burn-in phase, usually starting in less probable regions and moving toward the more probable ones (Ahrer, 2023; Kirk, 2018). This burn-in phase is eliminated after it has been completed, and the posterior probability distribution function is built using the remaining samples, providing a more efficient and reliable method to explore parameters.

# Chapter 3

# HAT-P-30 b

Previous ground-based studies of hot Jupiters have revealed mainly the detection of narrow lines cores of sodium (Nikolov et al., 2018; Snellen et al., 2008) and potassium (Wilson et al., 2015; Sedaghati et al., 2016). On the other hand, some have thick clouds or hazes that block off the majority of spectral features (Kirk et al., 2016; Mallonn et al., 2016). In order to gain a better understanding of the factors determining atmospheric composition, cloud formation, and the presence of hazes, it is necessary to expand the sample of studied hot Jupiter atmospheres.

In this thesis, I present the low-resolution ground-based transmission spectrum of the hot Jupiter HAT-P-30 b - (planetary parameters are recorded in Table 3.1 for reference). HAT-P-30 b is transiting a relatively bright and hot late F-type dwarf star ($T_{\rm eff} = 6300$ K) with magnitude $V = 10.4$ (Johnson et al., 2011). With a very low density and large scale height, HAT-P-30 b is a good target for transmission spectroscopy. Another interesting part is the alignment of the planetary orbit: HAT-P-30 b's projected stellar obliquity is $\lambda$[1] $= 73.5° \pm 9.0°$ (Johnson et al., 2011; Cegla et al., 2023), which is much more greater than $|\lambda| \geq 10°$ (Winn et al., 2010) making it a highly misaligned planet. Planets with such high misalignments are of great interest as they suggest different migration mechanisms, such as high-eccentricity tidal migration, rather than smooth inward migration through a protoplanetary disk. These mechanisms can provide insight into the planet's dynamic history and interactions with its stellar environment. Studying the atmosphere of this planet will help us also understand the formation mechanisms and evolutionary paths of hot Jupiter (Kirk et al., 2024).

## 3.1 Observations

Observations of transits of HAT-P-30 b were carried out as part of the program 199.C-0467(S), (Principal Investigator (PI) - Nikolov Nikolay), whose goal was to perform the first large-scale ground-based transmission spectral survey of twenty exoplanets with FORS2 across the full range of physical properties. The two transit

[1] $\lambda$ is the projected angle between the stellar spin axis and the normal to the orbital plane.

Table 3.1: Properties of the host star HAT-P-30 and planet HAT-P-30 b. Values taken from Johnson et al. (2011).

| | Parameter | Value |
|---|---|---|
| Star | Spectral Type | F |
| | $V_{mag}$ | 10.4 |
| | Mass, $M_*$ ($M_\odot$) | 1.242 ± 0.041 |
| | Radius, $R_*$ ($R_\odot$) | 1.215 ± 0.051 |
| | vsin $i_*$ (km/s) | 2.2 ± 0.5 |
| | Effective temperature, $T_{eff}$ (K) | 6304 ± 88 |
| | Metallicity, [Fe/H] | 0.13 ± 0.08 |
| Planet b | Period, P (days) | 2.810595 ± 0.000005 |
| | Semi-major axis, a (au) | 0.0419 ± 0.0005 |
| | Mass, $M_P$ ($M_{Jup}$) | 0.711 ± 0.028 |
| | Radius, $R_P$ ($R_{Jup}$) | 1.340 ± 0.065 |
| | Inclination, $i$ (°) | 83.6 ± 0.4 |
| | Equilibrium temperature, $T_{eq}$ (K) | 1630 ± 42 |
| | Impact parameter, $b$ | 0.854 ± 0.008 |

observations of HAT-P-30 b were carried out on the nights of January 19, 2018 and a month later, on February 19, 2018 UTC in photometric conditions, using the FORS2 spectrograph. On the first and second nights respectively, data were obtained utilizing `600B` (blue) and `600RI` (red) grisms, which together cover the wavelength range of 360 to 820 nm. The instrument was operated in MXU mode, which indicates that the target and reference stars were positioned within a specially made mask that had 10''wide slits adjusted within the path of the light. This effectively serves as a blocking mask to open the CCD to record simultaneous spectra. Figure 3.1 obtained from P2demo[2] illustrates the observational setup of HAT-P-30 b. For this thesis, in total, I used 1556 FORS2 spectra (778 of the target star and 778 of the reference star) of these observations from the ESO archive[3], obtained from both CHIP1 and CHIP2. Of these, 632 spectra (316 of the target star and of the reference star) belong to the first night observation using `600B` - blue grism (see Figure 3.3), and 924 spectra (462 of the target star and the reference star, each) were observed in the red band with `600RI` - red grism on the second night; see Figure 3.4. The raw acquisition images obtained during this observational run are presented in Figure 3.2.

The first transit observational sequence with grism `600B` (blue) lasted ∼ 5 hours. The complete transit lasted ∼ 2 hours, with the first contact at 5:30 UT and the last one at 7:37 UT. This transit timing information for both night observations was obtained using the NASA Exoplanet Archive website[4]. 724 spectral frames (362 of these are individual spectra of the target) were acquired with airmass ranging from 1.15 to 1.9 and exposure time was around 20 s for all the frames throughout the observations. The second transit observational sequence with grism `600RI` (red) lasted ∼ 4.9 hours. The complete transit event had first contact at 3:29 UT and

[2] https://www.eso.org/p2demo/home/run/60900301

[3] http://archive.eso.org/eso/eso_archive_main.html

[4] https://exoplanetarchive.ipac.caltech.edu/cgi-bin/TransitView/nph-visibletbls?dataset=transits

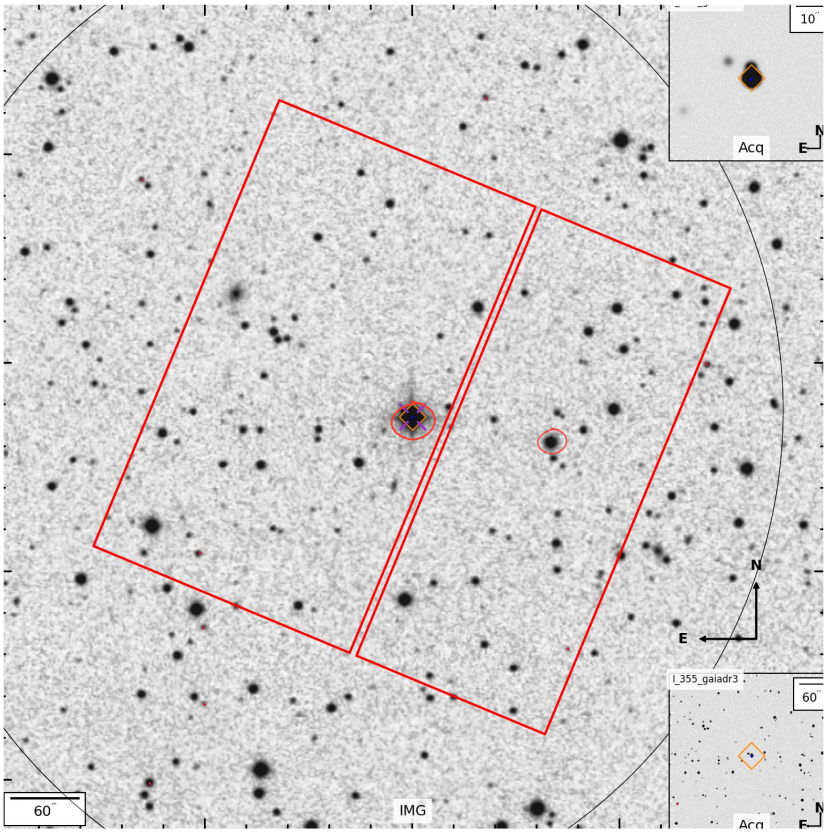


Figure 3.1: Illustration of observational set up of HAT-P-30, observed under program ID 199.C-0467(S) by project PI, image taken from P2demo. The red lines outline the two-chip detector mosaic. HAT-P-30 is positioned on the right chip, while Gaia DR3 3096359610087012480 serves as the reference star on the left chip, highlighted by red circles.

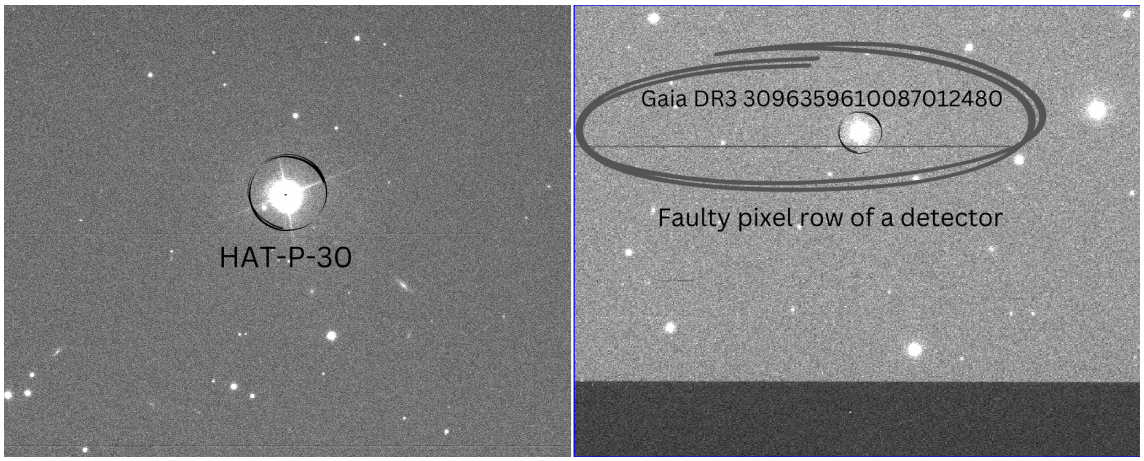


Figure 3.2: Raw acquisition frames of HAT-P-30 from the first night observed using the grism `600B` (blue). The left panel shows HAT-P-30 positioned on Chip 1, and the right panel presents the reference star on Chip 2, along with a faulty pixel row as a black line below it.

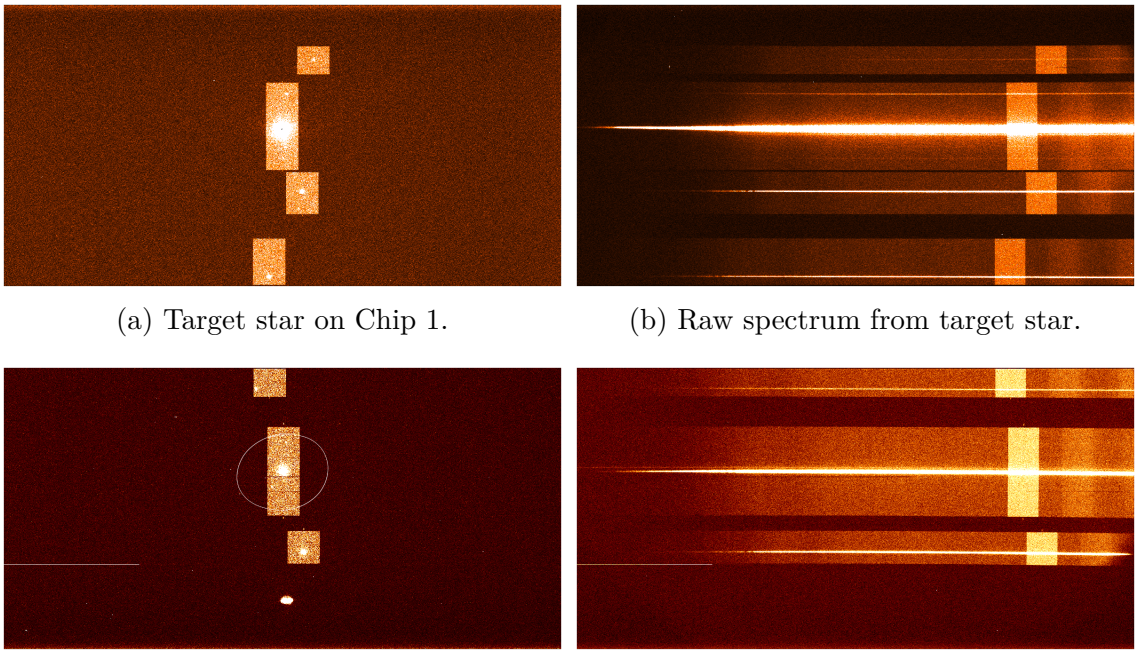

(a) Target star on Chip 1.

(b) Raw spectrum from target star.

(c) Reference star on Chip 2.

(d) Raw spectrum from reference star.

Figure 3.3: Acquisition frames of HAT-P-30 from the first night using the blue grism (600B). The top row shows the target star positioned on Chip 1 (left) and its raw spectrum before wavelength calibration (right). The bottom row presents the reference star on Chip 2 (left) and its corresponding raw spectrum (right). In the bottom left panel, a white circle highlights the reference star, and a faulty pixel row appears as a black line below it. The other stars shown are additional slits with potential reference stars, but that were not used because they are too faint for my analysis.

the last one at 5:37 UT. A total of 854 spectral frames (427 of the target star and 427 of the reference star) were obtained, with the airmass varying between 1.159 to 2.011. The exposure time was set around 11-13 s for the first 650 frames and later was changed to 15-18 s for the rest of the observations to increase SNR.

## 3.2 Data Reduction

The data reduction was performed utilizing an automated `EsoReflex` pipeline, explained in Section 2.2. I had to replace some of the 'WAVE' files of 'MASK ID 99419' with files of 'MASK ID 993853' in the raw data obtained with a narrow slit mask, for the wavelength calibration. Additionally, I used a modified OCA file, for data reduction. Only a few parameters were changed to reduce noise influences and obtain better fitting as described in the manual, as the rest of the parameters are already ensured by the pipeline according to the grisms and the spectra captured. Figures 3.5 & 3.6 illustrate the sample reduced spectra obtained with the `EsoReflex`. Sky subtraction was performed with self-written Python code, described in Section 3.3.1.

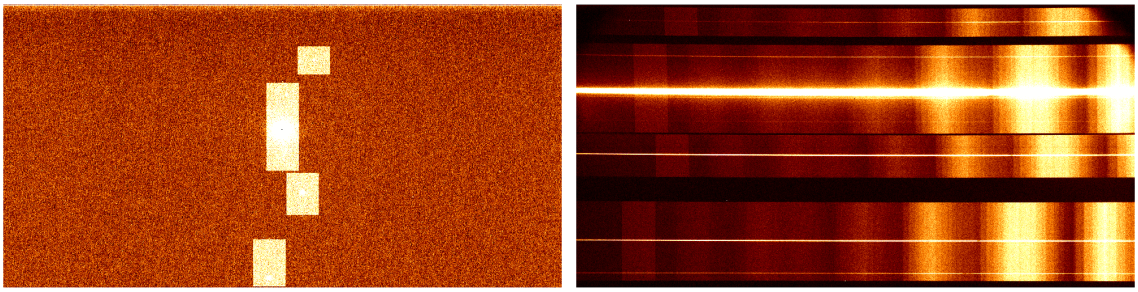

(a) Target star on Chip 1.

(b) Raw spectrum from target star.

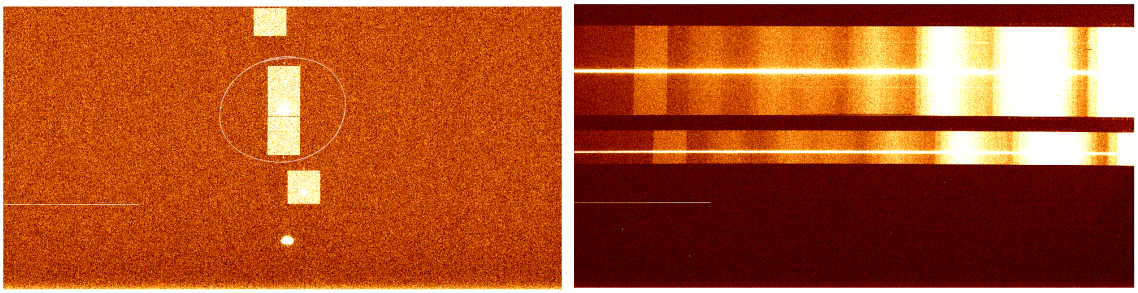

(c) Reference star on Chip 2.

(d) Raw spectrum from reference star.

Figure 3.4: Acquisition frames of HAT-P-30 from the second night using the grism `600RI` (red). The top row shows the target star positioned on Chip 1 (left) and its raw spectrum before wavelength calibration (right). The bottom row presents the reference star on Chip 2 (left) and its corresponding raw spectrum (right). In the bottom left panel, a white circle around the central slit highlights the reference star and a faulty pixel row (black line) below it.

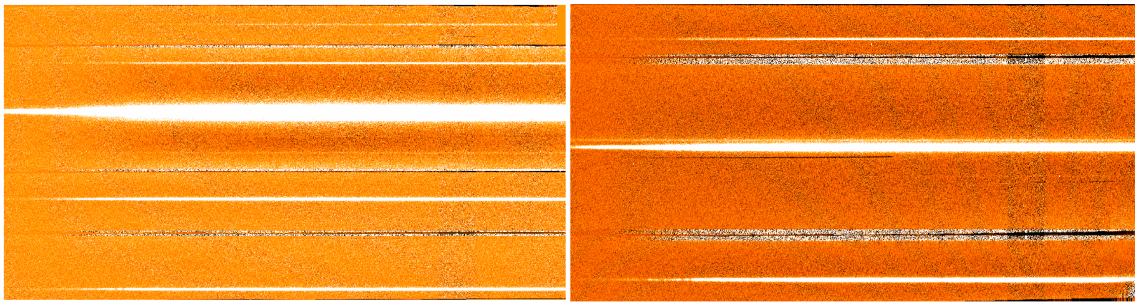

Figure 3.5: Left and the right panels show reduced spectra (after wavelength calibration) of the target and reference star respectively, from the first night observation after the data reduction with the `EsoReflex` pipeline. Here, the x-axis pixel corresponds to the wavelength direction, and the y-axis indicates the pixel's spatial direction.

## 3.3 Data Analysis

### 3.3.1 Spectrum extraction

The data reduction performed using the `EsoReflex` pipeline did not yield satisfactory 1D spectra for our analysis. To address this, I developed a custom Python script to extract spectra directly from the 2D files. For this study, I have multiple reference stars positioned on the CHIP2. Among these, I selected the brightest reference star, Gaia DR3 3096359610087012480, with a magnitude ($G_{\mathrm{mag}}$) of 13.57,

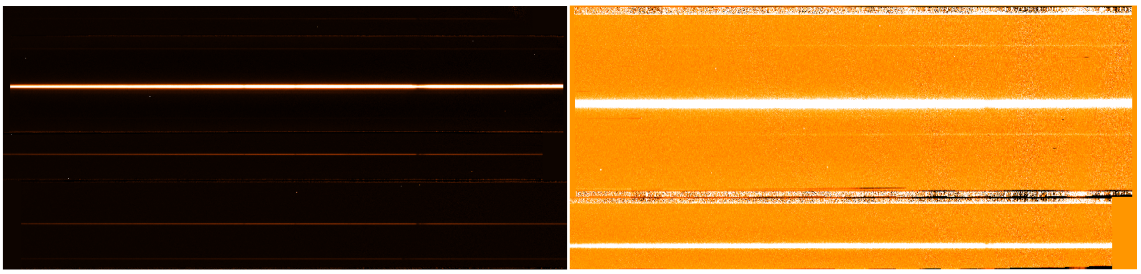

Figure 3.6: Left and right panel sample reduced spectra (after wavelength calibration) of the target and reference star respectively, from the second night observation after the data reduction with `EsoReflex`. Here, the x-axis pixel corresponds to the wavelength direction, and the y-axis indicates the pixel's spatial direction.

located at the center of CHIP2, as our reference star. The other reference stars had insufficient SNR, making them unsuitable for reliable analysis. I separated the target star and reference star files as they were placed on different chips on the CCD and performed Gaussian fitting by making a cut in the region of interest to collect the maximum amount of light and observe the spectrum at its peak, as shown in the Figure 3.7. The flux from multiple exposures was combined by adding a spread: ± [(value)] sigma to obtain a comprehensive 1D spectrum. After careful analysis using the least-squares method on the light curves, optimal sigma values of 9 pixel and 15 pixel were determined for the blue and red grism observations respectively. These values were selected as they resulted in the lowest root mean square (RMS).

In order to ensure precise measurements in a stable reference frame, barycentric correction modified the observed wavelengths of a star's spectrum, due to Earth's motion (orbital and rotational) with respect to the solar system's barycenter. The correction was carried out using `PyAstronomy's`[5] `helcorr` function, which determines the correction velocity by using the geographic coordinates of the observatory, the celestial coordinates of the star, and the Julian Date observation time. The Doppler shift formula was then used to shift the observed wavelengths using the resulting barycentric velocity. The corrected spectra are then aligned with the barycentric reference frame. The reference star flux is much lower than the target star flux, implying that the reference star is much dimmer than our target; this can be seen in Figure 3.9.

### 3.3.2 Light Curves

As mentioned, to analyze the transit of HAT-P-30 b, I processed the spectra from 1556 files in total using the developed Python script. The most suitable reference star - Gaia DR3 3096359610087012480 ($G_{\mathrm{mag}} = 13.57$) for our analysis was located at the center of CHIP2. The selection of this reference star ensures the highest SNR for our analysis and minimizes systematic errors caused by weaker or less stable stars in the field, and is important to get precise telluric correction and accurate normalization of the light curves.

[5] https://pyastronomy.readthedocs.io/en/latest/

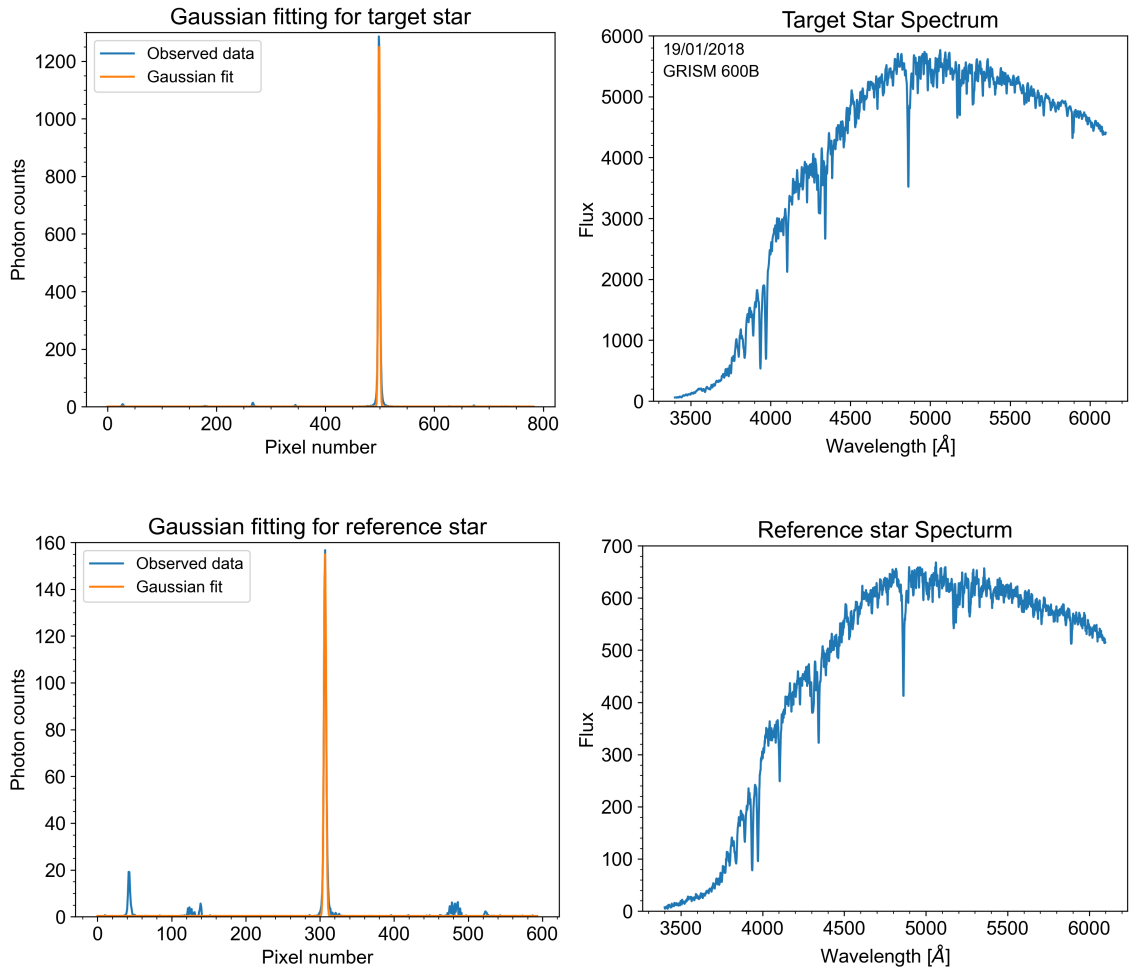


Figure 3.7: Gaussian fitting and spectral extraction applied to HAT-P-30's first-night observations with grism 600B. The top-left panel illustrates the Gaussian fitting used on the 2D target star file for spectral extraction, while the top-right panel presents the target star's spectra after Gaussian fitting. Similarly, the bottom-left panel demonstrates the Gaussian fitting applied to the 2D reference star file, and the bottom-right panel displays the reference star's spectra post-Gaussian fitting.

The spectra were divided into 23 total wavelength bins, each with a bin width of 170 Å and 280 Å for first and second nights data, respectively, for the main analysis. For the first night's observations, flux values below 4000 Å were excluded due to low SNR, while for the second night, flux values below 5300 Å were discarded for the same reason. The light curves for each bin were calculated by summing the flux within the corresponding wavelength range of each frame. These were then normalized by dividing each flux value by the mean flux of the out-of-transit points. To account for the effects of the Earth's atmosphere, which introduces telluric contamination through absorption features, the light curves of HAT-P-30 were corrected by dividing them by the corresponding light curves of a reference star, following established methods (Nikolov et al., 2018; Sedaghati et al., 2017). This approach ensures the removal of atmospheric effects, particularly prominent in the infrared but also present in optical wavelengths.

Wavelength-integrated white-light curves were similarly created by summing the flux over specific wavelength ranges for both the target and the reference star, following the same normalization and telluric correction process. This normalization yielded the raw light curves for both stars, as shown in the topmost rows of Figures 3.10 and 3.11. To refine the data further, a polynomial fit was applied to the out-of-transit points of the normalized white-light curve to remove residual trends. A quadratic model provided the best fit for the white-light curves, resulting in detrended light curves, illustrated in the middle rows of Figures 3.10 and 3.11. The bottom rows of these figures present the clean transit signals observed for both nights. For the binned light curves, a linear model in time was found to provide the best fit.

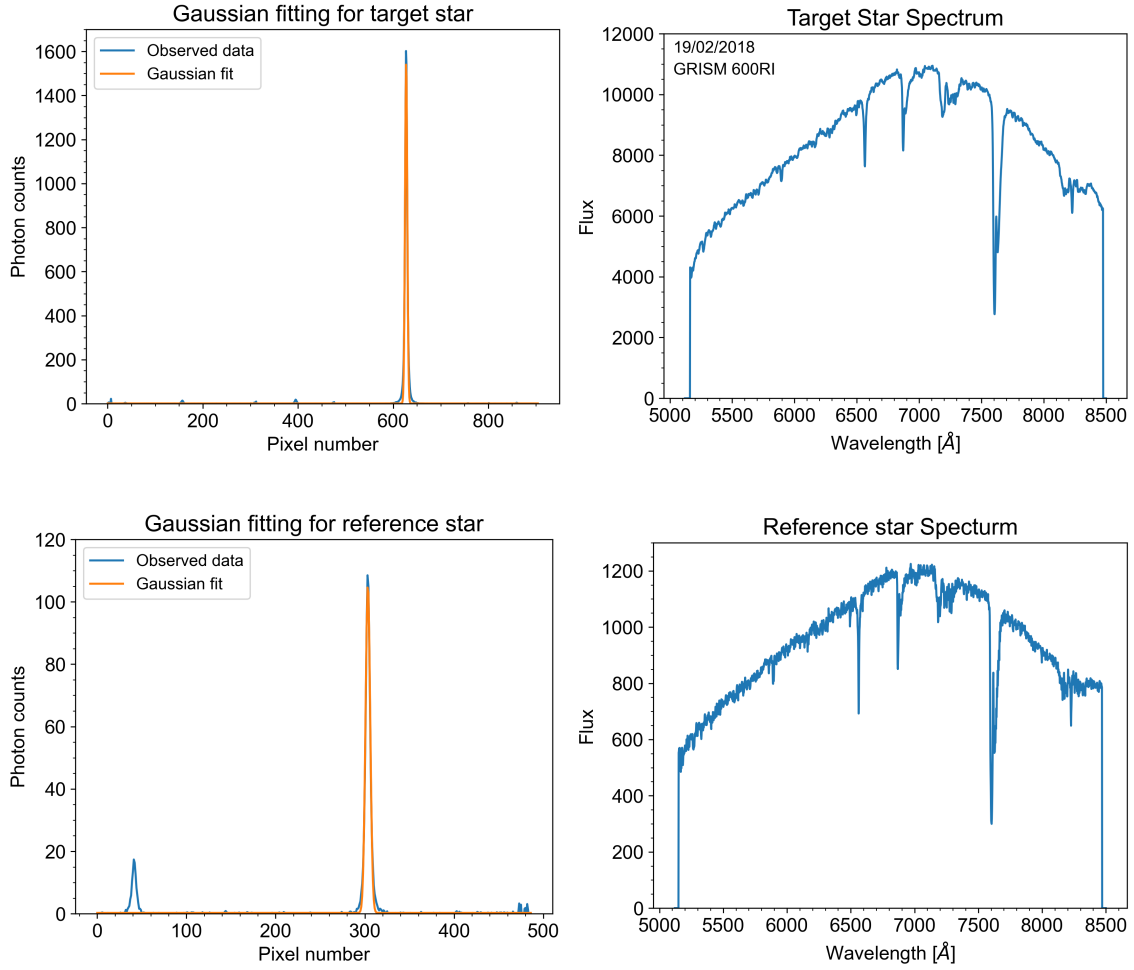


Figure 3.8: Illustration of the Gaussian fitting and spectra extraction performed on HAT-P-30's second-night observations using grism `600RI`. The top-left panel shows the Gaussian fitting performed on the 2D target star file to extract the spectra, while the top-right panel presents the corresponding spectra of the target star after Gaussian fitting. The bottom-left panel presents the Gaussian fitting on the 2D file of the reference star for spectra extraction, and the bottom-right panel displays the reference star's spectra after Gaussian fitting.

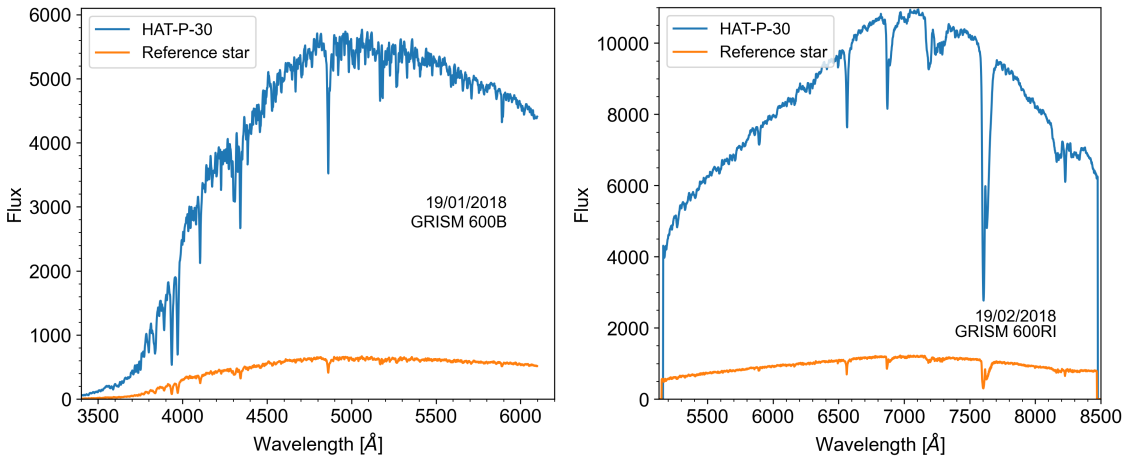


Figure 3.9: Left and right panels show example stellar spectra used for relative spectrophotometric calibration obtained using the `GRIS600B` (blue) and `GRIS600RI` (red) datasets, respectively. The flux comparison of our target HAT-P-30 to the reference star implies that the reference star is much dimmer than our target.

## 3.4 Gaussian Processes (GP) Regression

I modeled the white-light transits and accounted for systematic effects by treating the data as GP. The detrending of the white-light and binned light curves was carried out using the `Tiberius` software package, as detailed in Section 2.3.1. `Tiberius` utilizes the GPPM transit model class, which uses `batman` to generate the analytic, quadratically limb-darkened transit light curves, and `george`[6] to generate the GP red noise models. The white-light curve GP initial fitting parameters included the ratio of the planet to star radius $R_P/R_S$, the inclination $i$ of the planet, the quadratic limb-darkening coefficients $u_1$ and $u_2$, the scaled semi-major axis $a/R_S$ and the time of mid-transit $T_C$. Additional ancillary parameters (hyperparameters) were used to describe detrending functions, as explained below.

First, the planetary parameters $a/R_S$, $i$, and $T_C$ were fitted for the white-light light curve, as shown in Table 3.2. Gaussian priors were chosen for all system parameters, with lower and upper limits set to three times the respective error from the literature values (Table 3.1). The Limb Darkening Toolkit (Parviainen and Aigrain, 2015) was utilized to compute the limb darkening coefficients, incorporating uncertainties propagated from the stellar parameter errors based on Phoenix models (Husser et al., 2013). A quadratic limb-darkening law was applied, with one coefficient ($u_2$) held fixed to avoid degeneracies, following the approach used by Nikolov et al. (2018). The prior for $u_1$ was set as uniform, centered at the generated value with a range corresponding to three times the generated error. To fit for relative changes in transit depths over the wavelength range, the parameter values derived from the white-light curve were fixed for the subsequent analysis of binned light curves. This was done by fitting the planet to stellar radii ratio $R_P/R_S$, and $u_1$ for each wavelength bin using GP regression.

[6] https://george.readthedocs.io/en/latest/

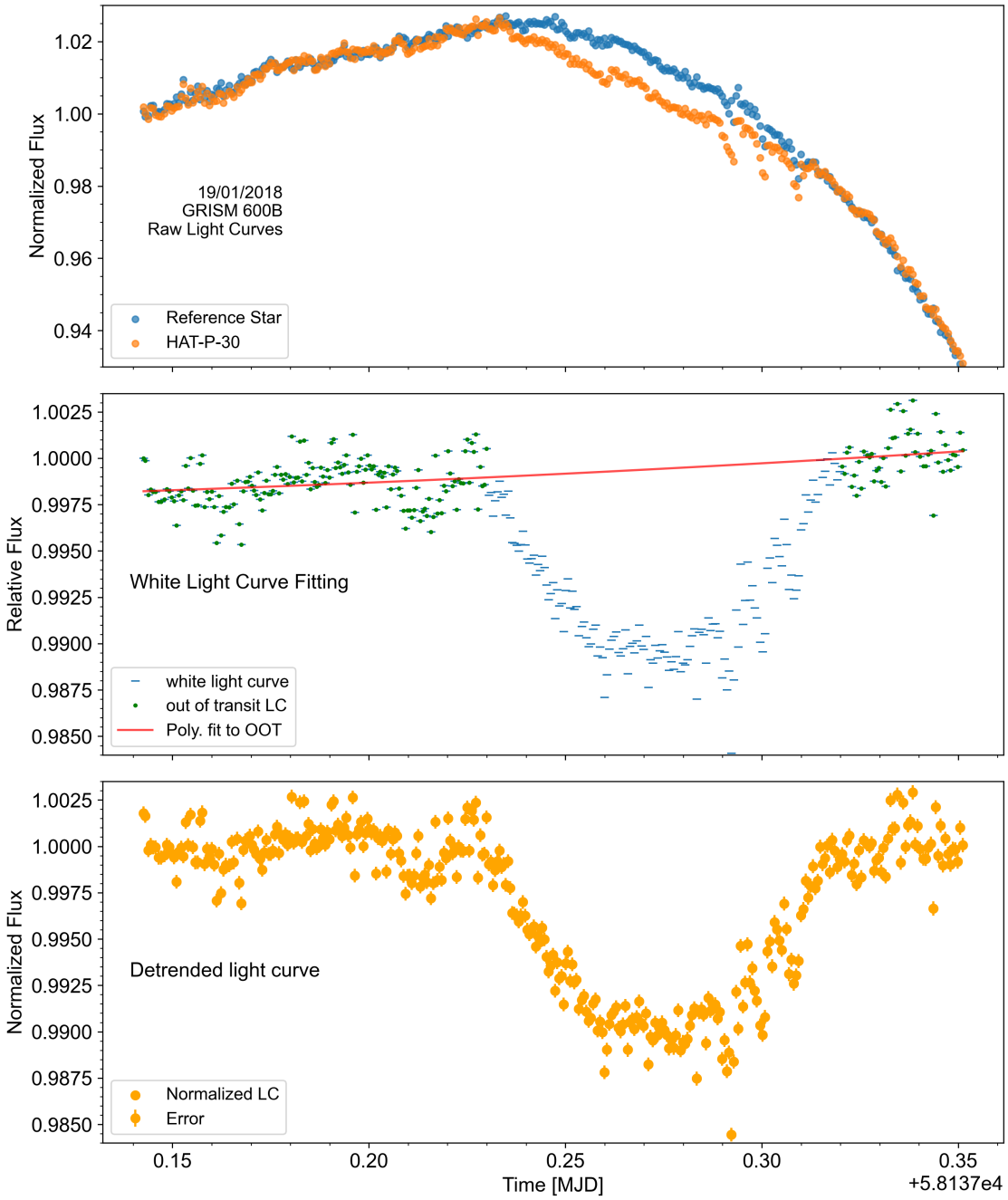


Figure 3.10: First transit observations of HAT-P-30 b using grism 600B. The first row presents the individual normalized raw light curves for the target and reference stars. The second row depicts the quadratic polynomial fit of the normalized relative flux. And, the third row showcases the detrended transit light curve.

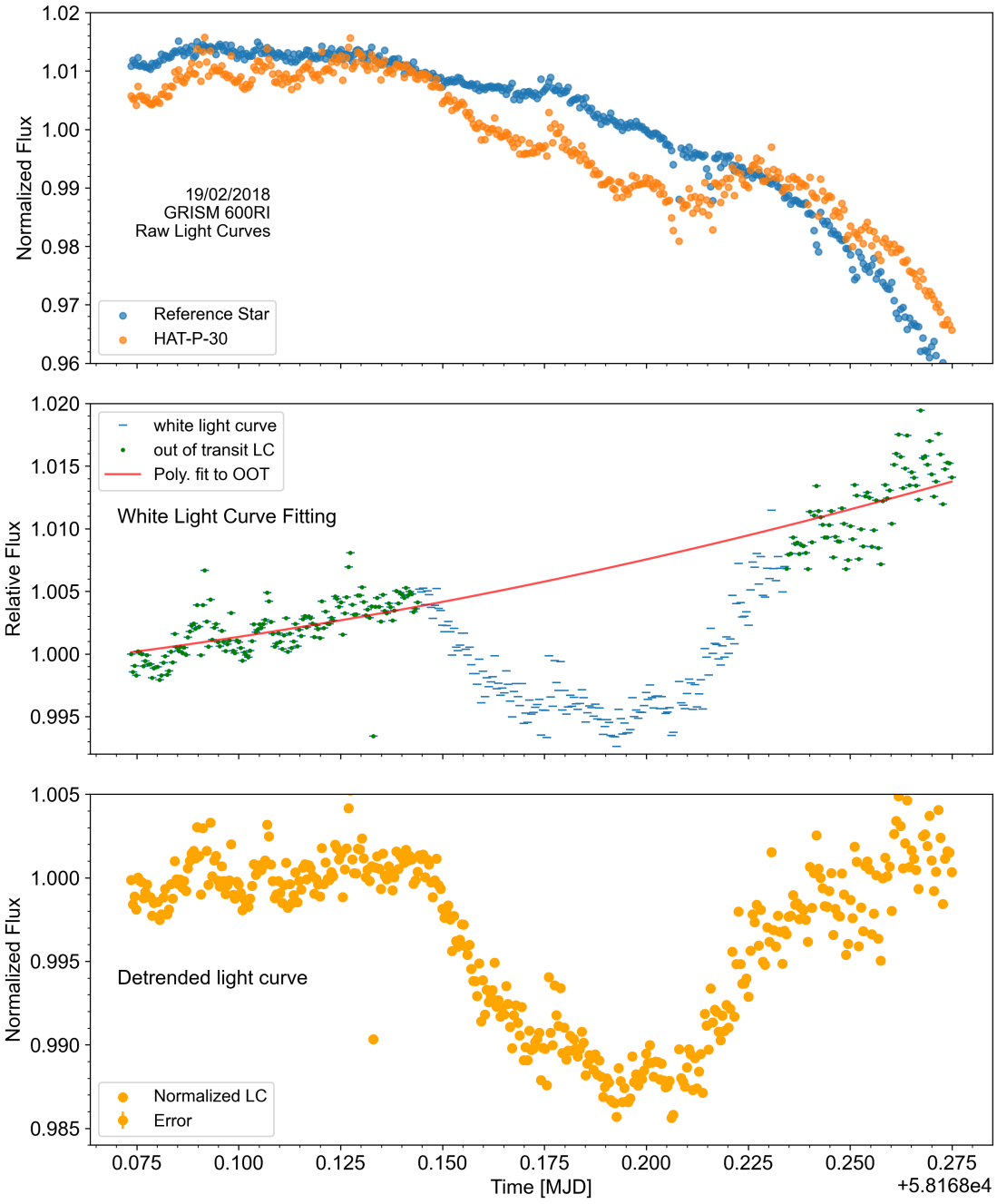


Figure 3.11: Second night observations of HAT-P-30 b with grism `600RI`. The first row presents the normalized raw light curves for both the target and reference stars. The second row illustrates the quadratic polynomial fit of the normalized relative flux. The third row displays the detrended transit light curve.

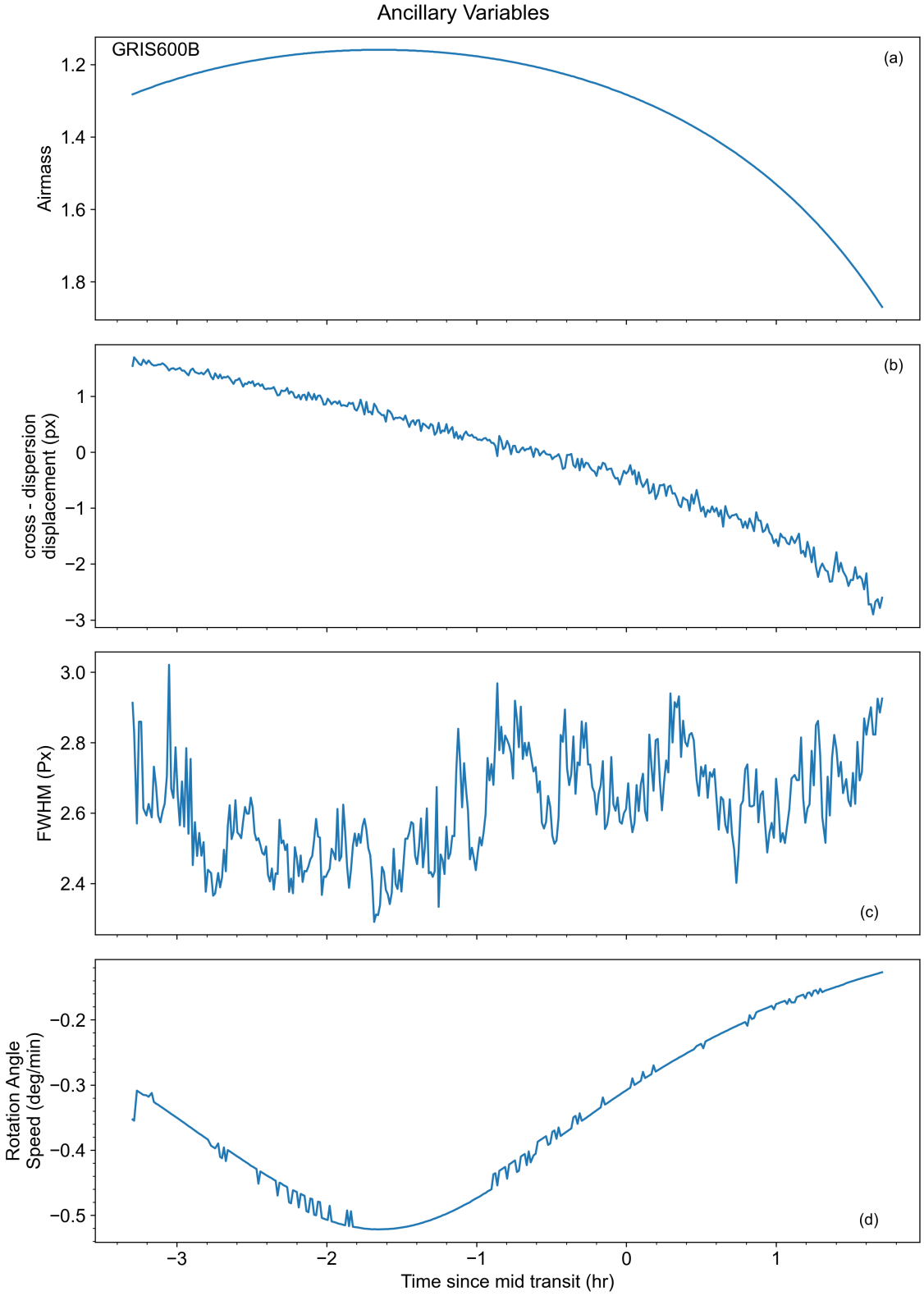


Figure 3.12: FORS2 (VLT) observations of HAT-P-30 b using the `GRIS600B` grism. Time-series of hyperparameters/ancillary variables: (a) Airmass, (b) Drift along the cross-dispersion direction, (c) Full Width at Half Maximum (FWHM) of the spectral profile, and (d) Rate of change of the rotation angle. Time is shown on the x-axis for all panels.

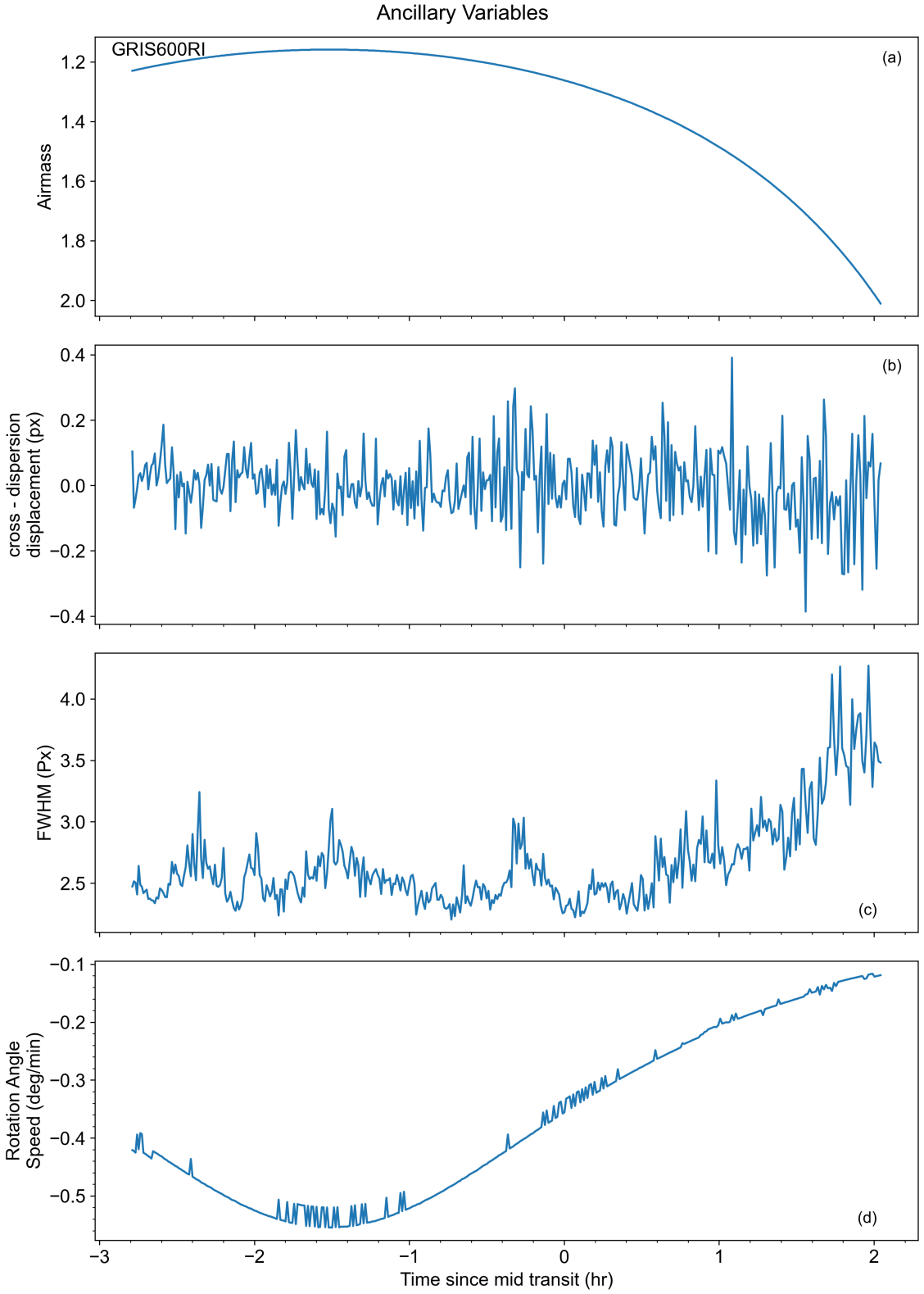


Figure 3.13: FORS2 (VLT) observations of HAT-P-30 b using the `GRIS600RI` grism. Time-series of hyperparameters/ancillary variables: (a) Airmass, (b) Drift along the cross-dispersion direction, (c) Full Width at Half Maximum (FWHM) of the spectral profile, and (d) Rate of change of the rotation angle. The x-axis represents time in all panels.

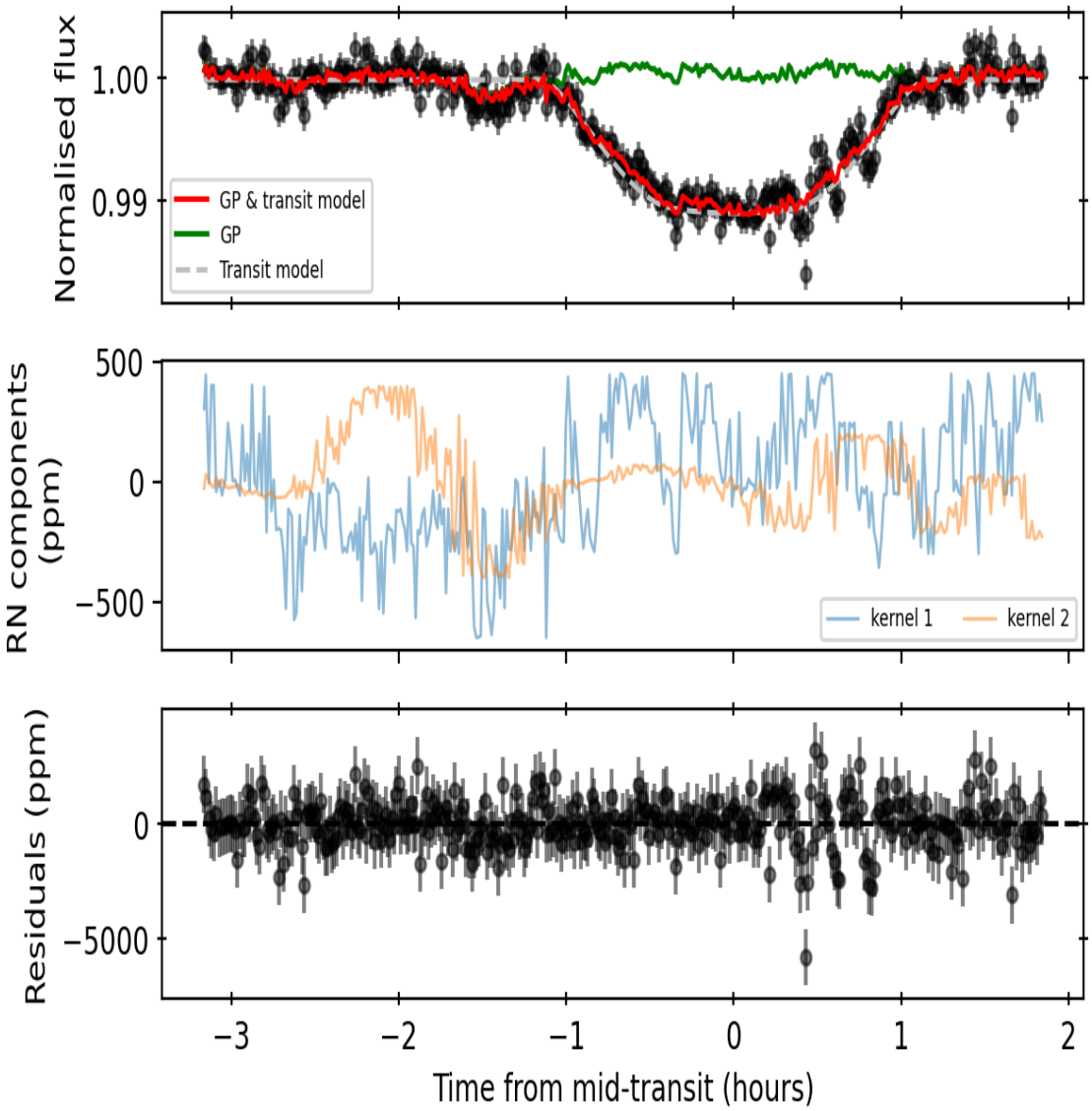


Figure 3.14: White-light transit light curve analysis of HAT-P-30 b using GP modeling. The red line shows the best-fitting model, while the dashed grey line represents the transit model, and the green line refers to the overall GP model.
(Top panel): presents the observed transit data and the fitted model.
(Middle panel): illustrates the GP components, showing the effects of cross-dispersion displacement (orange) and FWHM (blue).
(Bottom panel): displays the residuals between the data and the best-fit model.

Although the white-light curve was manually fitted with a quadratic time model, I observed that binned light curves produced better results when polynomial detrending functions (linear models) were simultaneously fitted during the GP regression, incorporating ancillary data/hyperparameters such as FWHM, cross-dispersion displacement (cdd), ras and airmass. The hyperparameters describing the covariance functions between data points in GP modeling were extracted from the FITS headers of the stellar observations, as shown in Figures 3.12 & 3.13. These hyperparameters served as kernel inputs for the GP regression, as outlined in Section 2.3.1. To optimize the modeling process, I tested various combinations of kernel inputs and found that two kernel inputs (FWHM and cdd) processing with Matern

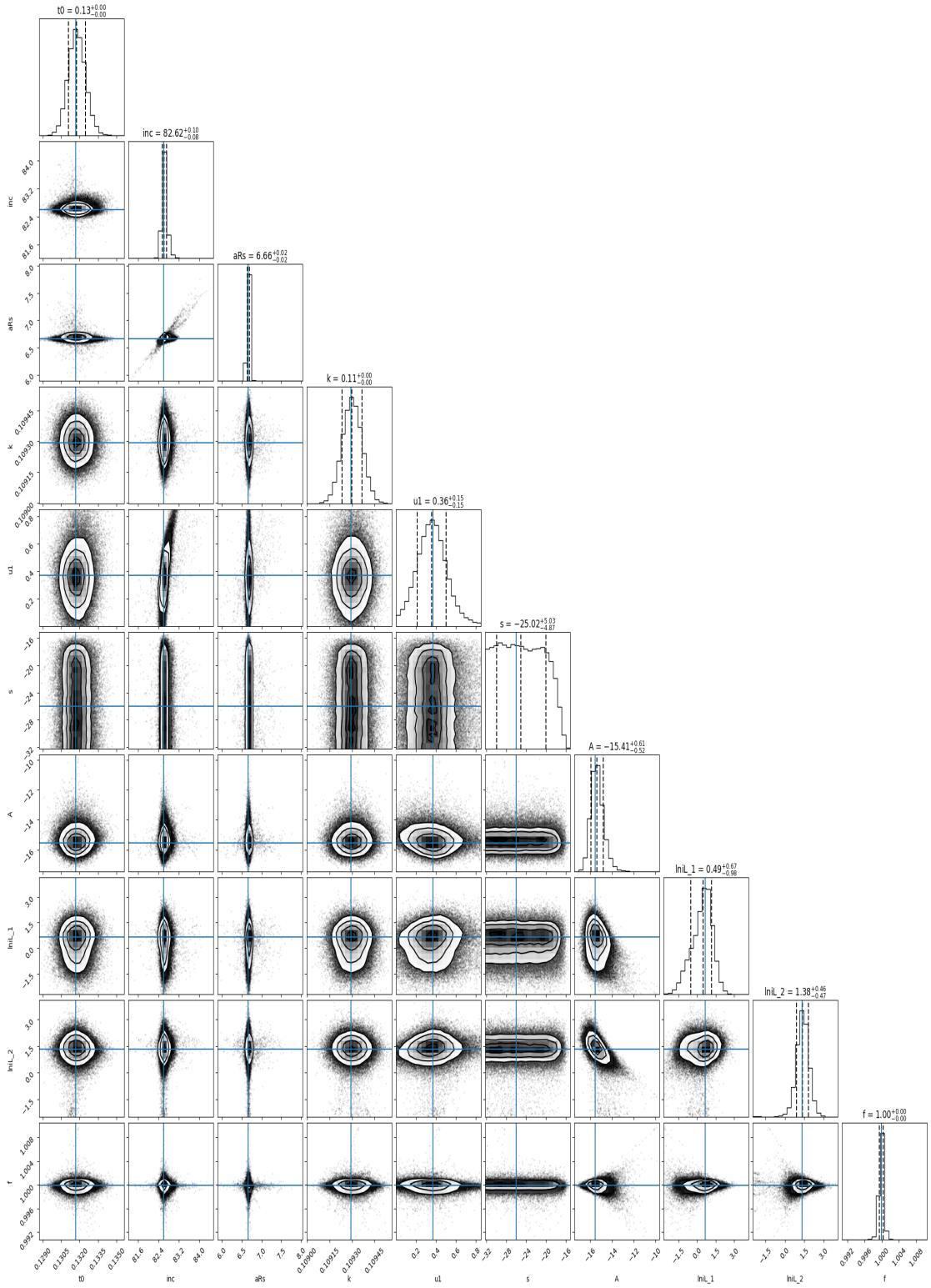


Figure 3.15: Corner plot of the posterior distributions for the fitted parameters from the white-light light curve analysis of HAT-P-30 b first-night observations, including GP to model systematics. The transit parameters include the inclination ($i°$), scaled semi-major axis ($a/R_S$), planet-to-star radius ratio ($R_P/R_S$), and limb-darkening coefficient ($u_1$), while the GP is described by the amplitude A. The most likely posterior value is indicated by blue lines in the plots. A summary of all retrieved parameters and their prior distributions is provided in Table 3.3.

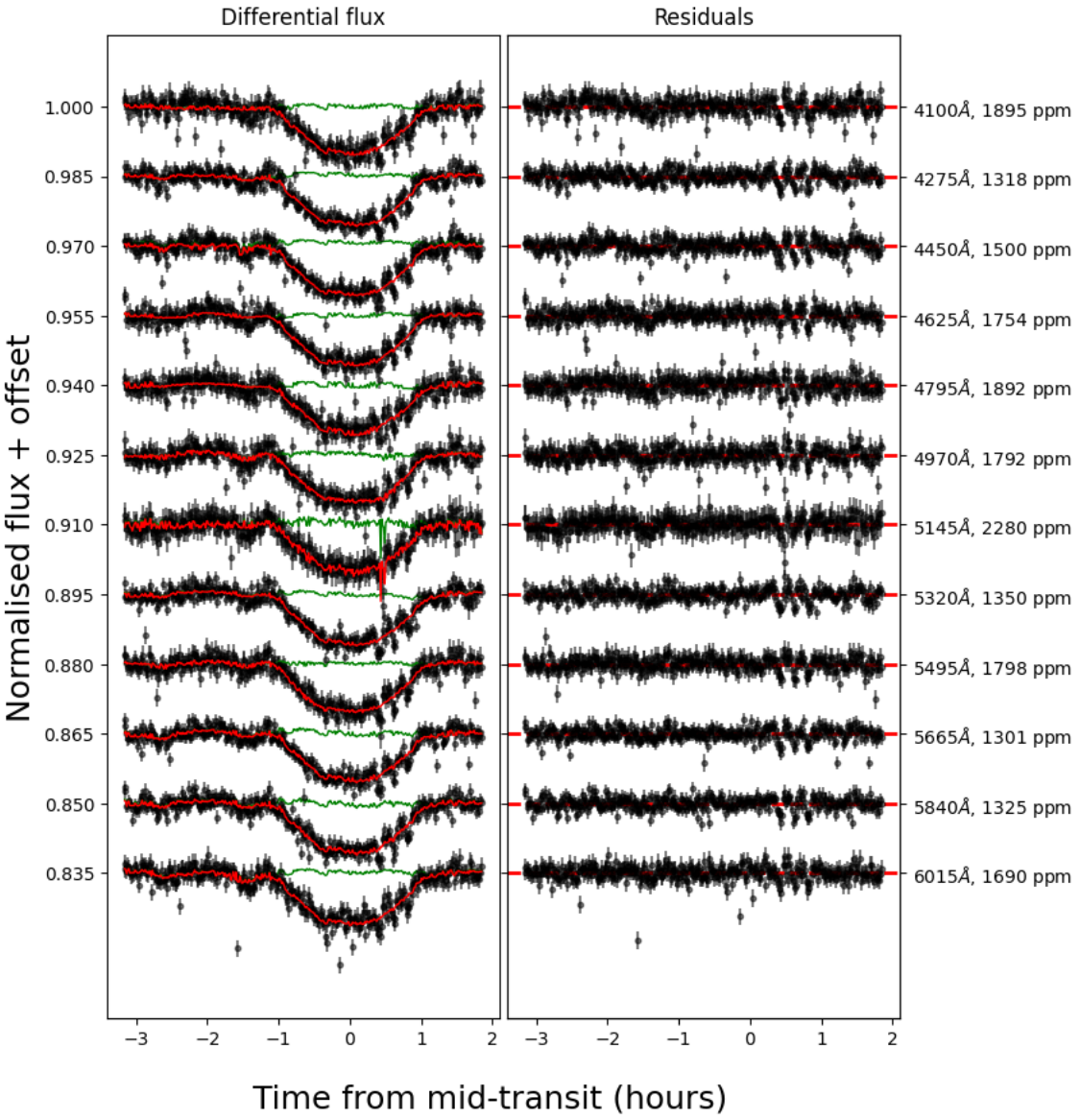


Figure 3.16: Left panel shows spectrophotometric light curves for individual wavelength bins, shown with the fitted transit model (red line). Right panel shows residuals corresponding to the spectroscopic light curves. From grism 600B.

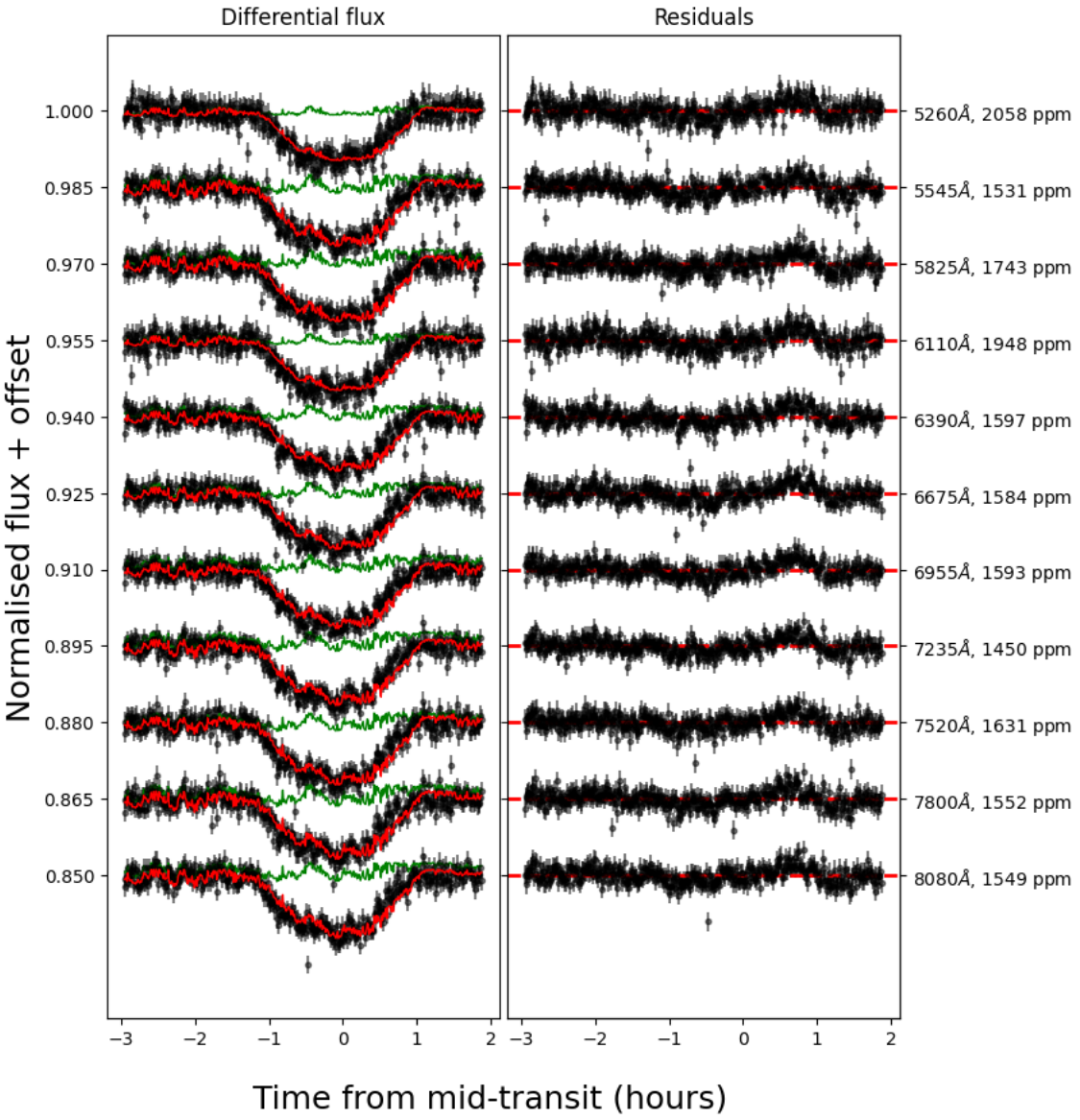


Figure 3.17: Left panel shows spectrophotometric light curves for individual wavelength bins, shown with the fitted transit model (red line). Right panel shows residuals corresponding to the spectroscopic light curves. From grism `600RI`

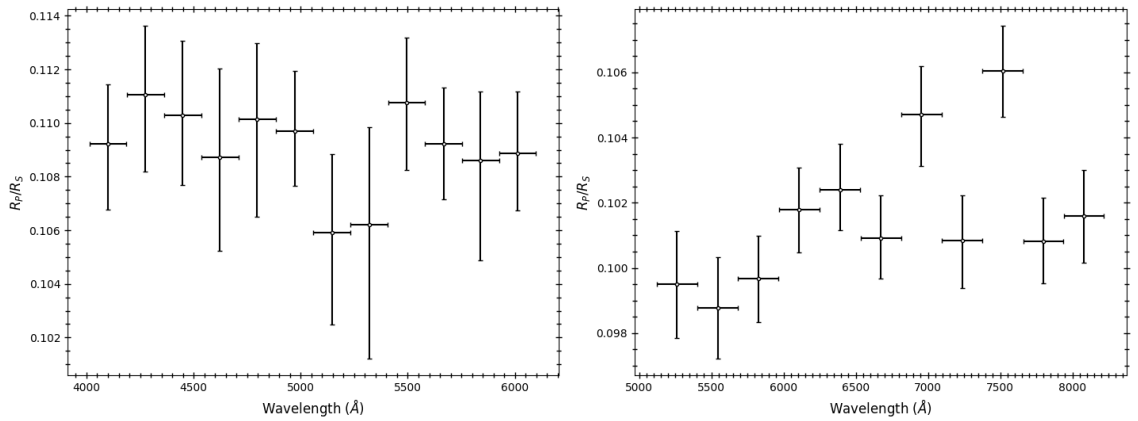


Figure 3.18: Indicated are the relative radius measurements of HAT-P-30 b with `Tiberius`, from grism `600B` (left panel) and `600RI` (right panel). An outlier point at 7500 Å in right panel, could be an indication of presence of potassium (K) in atmosphere of HAT-P-30 b.

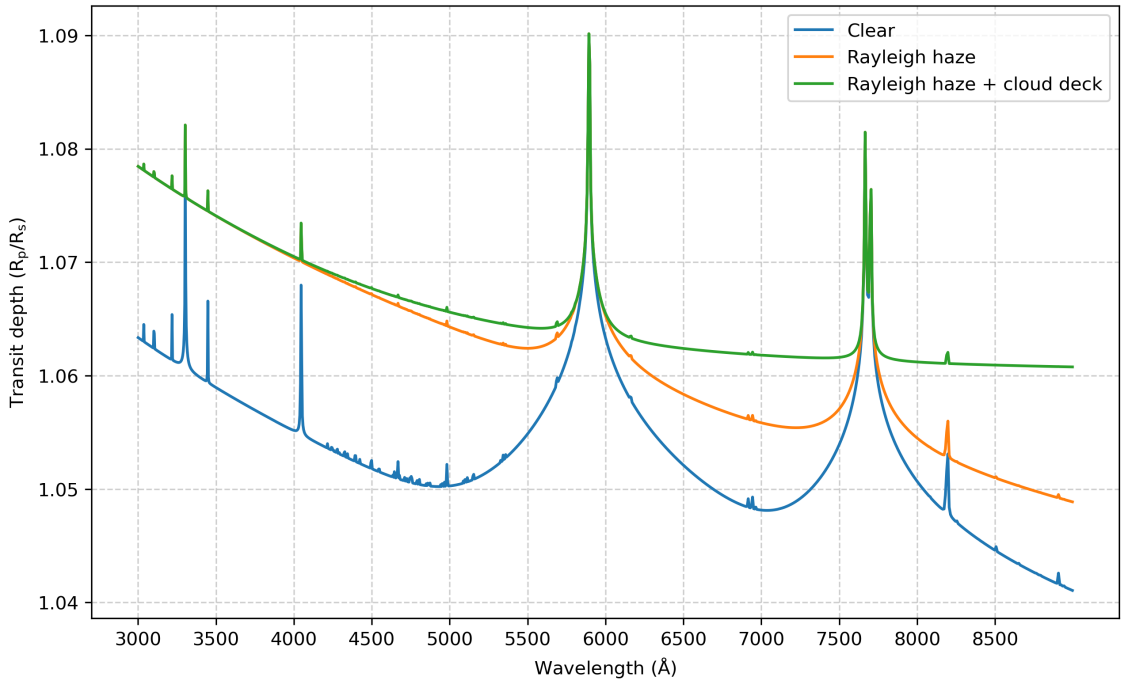


Figure 3.19: HAT-P-30 b's transmission spectrum forward modelled assuming a clear atmosphere with different line broadening shapes for Na and K. Models with hazes or clouds (orange and green) predict much smaller and narrower absorption features.

3/2 kernels (described in 2.3.1) were sufficient to effectively remove red noise[7] from the white-light curve. These optimized inputs were used in the final analysis. The resulting fit parameters for the white-light curve are mentioned in the table 3.2; the white-light curve fit is presented in Figure 3.14, where the contributions of the GP from FWHM and cross-dispersion are shown in blue and orange, respectively. Furthermore, the posterior distributions of the white light curve fit, including the

[7]Red noise refers to a type of noise that is more concentrated at lower frequencies, generally $\propto 1/f^2$

Table 3.2: The parameter values obtained from fitting the white-light curve, incorporating both polynomial and GP detrending methods.

| Grism | Parameter | Fitted values |
|---|---|---|
| 600 B | Scaled semi-major axis $a/R_S$ | $6.664^{+0.024}_{-0.024}$ |
| | Inclination $i$ (°) | $82.624^{+0.097}_{-0.079}$ |
| | Planet-to-star radius ratio $R_P/R_S$ | $0.109299^{+0.000066}_{-0.000065}$ |
| | Limb-darkening coefficient $u_1$ | $0.357^{+0.145}_{-0.146}$ |
| | Limb-darkening coefficient $u_2$ | 0.1482 (fixed) |
| 600 RI | Scaled semi major axis $a/R_S$ | $6.665^{+0.024}_{-0.023}$ |
| | Inclination $i$ (°) | $82.672^{+0.047}_{-0.049}$ |
| | Planet-to-star radius ratio $R_P/R_S$ | $0.109314^{+0.000065}_{-0.000065}$ |
| | Limb-darkening coefficient $u_1$ | $0.432611^{+0.000358}_{-0.000360}$ |
| | Limb-darkening coefficient $u_2$ | 0.1648 (fixed) |

GP hyperparameters, are presented in Figure 3.15.

I fitted all 23 spectrophotometric bins using shared GP hyperparameters for the length scale to model the common noise structure and allowing separately varying amplitude and white noise for each light curve. This method guaranteed more consistent detrending across adjacent wavelength bins despite its computational cost. The natural logarithm of the inverse length scale of the kernel inputs for the FWHM and cross dispersion displacement were the two parameters that were common to all 23 bins. The planetary to stellar radii ratio ($R_P/R_S$) and the limb-darkening coefficient $u_1$, all these distinct parameters were fitted simultaneously for each spectrophotometric light curve. Figures 3.16 and 3.17 shows the fitted spectroscopic light curves and retrieved planet-to-star radius ratio values of HAT-P-30 b are recorded in Table 3.3.

## 3.5 Results and Discussions

The transmission spectrum of HAT-P-30 b in Figure 3.18 appears relatively featureless in grism `600B`, with no detectable sodium absorption or scattering slope, but the outlier around 7500 Å in grism `600RI` indicates that the presence of potassium (K) (7650-7700 Å) is plausible, when compared to the transmission spectrum model of HAT-P-30 b in Figure 3.19 derived using PetitRADTRANS (Mollière et al., 2019). However, the planet-to-star radius ratio of the left figure corresponding to grism `600B` in Figure 3.18 does not fit well with those corresponding to grism `600RI` in the same figure. Since they were taken on different nights, the data corresponding to both the grisms could have had a probable impact on the results, though more attention needs to be focused. The observed spectrum does not accurately match

Table 3.3: Retrieved transmission spectrum of HAT-P-30 b in tabulated form using GP detrending as plotted in as seen in 3.18.

| Bin (Å) | $R_p/R_s$ | $u_1$ | $u_2$ |
|---|---|---|---|
| 4013-4186 | $0.1092^{+0.0022}_{-0.0024}$ | $0.7243^{+0.0006}_{-0.0006}$ | 0.0934 |
| 4187-4360 | $0.1111^{+0.0026}_{-0.0029}$ | $0.7172^{+0.0004}_{-0.0004}$ | 0.1066 |
| 4361-4534 | $0.1103^{+0.0028}_{-0.0026}$ | $0.6844^{+0.0005}_{-0.0005}$ | 0.1184 |
| 4535-4708 | $0.1087^{+0.0033}_{-0.0035}$ | $0.6454^{+0.0005}_{-0.0005}$ | 0.1288 |
| 4710-4883 | $0.1101^{+0.0029}_{-0.0036}$ | $0.5899^{+0.0006}_{-0.0006}$ | 0.1378 |
| 4884-5057 | $0.1097^{+0.0023}_{-0.0020}$ | $0.5913^{+0.0005}_{-0.0005}$ | 0.1453 |
| 5058-5231 | $0.1059^{+0.0029}_{-0.0034}$ | $0.5699^{+0.0004}_{-0.0004}$ | 0.1514 |
| 5232-5405 | $0.1062^{+0.0036}_{-0.0050}$ | $0.5461^{+0.0004}_{-0.0004}$ | 0.1561 |
| 5407-5579 | $0.1108^{+0.0024}_{-0.0025}$ | $0.5316^{+0.0004}_{-0.0004}$ | 0.1594 |
| 5581-5752 | $0.1092^{+0.0021}_{-0.0021}$ | $0.5104^{+0.0004}_{-0.0005}$ | 0.1613 |
| 5754-5925 | $0.1086^{+0.0026}_{-0.0037}$ | $0.4964^{+0.0004}_{-0.0005}$ | 0.1618 |
| 5927-6098 | $0.1089^{+0.0023}_{-0.0021}$ | $0.4794^{+0.0005}_{-0.0005}$ | 0.1608 |
| 5121-5401 | $0.0995^{+0.0016}_{-0.0017}$ | $0.5560^{+0.0003}_{-0.0004}$ | 0.0934 |
| 5403-5683 | $0.0988^{+0.0016}_{-0.0016}$ | $0.5230^{+0.0004}_{-0.0004}$ | 0.1066 |
| 5685-5965 | $0.0997^{+0.0013}_{-0.0013}$ | $0.4942^{+0.0004}_{-0.0004}$ | 0.1184 |
| 5967-6247 | $0.1018^{+0.0013}_{-0.0013}$ | $0.4707^{+0.0003}_{-0.0003}$ | 0.1288 |
| 6249-6530 | $0.1024^{+0.0014}_{-0.0012}$ | $0.4428^{+0.0004}_{-0.0004}$ | 0.1378 |
| 6531-6812 | $0.1009^{+0.0013}_{-0.0013}$ | $0.4045^{+0.0004}_{-0.0004}$ | 0.1453 |
| 6814-7094 | $0.1047^{+0.0015}_{-0.0016}$ | $0.4084^{+0.0004}_{-0.0004}$ | 0.1514 |
| 7096-7376 | $0.1008^{+0.0014}_{-0.0015}$ | $0.4489^{+0.0003}_{-0.0003}$ | 0.1561 |
| 7378-7657 | $0.1061^{+0.0014}_{-0.0014}$ | $0.5517^{+0.0003}_{-0.0004}$ | 0.1594 |
| 7658-7937 | $0.1008^{+0.0013}_{-0.0013}$ | $0.3569^{+0.0003}_{-0.0003}$ | 0.1613 |
| 7939-8218 | $0.1016^{+0.0014}_{-0.0014}$ | $0.3481^{+0.0003}_{-0.0004}$ | 0.1618 |

the expected atmospheric model, suggesting possible limitations in the data quality or retrieval process. One of the primary challenges in this analysis was due to the observations and the low SNR of the reference star, it being dimmer than the target star, HAT-P-30. This brightness discrepancy is evident in the flux comparison plot (Figure 3.9), where the lower flux levels of the reference star contributed to the increase in uncertainties in the derived spectrum.

Additionally, during observations, the reference star was positioned near a faulty pixel row on the detector, likely leading to a loss of crucial spectral information and further reducing the SNR (see the bottom left panel in the acquisition images 3.3, 3.4). Despite this, the reference star spectrum was successfully extracted using a Gaussian fitting, as shown in Figures 3.7 and 3.8. However, the reduced brightness of the reference star, in comparison to the target, resulted in larger error bars in the transmission spectrum.

Ideally, a reference star should be of similar brightness and have a similar B–V color index to the target star to ensure reliable ground-based low-resolution transmission spectroscopy. The discrepancies in brightness observed in this study underscore the importance of careful reference star selection in future observations to improve data accuracy and minimize uncertainties.

# Chapter 4

# WASP-96 b

In order to help guide my analysis of the exoplanet HAT-P-30 b, I realized that I would need a reference planet with a well-studied atmosphere. WASP-96 b is classified as a "hot Saturn" (refer 4.1 for planetary parameters) and turned out to be a perfect choice due to its unique, cloud-free atmosphere and detailed spectral data. It orbits around a chromospherically quiet and photometrically stable G8-type star with an apparent magnitude (V) of 12.2, located about 356 ± 5 parsecs away in the constellation Phoenix (Hellier et al., 2014). The transmission spectrum of WASP-96 b, obtained with the VLT, shows a complete, pressure-broadened sodium absorption profile (Nikolov et al., 2018). Precise measurements of atmospheric potassium and sodium abundances (or other components), which are often partially obscured in other exoplanetary atmospheres, are made possible due to its cloud-free atmosphere. Initially, I performed data reduction, developed a code and obtained results for WASP-96 and compared my results with those previously published in Nikolov et al. (2018), to verify the reliability of my method. After validation, I used the same methodology described in Chapter 3 for my target exoplanet, HAT-P-30 b. In this section, I will briefly describe the process, along with a summary of the main conclusions for WASP-96 b.

## 4.1 Observations

Transits of WASP-96 b were observed on two nights, the first on 2017 July 29, with 600B (blue) grism, with the observing time around ∼ 5.4 hours. The ingress started at 06:57 UT and the egress at 09:24 UT, making the transit event last for about ∼ 2.45 hours[1]. The second observing night was on 2017 August 22 UT, using 600RI (red) in photometric conditions, using the FORS2 spectrograph on the 8.2-m Unit Telescope 1 of the VLT. Data from the two transit observations were collected in a similar way as that of HAT-P-30 b, and were downloaded from the ESO archive services[2]. I decided not to use the data from second night's observation; the reason

[1] https://exoplanetarchive.ipac.caltech.edu/cgi-bin/TransitView/nph-visibletbls?dataset=transits

[2] http://archive.eso.org/eso/eso_archive_main.html

is explained in Section 4.2. The observational setup of WASP-96 b gathered using P2demo[3] is shown in Figure 4.1, and the raw acquisition images from the transit observation run of WASP-96 b is shown in Figure 4.2.

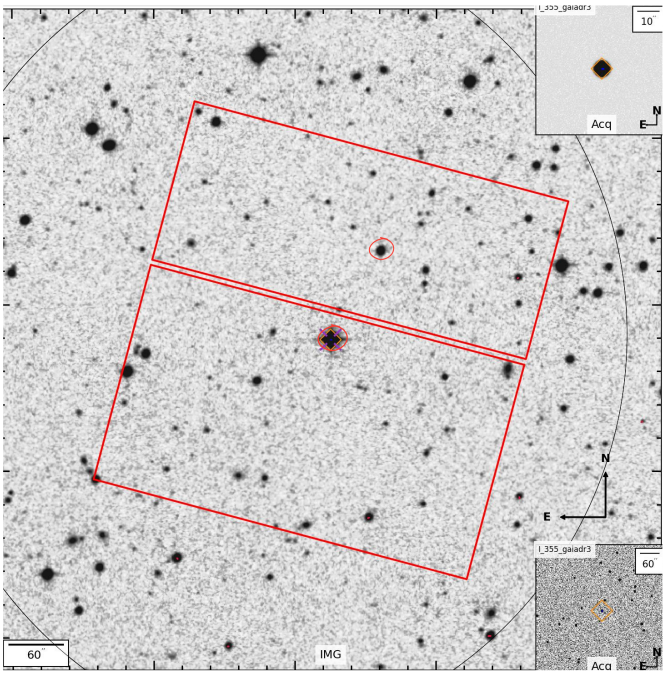


Figure 4.1: Observational set up of WASP-96, observed under program ID 199.C-0467(H) by project PI. The red lines outline the two-chip detector mosaic. In the instance shown, highlighted by red circles, WASP-96 is on the lower slit, and Gaia DR3 4990047799410930304 is on the upper slit as the reference star. Image taken from P2demo.

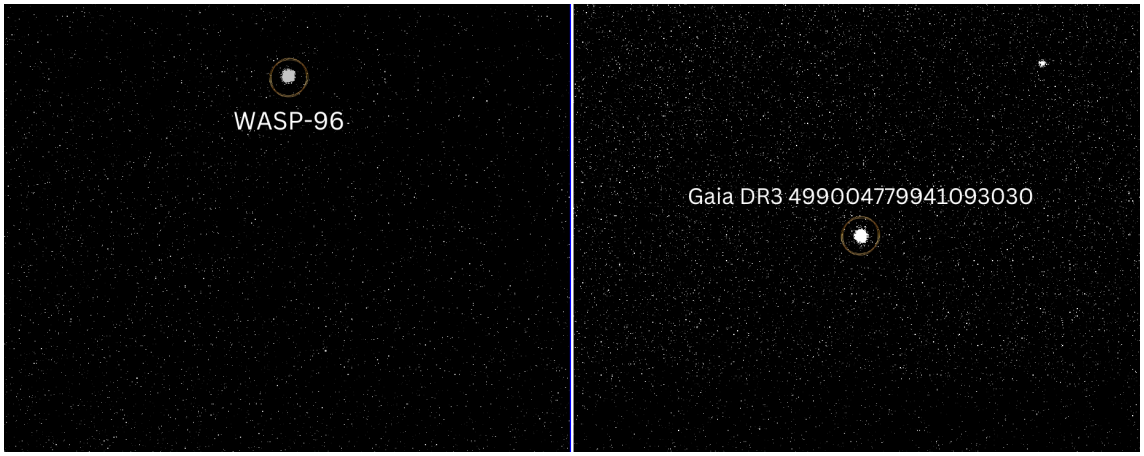


Figure 4.2: Raw acquisition frames of WASP-96 from the first night observed using the grism 600B (blue).
Left panel: shows the target star positioned on CHIP1.
Right panel: presents the reference star on CHIP2.

[3] https://www.eso.org/p2demo/home/run/60900301

Table 4.1: Stellar and planetary parameters of a WASP-96. Values are taken from Hellier et al. (2014).

| | Parameter | Value |
|---|---|---|
| Star | Spectral Type | G8 |
| | $V_{mag}$ | 12.2 |
| | Mass, $M_*$ ($M_\odot$) | 1.06 ± 0.09 |
| | Radius, $R_*$ ($R_\odot$) | 1.05 ± 0.05 |
| | vsin $i_*$ (km/s) | 1.5 ± 1.3 |
| | Effective temperature, $T_{eff}$ (K) | 5500± 150 |
| | Metallicity, [Fe/H] | +0.14 ± 0.19 |
| Planet b | Period, P (days) | 3.4252602 ± 0.0000027 |
| | Semi-major axis, a (au) | 0.0453 ± 0.0013 |
| | Mass, $M_P$ ($M_{\rm Jup}$ ) | 0.48 ± 0.003 |
| | Radius, $R_P$ ($R_{\rm Jup}$ ) | 1.20 ± 0.06 |
| | Inclination, $i$ ($^\circ$) | 85.6 ± 0.2 |
| | Equilibrium temperature, $T_{\rm eq}$ (K) | 1286 ± 40 |
| | Impact parameter, $b$ | 0.710 ± 0.019 |

## 4.2 Data Reduction and Spectrum extraction

Data reduction for WASP-96 was carried out with `EsoReflex` using the same methodology as described in Section 3.2. The modified OCA file, tailored to reduce noise and ensure optimal fit as per the manual, was used. Most parameters remained unchanged, as they were pre-optimized in the `EsoReflex` pipeline on the basis of the grisms and spectra. The reduced spectra obtained from WASP-96 are shown in Figure 4.3 and 4.5. Gaussian fitting for spectrum extraction were performed similarly, using the techniques described in Section 3.3.1. To generate the 1D spectra, I followed the same approach as described earlier in Section 3.3.1, by combining flux from multiple exposures by adding a spread of ± sigma. Using the least-squares method to analyze the light curves, I determined that a sigma value of 13 pixels was optimal for both nights' data, as it minimized noise and gave the best results. The comparison star spectrum was extracted similarly; this is shown in Figure 4.4. As seen in the top right of Figure 4.5, flux values does not appear to be normal. This could have happened due to certain issues with the pipeline during the data reduction. Thus, to account for correct analysis, I normalised the flux values by multiplying it by 1000 so that it could be used for further analysis. However, we realized that even after normalizing, the target star spectrum is not as expected. On integrating the flux values and generating a white-light curve, extreme distortions were seen (Figure 4.8), distinct from a typically expected light curve. Thus, I decided to work only with the data corresponding to the first night observations for further analysis.

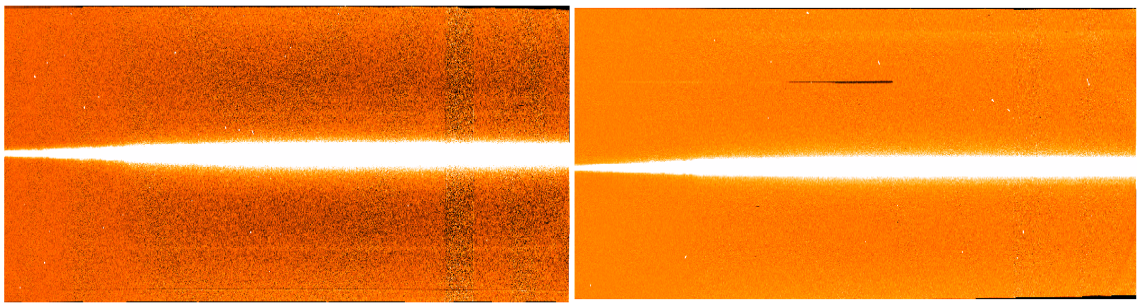

Figure 4.3: Left and the right panels show reduced spectra (after wavelength calibration) of the target and comparison star, respectively, from the first night observation after the data reduction with the `EsoReflex`. Here, the x-axis pixel represents wavelength direction, and the y-axis pixel indicates spatial direction.

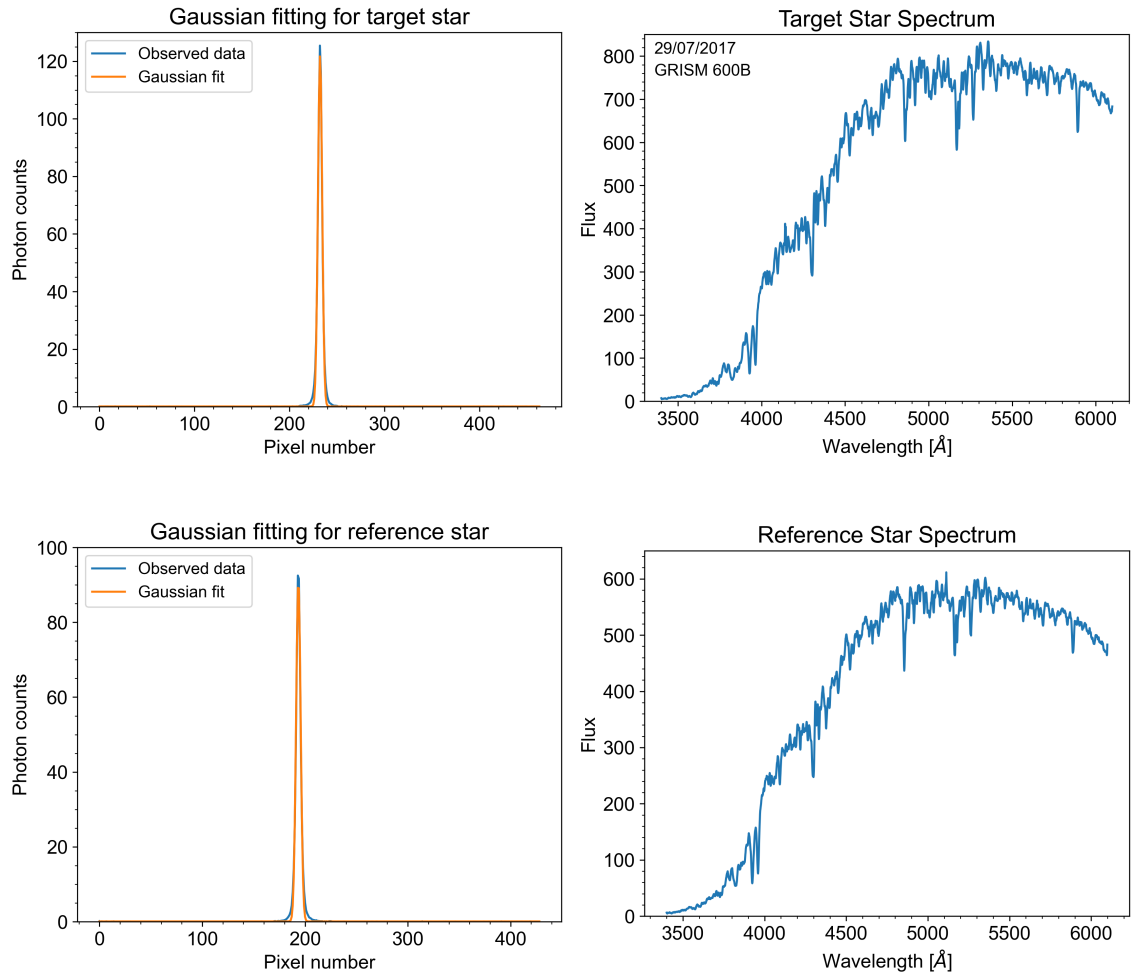


Figure 4.4: Illustration of the Gaussian fitting and spectra extraction performed on WASP-96's first-night observations using GRISM `600B`. The top-left panel shows the Gaussian fitting performed on the 2D target star file to extract the spectra, while the top-right panel presents the corresponding spectra of the target star after sky subtraction using Gaussian fitting. Similarly, the bottom-left panel depicts the Gaussian fitting on the 2D file of the reference star for spectra extraction, and the bottom-right panel displays the reference star's spectra after sky subtraction using Gaussian fitting.

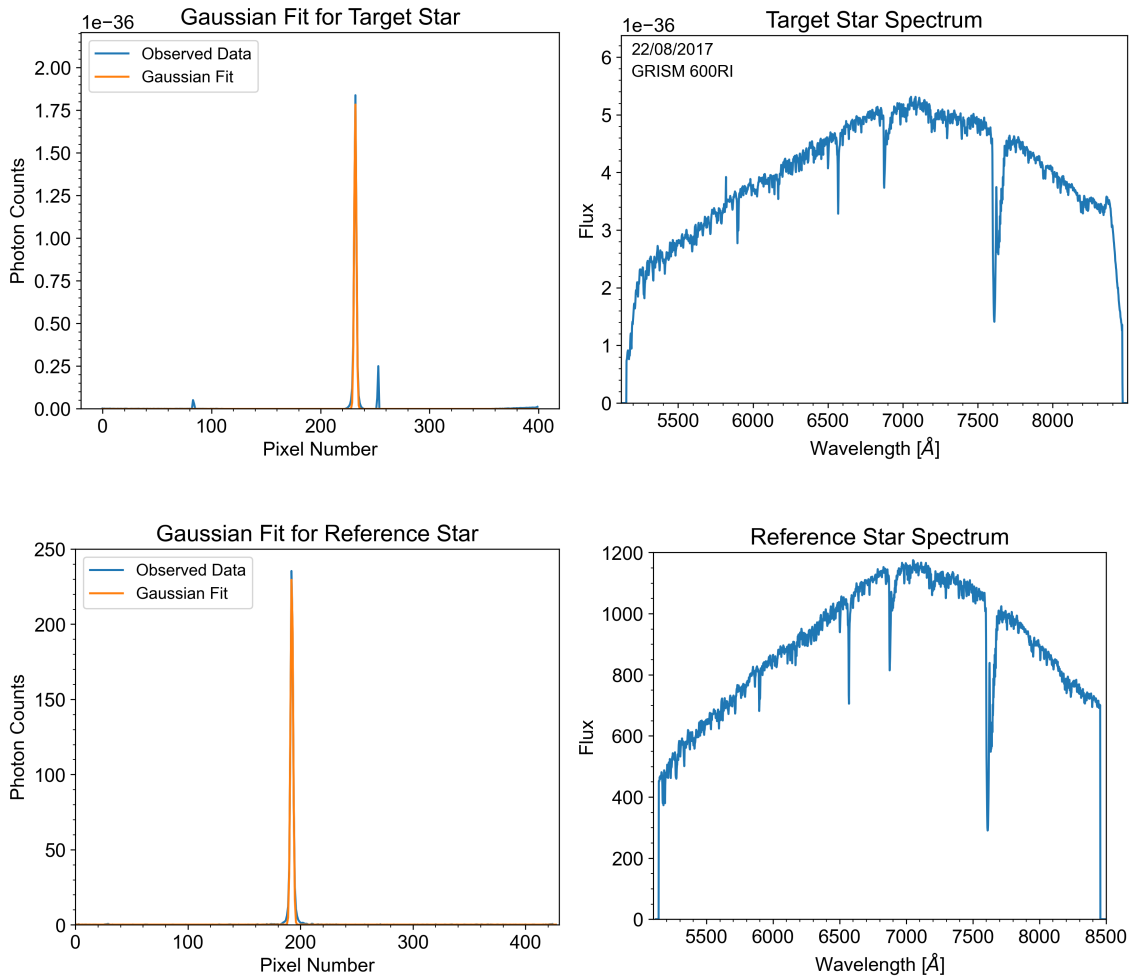


Figure 4.5: Gaussian fitting and spectral extraction applied to WASP-96's second-night observations with GRISM `600RI`. The top-left panel illustrates the Gaussian fitting used on the 2D target star file for spectral extraction, while the top-right panel presents the target star's spectra. Notice the flux scale in this plot. Similarly, the bottom-left panel demonstrates the Gaussian fitting applied to the 2D reference star file, and the bottom-right panel displays the reference star's spectra.

## 4.3 Light Curves

To analyze the transit of WASP-96 b, I followed a process similar to that described in Section 3.3.2. A total of 196 spectra from the first night and 474 spectra from the second night were processed using the developed Python script. A suitable reference star, Gaia DR3 4990047799410930304 ($G_{\mathrm{mag}} = 15.721666$), was identified by examining the field and evaluating the intensity peaks in the data to determine their brightness. The brightest peaks were located around pixels 230 and 190 on CHIP1 and CHIP2, respectively (see Figure 4.4). The wavelength-integrated white-light curve for WASP-96 b was created following the same steps. For the first night's observations, flux values from low-SNR wavelength regions were excluded before calculating the integrated flux. This was followed by normalization and telluric cor-

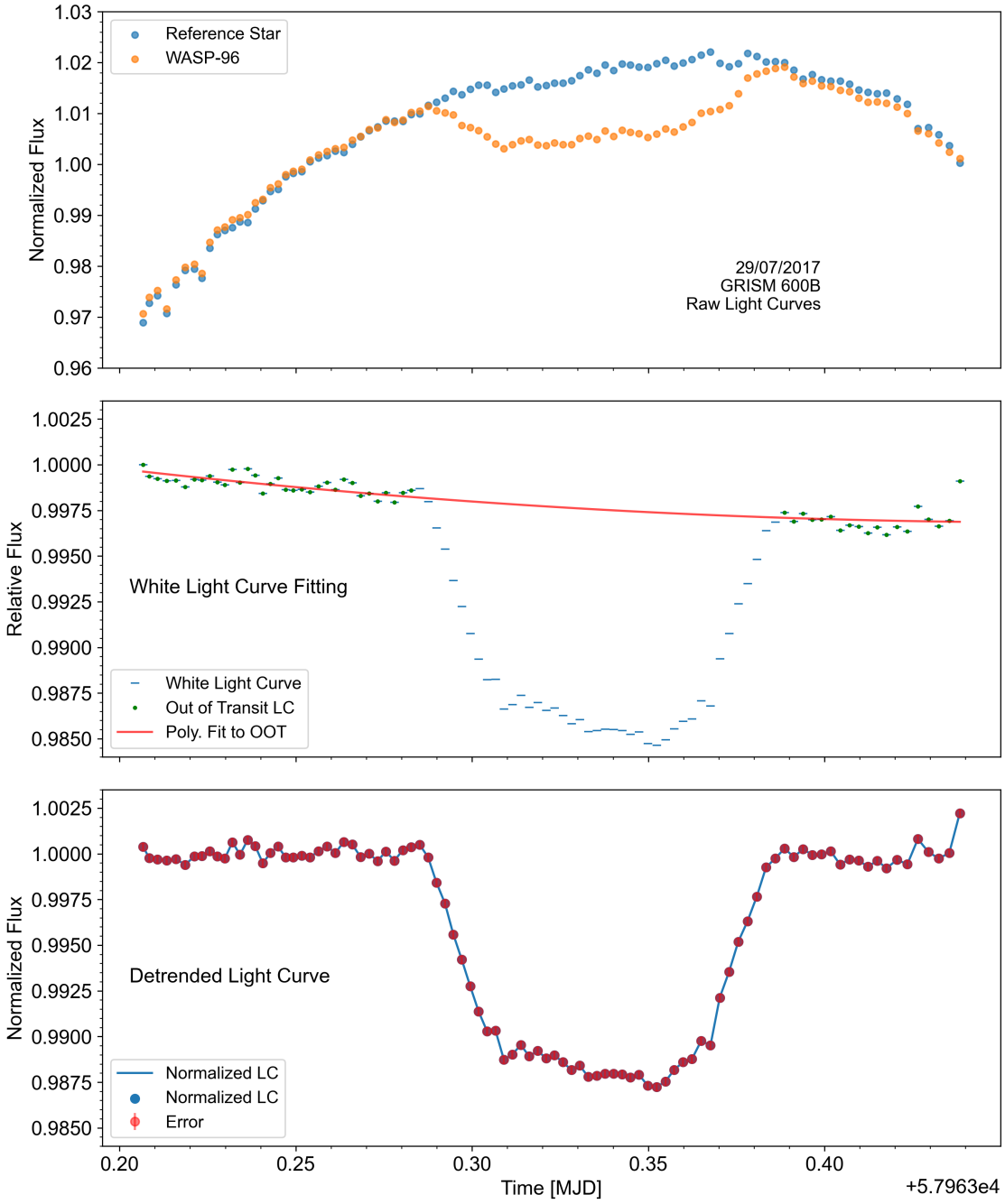


Figure 4.6: The first row displays the individual normalized raw light curves for WASP-96 and the reference star. The second row illustrates the quadratic-polynomial fitting of the normalized relative target-to-reference raw flux. Finally, the third row presents the detrended transit light curve for the first night of observations.

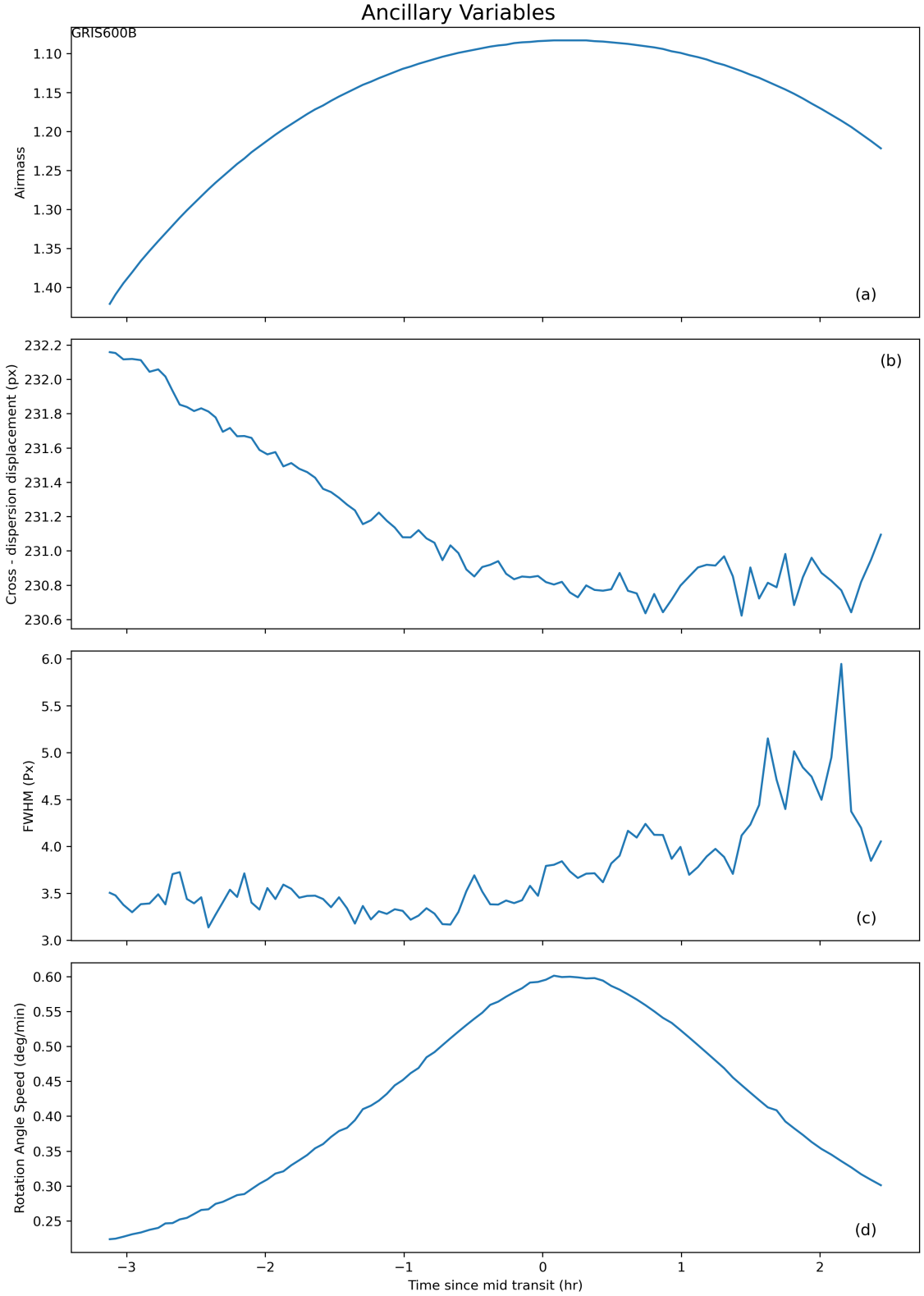


Figure 4.7: Observations of WASP-96 b using GRIS600B grism of FORS2 VLT. Time-series of the following hyperparameters/ancillary variables: (a) airmass; (b) drift along the direction of cross-dispersion; (c) the spectral profile's FWHM; and (d) the rotation angle's rate of change. For every panel, time is displayed on the x-axis.

rection using the reference star. However, the white-light curve obtained from the second night's data appeared distorted as shown in Figure 4.8, thus only the first night's observations were used, as the goal was to verify the methodology for the primary target, HAT-P-30 b. A quadratic fitting was applied to the out-of-transit points to detrend the light curve, resulting in the final transit signal shown in Figure 4.6.

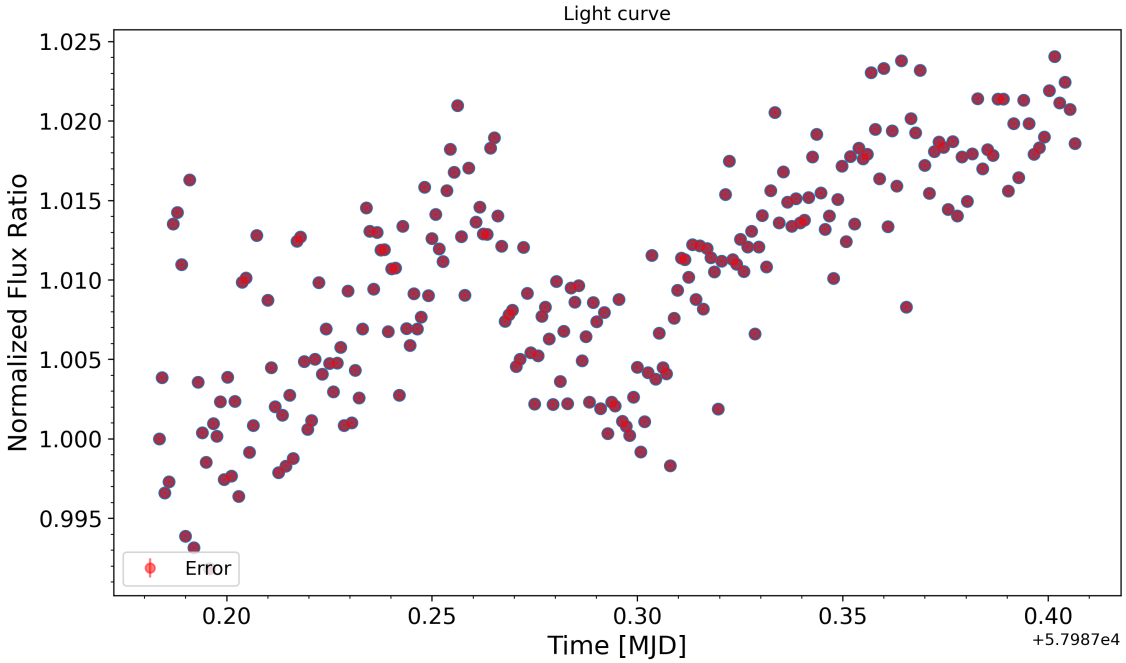


Figure 4.8: White light curve from the second night of observations of WASP-96 using the `600RI` grism. Unlike typical light curves, this one shows an unusual dip and appears to be highly noisy rather than displaying the expected smooth dip.

For the binned analysis, the spectra were divided into 18 wavelength bins, width of 144 Å. The Light curves for each bin were generated by summing the flux within the corresponding wavelength range and applying the same normalization and telluric correction process as described for HAT-P-30 b in Section 3.3.2. Further refinement was achieved by fitting a polynomial to the out-of-transit points of the normalized white-light curves, with a quadratic model providing the best fit for white-light curves and a linear model used for binned-light curves. The detrended light curves, displays clear transit signals, are shown in the bottom panels of Figures 3.10 and 3.11.

## 4.4 Gaussian Processes (GP) Regression

The transmission spectrum of the analysis of WASP-96 b was conducted using a methodology akin to that of the HAT-P-30 b (Section 3.4). Using `Tiberius` package, GP regression was used to detrend the white-light and binned light curves. $R_P/R_S$, $i$, $u_1$, $u_2$, $a/R_S$, and $T_C$ were the initial white-light curve parameters, $u_2$ was

fixed to avoid degeneracies.

Red noise was successfully decreased for detrending by processing two kernel inputs (FWHM and cross-dispersion displacement) using Matérn 3/2 kernels. In order to isolate the wavelength dependence of the transit depth, the parameters of the recovered white-light curve recorded in Table 4.2 were kept fixed for GP regression of the 18 spectrophotometric light curves. The fitted light curves with GP contributions are shown in Figures 4.9 and 4.11, while Figures 4.7 and 4.10 display the hyperparameters used for GP and posterior distributions, respectively. Table 4.3 and Figure 4.12 provides a summary of the transmission spectrum of the WASP-96 b.

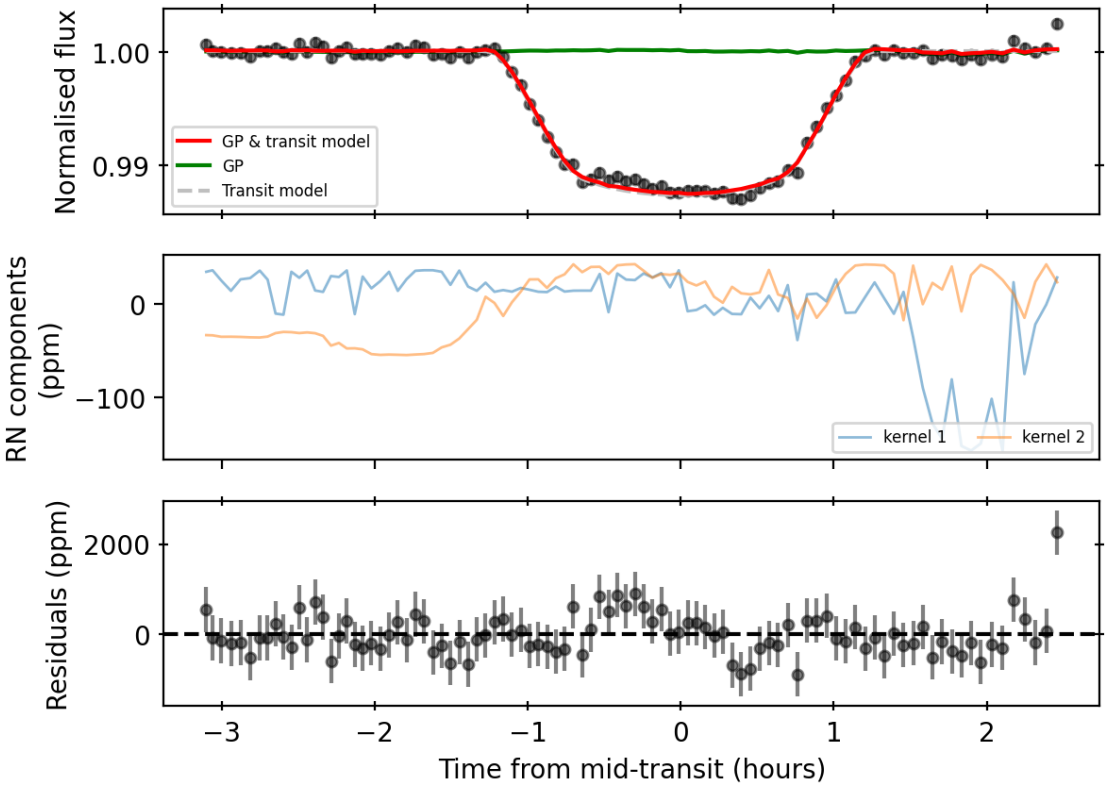


Figure 4.9: The white-light transit light curve of WASP-96 b (600B) fitted using a GP. The top panel shows the fitted light curve; the middle panel shows the contributions from the two GP kernel inputs: cross-dispersion displacement (blue) and FWHM (orange); the bottom panel shows residuals to the fit. The red line shows the best-fitting model, while the dashed grey line represents the transit model, and the green line refers to the overall GP model.

## 4.5 Results and Discussion

The use of GP modeling for removing trends in transit data worked effectively. It successfully identified and accounted for systematic noise in the data, allowing for accurate measurement of key parameters. Additionally, the parameters estimated using the GP (Table 4.2 & Table 4.3) are comparable to values previously reported

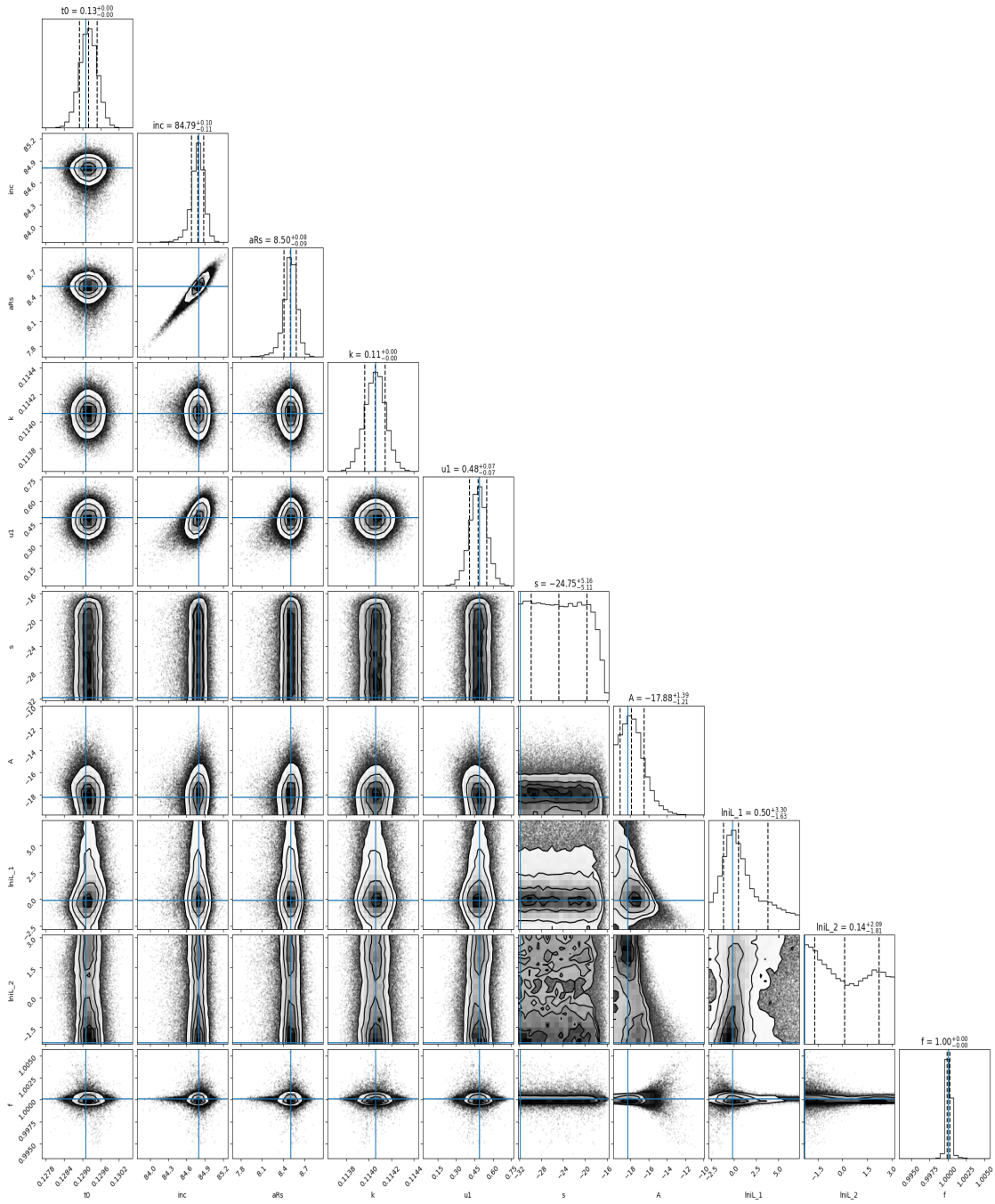


Figure 4.10: WASP-96 b first-night observations, corner plot of the posterior distributions for the fitted parameters from the white-light light curve analysis, including GP to model systematics. The transit parameters include the inclination ($i°$), scaled semi-major axis ($a/R_S$), planet-to-star radius ratio ($R_P/R_S$), and limb-darkening coefficient ($u_1$), while the GP is described by the amplitude A. Blue lines in the plots are the most likely posterior value. A summary of all retrieved parameters and their prior distributions is provided in Table 4.3.

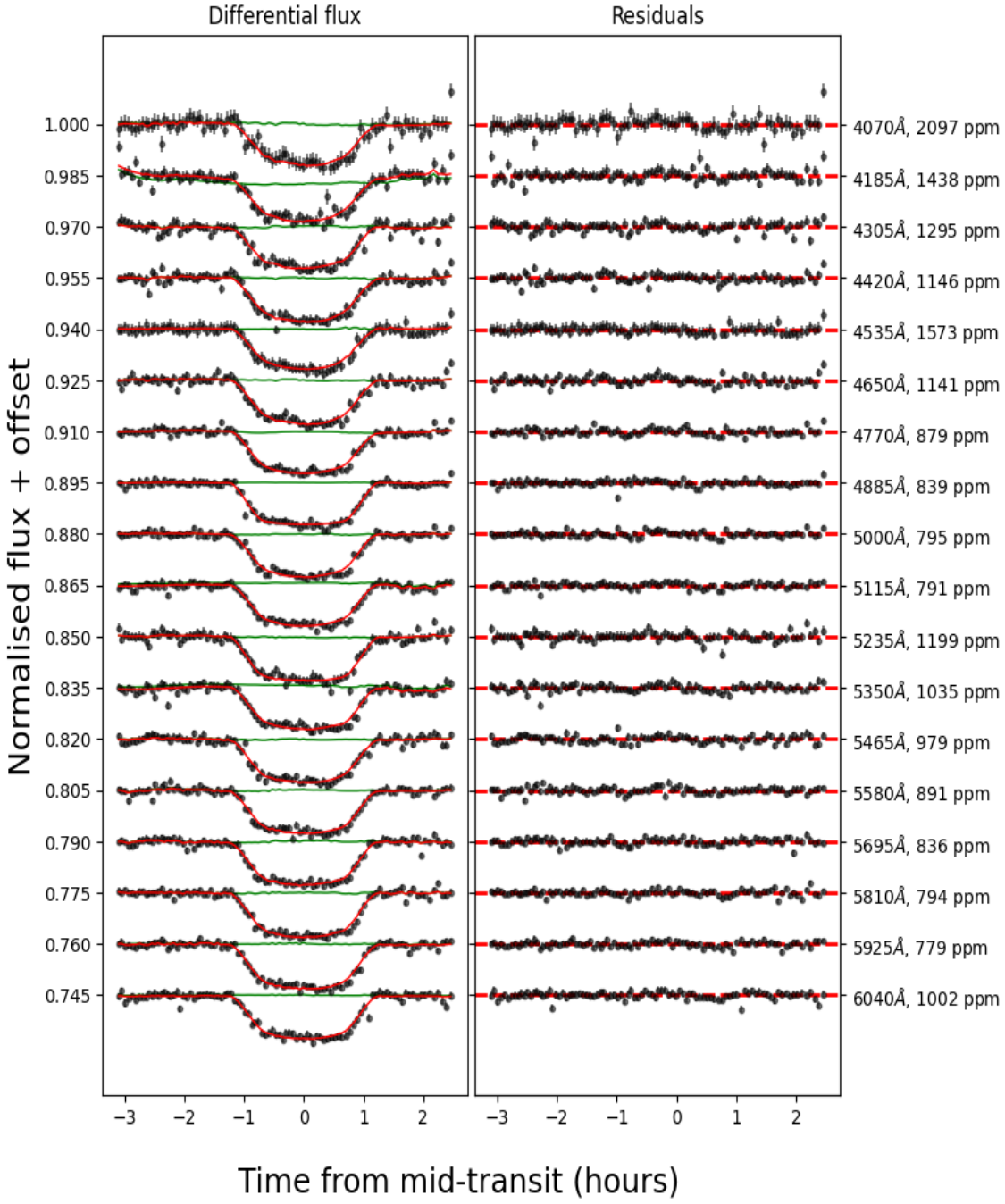


Figure 4.11: Spectrophotometric light curves of WASP-96 from grism 600B. The first panel shows the detrended light curves and the transit model (indicated with red dotted lines). The second panel shows residuals with error bars.

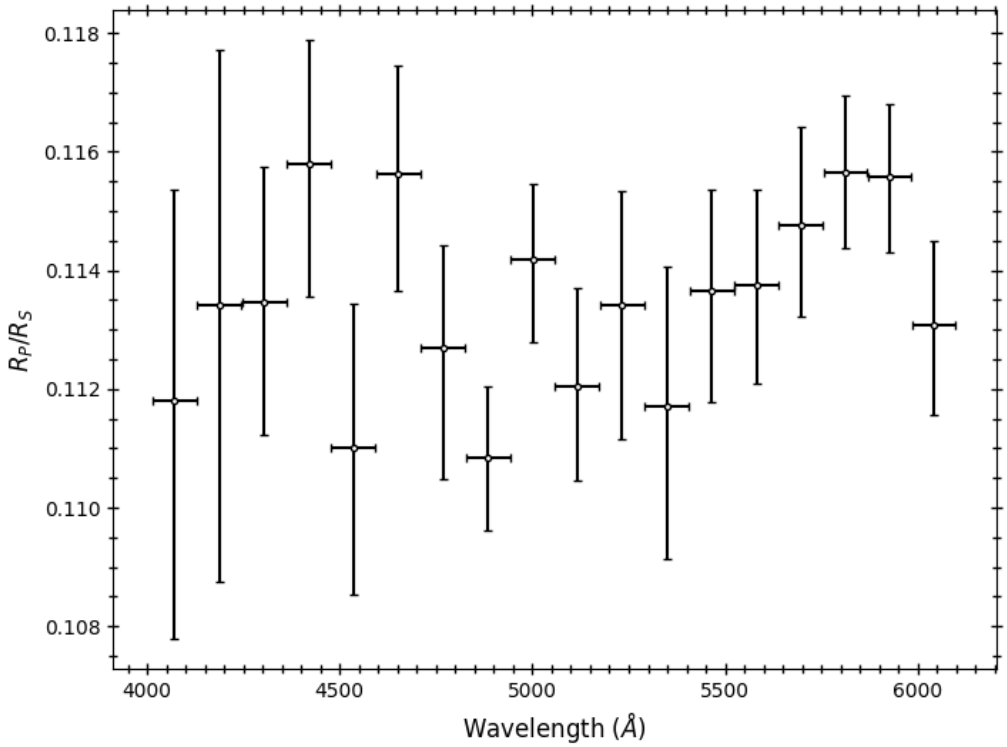


Figure 4.12: The transmission spectrum of WASP-96 b, spanning a wavelength range from approximately 4000 to 6000 Å on x-axis, reveals no clear detection of sodium (Na) absorption features through variations in the planetary radius relative to the stellar radius ($R_P/R_S$) on y-axis. Note the difference in scale with respect to Figure 4.13.

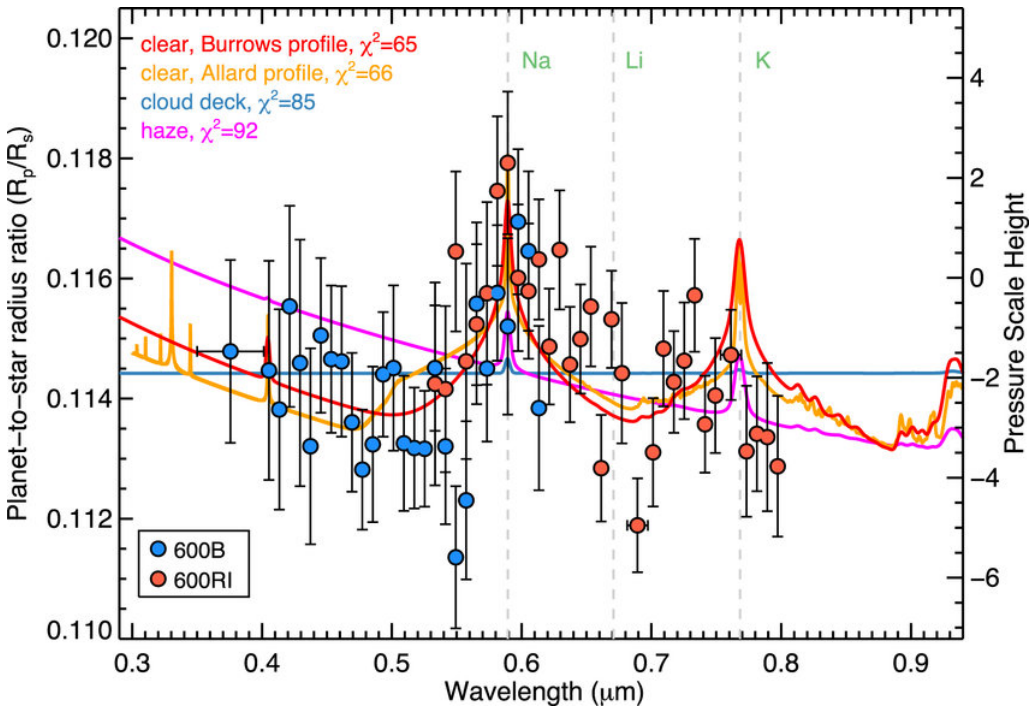


Figure 4.13: Transmission spectrum of WASP-96 b from Nikolov et al. (2018). The black dots with $1\sigma$ error bars represent FORS2 observations, while the horizontal bars indicate spectral bin widths. Colored lines show various atmospheric models: clear (red and orange), cloudy (blue), and hazy (magenta). The spectrum reveals prominent Na absorption features consistent with a clear, cloud-free atmosphere.

in Nikolov et al. (2018). This strong agreement with known results highlights the reliability and effectiveness of the GP approach for analyzing transit observations.

The GP parameters are consistent with Nikolov et al. (2018) with lower precision. The presence of sodium (Na) absorption feature in the transmission spectrum of WASP-96 b remains plausible based on the feature seen around 5900 Å in Figure 4.12 compared to that seen in Figure 4.13

Several factors may contribute to this discrepancy. First, differences in data reduction methodology could play a significant role; I used `EsoReflex` for initial data reduction, followed by custom code for further analysis, whereas Nikolov et al. (2018) in their study, used a custom IDL script for the data reduction. These differing approaches might have led to variations in the final spectrum. Additionally, the error bars in the transmission spectrum are approximately twice as large as those reported by Nikolov et al. (2018), potentially masking weaker spectral features. Variations in spectral extraction, normalization, or detrending methods might also have contributed to the differences in the final results. Since, I decied to not use grism `600RI` data, I could only use the first night data with grism `600B`, covering wavelength range only until 3600 Å to 6100 Å. Due to the limited data access, I could only check for partially hidden Na features. Instead, the analysis of Nikolov et al. (2018) ranges from 3600 to 8200 Å.

Table 4.2: The parameter values of WASP-96 b were obtained from fitting the white-light curve, incorporating both polynomial and GP detrending methods.

| Grism | Parameter | Fitted values |
|---|---|---|
| 600 B | Scaled semi-major axis $a/R_S$ | $8.503^{+0.084}_{-0.093}$ |
| | Inclination $i$ (°) | $84.785^{+0.095}_{-0.107}$ |
| | Planet-to-star radius ratio $R_P/R_S$ | $0.114057^{+0.000089}_{-0.000094}$ |
| | Limb-darkening coefficient $u_1$ | $0.480^{+0.068}_{-0.070}$ |
| | Limb-darkening coefficient $u_2$ | 0.0660 (fixed) |

Extensive atmospheric studies using space-based and ground-based telescopes have made the hot Saturn exoplanet WASP-96 b one of the most studied and well-understood exoplanets. Prominent sodium (Na) absorption features in the VLT observations by Nikolov et al. (2018) suggested that the atmosphere was cloud-free. Later observations by the Spitzer Space Telescope and the Hubble Space Telescope (HST) confirmed this finding (Nikolov et al., 2022). However, more recent studies have provided a more complex understanding of WASP-96 b's atmosphere. The James Webb Space Telescope (JWST), as part of its Early Release Observations program, utilized the NIRISS/SOSS instrument to conduct detailed atmospheric analysis (Taylor et al., 2023; Radica et al., 2023), detecting water vapor $H_2O$, car-

Table 4.3: Retrieved transmission spectrum of WASP-96 b in tabulated form using GP detrending as plotted in Figure 4.11.

| Bin (Å) | $R_P/R_S$ | $u_1$ | $u_2$ (fixed) |
|---|---|---|---|
| 4013-4127 | $0.1118^{+0.0036}_{-0.0040}$ | $0.9375^{+0.0005}_{-0.0005}$ | -0.0903 |
| 4129-4244 | $0.1134^{+0.0043}_{-0.0047}$ | $0.9193^{+0.0004}_{-0.0004}$ | -0.0657 |
| 4245-4360 | $0.1135^{+0.0023}_{-0.0022}$ | $0.8646^{+0.0003}_{-0.0003}$ | -0.0426 |
| 4361-4476 | $0.1158^{+0.0021}_{-0.0022}$ | $0.8695^{+0.0003}_{-0.0003}$ | -0.0210 |
| 4477-4592 | $0.1110^{+0.0024}_{-0.0025}$ | $0.8018^{+0.0006}_{-0.0006}$ | -0.0009 |
| 4593-4708 | $0.1156^{+0.0018}_{-0.0020}$ | $0.7794^{+0.0005}_{-0.0005}$ | 0.0177 |
| 4710-4824 | $0.1127^{+0.0017}_{-0.0022}$ | $0.7577^{+0.0006}_{-0.0005}$ | 0.0348 |
| 4826-4941 | $0.1108^{+0.0012}_{-0.0012}$ | $0.2726^{+0.0006}_{-0.0006}$ | 0.0504 |
| 4942-5057 | $0.1142^{+0.0013}_{-0.0014}$ | $0.7160^{+0.0005}_{-0.0005}$ | 0.0645 |
| 5058-5173 | $0.1120^{+0.0017}_{-0.0016}$ | $0.7104^{+0.0005}_{-0.0005}$ | 0.0771 |
| 5174-5289 | $0.1134^{+0.0019}_{-0.0023}$ | $0.3043^{+0.0005}_{-0.0005}$ | 0.0883 |
| 5290-5405 | $0.1117^{+0.0023}_{-0.0026}$ | $0.6454^{+0.0005}_{-0.0005}$ | 0.0979 |
| 5407-5521 | $0.1137^{+0.0017}_{-0.0019}$ | $0.6368^{+0.0005}_{-0.0005}$ | 0.1060 |
| 5523-5638 | $0.1137^{+0.0016}_{-0.0017}$ | $0.6126^{+0.0005}_{-0.0005}$ | 0.1127 |
| 5639-5754 | $0.1148^{+0.0017}_{-0.0015}$ | $0.5975^{+0.0005}_{-0.0005}$ | 0.1178 |
| 5755-5869 | $0.1157^{+0.0013}_{-0.0013}$ | $0.5880^{+0.0005}_{-0.0005}$ | 0.1215 |
| 5870-5983 | $0.1156^{+0.0012}_{-0.0013}$ | $0.5705^{+0.0005}_{-0.0005}$ | 0.1236 |
| 5985-6098 | $0.1131^{+0.0014}_{-0.0015}$ | $0.5626^{+0.0005}_{-0.0005}$ | 0.1243 |

bon dioxide $CO_2$, and potassium K, along with evidence of clouds. A strong water signature was also noted in HST WFC3 observations by Yip et al. (2020).

Further modeling efforts by Samra et al. (2023) using 3D general circulation models (GCMs) and kinetic cloud formation models demonstrated that clouds are probably common in the atmosphere of WASP-96 b, with metal oxides accounting for up to 40% of cloud particles in low-pressure areas and silicates accounting for 40–90%. Mechanisms, like reduced vertical mixing and porous cloud particles, were proposed to explain clear molecular features despite the presence of clouds. The detection of aluminium oxide $Al_2O_3$ in the atmosphere of WASP-96 b by Chubb et al. (2024) provides additional evidence for the existence of metal oxide clouds. Various cloud-forming substances, such as $Al_2O_3$, $Mg_2SiO_4$, FeO, $Fe_2O_3$, and Fe, have a substantial effect on the planet's atmospheric characteristics and observed spectra (Samra et al., 2023).

# Chapter 5

# Conclusion & Future Prospects

In this thesis, I presented a detailed analysis of spectrophotometric FORS2 data of a hot Jupiter HAT-P-30 b and WASP-96 b in transmission, aimed at exploring the atmospheric characteristics of these exoplanets. In both cases, no strong evidence of sodium (Na) or potassium (K) absorption features were detected.

Archival data from two transit events of HAT-P-30 b and WASP-96 b were used to examine the atmospheric composition of these exoplanets. Observations were made using the 600B (blue) and 600RI (red) grisms of the FORS2 spectrograph on 8.2 m Unit Telescope 1 of the VLT, which have a broad wavelength range of 360–820 nm. The `EsoReflex` pipeline was used to reduce the data. However, extracted 1D spectra were not ideal for analysis. I applied a custom Python script to perform Gaussian fitting for spectrum extraction, and barycentric corrections. `Tiberius` was used to apply GP regression to reduce systematic noise, and optimized kernel functions were used to detrend the spectrophotometric light curves and the white-light curve carefully.

In the case of HAT-P-30 b, the transmission spectrum in grism `600B` appears relatively featureless, with no detectable sodium absorption or Rayleigh scattering slope. However, an outlier around 7650 Å in grism `600RI` suggests the possible presence of potassium (K), as seen in Figure 3.18, particularly when compared to the model transmission spectrum derived using PetitRADTRANS (Mollière et al., 2019) in Figure 3.19; this potential potassium detection warrants further investigation. HAT-P-30 b is a highly misaligned exoplanet orbits an F-type dwarf star ($V_{\mathrm{mag}}$ = 10.4) on a 2.81-day orbit with an equilibrium temperature of 1630 K. The transmission spectrum was extracted into 23 bins, each being 170 to 280 Å wide for the first and second nights, respectively. The featureless outcome of the transmission spectrum of HAT-P-30 b may be attributed to the presence of high-altitude clouds or hazes that obscure the expected spectral lines; this phenomenon is commonly observed in many hot Jupiters (Sing et al., 2016). Additionally, the low signal-to-noise ratio (SNR) of the reference star with extremely low brightness (($G_{\mathrm{mag}}$ = 13.57) likely introduced additional uncertainties, potentially limiting our ability to detect faint atmospheric signatures. During observations, the reference star was also po-

sitioned near a faulty pixel row on the detector, which likely resulted in the loss of crucial spectral information and further reduced the SNR.

The study of WASP-96 b in this thesis, a "hot Jupiter" exoplanet orbiting a G8-type star, was conducted as a reference for the analysis of HAT-P-30 b. Light curves were created for both the target and a reference star, with the second night's data being excluded due to distortion. The spectra were divided into 18 wavelength bins with a bin width of 144 Å for detailed analysis. GP regression was applied using `Tiberius` software to detrend the light curves and reduce red noise. The GP parameters were found to be consistent with those reported by (Nikolov et al., 2018), albeit with lower precision. The retrieved transmission spectrum spans wavelengths from about 4000 to 6000 Å, and the presence of a sodium (Na) absorption feature remains plausible based on the feature seen around 5900 Å in Figure 4.12, which aligns with the previously observed feature in Figure 4.13. This finding suggests that, while the signal is less pronounced, it does not contradict earlier detections by (Nikolov et al., 2018). Since this study used `EsoReflex` for initial processing and custom Python scripts for analysis, while earlier work used a custom IDL script, the difference may be the result of different data reduction approaches. A common noise model, used in previous studies (e.g. Sing et al., 2012; Nikolov et al., 2016; Kirk et al., 2021), could have reduced uncertainties and systematic noise, but time and computational constraints prevented its application. Future studies could explore this approach to reassess Na and K detections and improve the precision of atmospheric characterizations. The methodology validated with WASP-96 b was successfully applied to HAT-P-30 b; the pre-Tiberius processing may have influenced the results, further validation is needed.

## 5.1 Future prospects

To detect the expected presence of Na, K, or other molecular species in the atmosphere of HAT-P-30 b, future observations with higher resolution and improved reference star selection are encouraged. Space-based observatories such as JWST, and Ariel could provide more precise measurements, minimizing the impact of telluric contamination and instrumental noise. Additionally, upcoming ELT could provide high-quality ground-based observations.

Over 15 cases confirmed by HST and only a small number measured from the ground - sodium absorption detections in hot Jupiters are still somewhat rare, particularly in the low-resolution regime (e.g., Nikolov et al., 2014; Kang et al., 2024; Sing et al., 2012; Chen et al., 2020; Nikolov et al., 2016, 2018). In some instances, the detections have been challenged, such as in the initial HD 209458b case (Casasayas-Barris et al., 2020, 2021). A comparative study targeting other gas giants with similar temperatures and radii would be valuable in determining whether the observed lack of Na and K absorption is unique to HAT-P-30 b or a common trait among hot Jupiters. Such an investigation could shed light on the role of atmo-

spheric dynamics, cloud formation, and elemental depletion processes in shaping the exoplanetary atmosphere.

A non-detection of Na and K in similar exoplanets would suggest that HAT-P-30 b is not unique but rather part of a broader atmospheric trend among hot Jupiters. Conversely, suppose other exoplanets of similar characteristics exhibit strong Na and K signatures. In that case, HAT-P-30 b might represent a unique case where additional physical mechanisms, such as photochemical hazes or strong metallic cloud coverage, could be influencing the atmosphere (e.g. Sing et al., 2016).

# Bibliography


Ahrer, E.-M. (2023). *Low resolution transmission spectroscopy of exoplanet atmospheres using ground-based and space telescopes*. PhD thesis, University of Warwick.

Aigrain, S., Parviainen, H., and Pope, B. (2016). K2sc: flexible systematics correction and detrending of k2 light curves using gaussian process regression. *Monthly Notices of the Royal Astronomical Society*, 459(3):2408–2419.

Anglada-Escudé, G., Amado, P. J., Barnes, J., Berdiñas, Z. M., Butler, R. P., Coleman, G. A., de La Cueva, I., Dreizler, S., Endl, M., Giesers, B., et al. (2016). A terrestrial planet candidate in a temperate orbit around proxima centauri. *Nature*, 536(7617):437–440.

Appenzeller, I., Fricke, K., Fürtig, W., Gässler, W., Häfner, R., Harke, R., Hess, H., Hummel, W., Jürgens, P., Kudritzki, R., et al. (1998). Successful commissioning of fors1-the first optical instrument on the vlt. *The messenger*, 94(1).

Astudillo-Defru, N. and Rojo, P. (2013). Ground-based detection of calcium and possibly scandium and hydrogen in the atmosphere of hd 209458b. *Astronomy & Astrophysics*, 557:A56.

Baeyens, R., Konings, T., Venot, O., Carone, L., and Decin, L. (2022). Grid of pseudo-2d chemistry models for tidally locked exoplanets–ii. the role of photochemistry. *Monthly Notices of the Royal Astronomical Society*, 512(4):4877–4892.

Bakos, G., Noyes, R., Kovács, G., Stanek, K., Sasselov, D. D., and Domsa, I. (2004). Wide-field millimagnitude photometry with the hat: A tool for extrasolar planet detection. *Publications of the Astronomical Society of the Pacific*, 116(817):266.

Barragán, O., Aigrain, S., Kubyshkina, D., Gandolfi, D., Livingston, J., Fridlund, M., Fossati, L., Korth, J., Parviainen, H., Malavolta, L., et al. (2019). Radial velocity confirmation of k2-100b: a young, highly irradiated, and low-density transiting hot neptune. *Monthly Notices of the Royal Astronomical Society*, 490(1):698–708.

Baxter, C., Désert, J.-M., Parmentier, V., Line, M., Fortney, J., Arcangeli, J., Bean, J. L., Todorov, K. O., and Mansfield, M. (2020). A transition between the hot and the ultra-hot jupiter atmospheres. *Astronomy & Astrophysics*, 639:A36.

Beaulieu, J.-P., Bennett, D. P., Fouqué, P., Williams, A., Dominik, M., Jørgensen, U., Kubas, D., Cassan, A., Coutures, C., Greenhill, J., et al. (2006). Discovery of a cool planet of 5.5 earth masses through gravitational microlensing. *Nature*, 439(7075):437–440.

Benedict, G., McArthur, B., Nelan, E., Wittenmyer, R., Barnes, R., Smotherman, H., and Horner, J. (2022). The $\mu$ arae planetary system: Radial velocities and astrometry. *The Astronomical Journal*, 163(6):295.

Benedict, G. F., McArthur, B. E., Gatewood, G., Nelan, E., Cochran, W. D., Hatzes, A., Endl, M., Wittenmyer, R., Baliunas, S. L., Walker, G. A., et al. (2006). The extrasolar planet $\epsilon$ eridani b: orbit and mass. *The Astronomical Journal*, 132(5):2206.

Birkby, J., De Kok, R., Brogi, M., de Mooij, E., Schwarz, H., Albrecht, S., and Snellen, I. (2013). Detection of water absorption in the day side atmosphere of hd 189733 b using ground-based high-resolution spectroscopy at 3.2 $\mu$m. *Monthly Notices of the Royal Astronomical Society: Letters*, 436(1):L35–L39.

Boffin, H., Blanchard, G., Gonzalez, O., Moehler, S., Sedaghati, E., Gibson, N., van den Ancker, M., Smoker, J., Anderson, J., Hummel, C., et al. (2015). Making fors2 fit for exoplanet observations (again). *arXiv preprint arXiv:1502.03172*.

Bohn, A. J., Kenworthy, M. A., Ginski, C., Rieder, S., Mamajek, E. E., Meshkat, T., Pecaut, M. J., Reggiani, M., de Boer, J., Keller, C. U., et al. (2020). Two directly imaged, wide-orbit giant planets around the young, solar analog tyc 8998-760-1. *The Astrophysical Journal Letters*, 898(1):L16.

Boisse, I., Pepe, F., Perrier, C., Queloz, D., Bonfils, X., Bouchy, F., Santos, N., Arnold, L., Beuzit, J.-L., Díaz, R., et al. (2012). The sophie search for northern extrasolar planets-v. follow-up of elodie candidates: Jupiter-analogs around sun-like stars. *Astronomy & Astrophysics*, 545:A55.

Bond, I. A., Udalski, A., Jaroszyński, M., Rattenbury, N., Paczyński, B., Soszyński, I., Wyrzykowski, L., Szymański, M., Kubiak, M., Szewczyk, O., et al. (2004). Ogle 2003-blg-235/moa 2003-blg-53: a planetary microlensing event. *The Astrophysical Journal*, 606(2):L155.

Borucki, W. J., Koch, D., Basri, G., Batalha, N., Brown, T., Caldwell, D., Caldwell, J., Christensen-Dalsgaard, J., Cochran, W. D., DeVore, E., et al. (2010). Kepler planet-detection mission: introduction and first results. *Science*, 327(5968):977–980.

Boss, A. P. (1997). Giant planet formation by gravitational instability. *Science*, 276(5320):1836–1839.

Brown, T. M. (2001). Transmission spectra as diagnostics of extrasolar giant planet atmospheres. *The Astrophysical Journal*, 553(2):1006.

Casasayas-Barris, N., Palle, E., Nowak, G., Yan, F., Nortmann, L., and Murgas, F. (2017). Detection of sodium in the atmosphere of wasp-69b. *Astronomy & Astrophysics*, 608:A135.

Casasayas-Barris, N., Palle, E., Stangret, M., Bourrier, V., Tabernero, H., Yan, F., Borsa, F., Allart, R., Osorio, M. Z., Lovis, C., et al. (2021). The atmosphere of hd 209458b seen with espresso-no detectable planetary absorptions at high resolution. *Astronomy & Astrophysics*, 647:A26.

Casasayas-Barris, N., Pallé, E., Yan, F., Chen, G., Luque, R., Stangret, M., Nagel, E., Zechmeister, M., Oshagh, M., Sanz-Forcada, J., et al. (2020). Is there na i in the atmosphere of hd 209458b?-effect of the centre-to-limb variation and rossiter-mclaughlin effect in transmission spectroscopy studies. *Astronomy & Astrophysics*, 635:A206.

Cegla, H., Roguet-Kern, N., Lendl, M., Akinsanmi, B., McCormac, J., Oshagh, M., Wheatley, P., Chen, G., Allart, R., Mortier, A., et al. (2023). Exploring the stellar surface phenomena of wasp-52 and hat-p-30 with espresso. *Astronomy & Astrophysics*, 674:A174.

Charbonneau, D., Brown, T. M., Latham, D. W., and Mayor, M. (1999). Detection of planetary transits across a sun-like star. *The Astrophysical Journal*, 529(1):L45.

Charbonneau, D., Brown, T. M., Noyes, R. W., and Gilliland, R. L. (2002). Detection of an extrasolar planet atmosphere. *The Astrophysical Journal*, 568(1):377.

Chauvin, G., Lagrange, A.-M., Dumas, C., Zuckerman, B., Mouillet, D., Song, I., Beuzit, J.-L., and Lowrance, P. (2004). A giant planet candidate near a young brown dwarf-direct vlt/naco observations using ir wavefront sensing. *Astronomy & Astrophysics*, 425(2):L29–L32.

Chen, G., Casasayas-Barris, N., Pallé, E., Welbanks, L., Madhusudhan, N., Luque, R., and Murgas, F. (2020). Detection of na in wasp-21b's lower and upper atmosphere. *Astronomy & Astrophysics*, 642:A54.

Chubb, K. L., Stam, D. M., Helling, C., Samra, D., and Carone, L. (2024). Modelling reflected polarized light from close-in giant exoplanet wasp-96b using polhex (polarization of hot exoplanets). *Monthly Notices of the Royal Astronomical Society*, 527(3):4955–4982.

Claudi, R., Benatti, S., Carleo, I., Ghedina, A., Molinari, E., Oliva, E., Tozzi, A., Baruffolo, A., Cecconi, M., Cosentino, R., et al. (2016). Giarps: the unique vis-nir high precision radial velocity facility in this world. In *Ground-based and airborne instrumentation for astronomy vi*, volume 9908, pages 359–366. SPIE.

Clavel, J. (2009). Esa's cosmic vision 2015-2025 program. In *Astronomical Data Analysis Software and Systems XVIII*, volume 411, page 89.

Connelly, J. N., Bizzarro, M., Krot, A. N., Nordlund, Å., Wielandt, D., and Ivanova, M. A. (2012). The absolute chronology and thermal processing of solids in the solar protoplanetary disk. *Science*, 338(6107):651–655.

Cridland, A. J., van Dishoeck, E. F., Alessi, M., and Pudritz, R. E. (2019). Connecting planet formation and astrochemistry-a main sequence for c/o in hot exoplanetary atmospheres. *Astronomy & Astrophysics*, 632:A63.

Csizmadia, S., Pasternacki, T., Dreyer, C., Cabrera, J., Erikson, A., and Rauer, H. (2013). The effect of stellar limb darkening values on the accuracy of the planet radii derived from photometric transit observations. *Astronomy & Astrophysics*, 549:A9.

Dawson, R. I. and Johnson, J. A. (2018). Origins of hot jupiters. *Annual Review of Astronomy and Astrophysics*, 56(1):175–221.

De Wit, J. and Seager, S. (2013). Constraining exoplanet mass from transmission spectroscopy. *Science*, 342(6165):1473–1477.

Deming, D., Wilkins, A., McCullough, P., Burrows, A., Fortney, J. J., Agol, E., Dobbs-Dixon, I., Madhusudhan, N., Crouzet, N., Desert, J.-M., et al. (2013). Infrared transmission spectroscopy of the exoplanets hd 209458b and xo-1b using the wide field camera-3 on the hubble space telescope. *The Astrophysical Journal*, 774(2):95.

Demory, B.-O., De Wit, J., Lewis, N., Fortney, J., Zsom, A., Seager, S., Knutson, H., Heng, K., Madhusudhan, N., Gillon, M., et al. (2013). Inference of inhomogeneous clouds in an exoplanet atmosphere. *The Astrophysical Journal Letters*, 776(2):L25.

Des Etangs, A. L. and Lissauer, J. J. (2022). The iau working definition of an exoplanet. *New Astronomy Reviews*, 94:101641.

Drummond, B., Hébrard, E., Mayne, N. J., Venot, O., Ridgway, R. J., Changeat, Q., Tsai, S.-M., Manners, J., Tremblin, P., Abraham, N. L., et al. (2020). Implications of three-dimensional chemical transport in hot jupiter atmospheres: Results from a consistently coupled chemistry-radiation-hydrodynamics model. *Astronomy & Astrophysics*, 636:A68.

Dumusque, X., Santos, N., Udry, S., Lovis, C., and Bonfils, X. (2011). Planetary detection limits taking into account stellar noise-ii. effect of stellar spot groups on radial-velocities. *Astronomy & Astrophysics*, 527:A82.

D'Angelo, G., Lubow, S. H., and Bate, M. R. (2006). Evolution of giant planets in eccentric disks. *The Astrophysical Journal*, 652(2):1698.

Einstein, A. (1936). Lens-like action of a star by the deviation of light in the gravitational field. *Science*, 84(2188):506–507.

Ekers, R. (2018). The prague iau general assembly, pluto and the iau processes. *Proceedings of the International Astronomical Union*, 13(S349):51–57.

Espinoza, N. and Jordán, A. (2015). Limb darkening and exoplanets: testing stellar model atmospheres and identifying biases in transit parameters. *Monthly Notices of the Royal Astronomical Society*, 450(2):1879–1899.

Evans, T. M., Aigrain, S., Gibson, N., Barstow, J. K., Amundsen, D. S., Tremblin, P., and Mourier, P. (2015). A uniform analysis of hd 209458b spitzer/irac light curves with gaussian process models. *Monthly Notices of the Royal Astronomical Society*, 451(1):680–694.

Evans, T. M., Pont, F., Sing, D. K., Aigrain, S., Barstow, J. K., Désert, J.-M., Gibson, N., Heng, K., Knutson, H. A., and Des Etangs, A. L. (2013). The deep blue color of hd 189733b: Albedo measurements with hubble space telescope/space telescope imaging spectrograph at visible wavelengths. *The Astrophysical Journal Letters*, 772(2):L16.

Feinstein, A. D., Radica, M., Welbanks, L., Murray, C. A., Ohno, K., Coulombe, L.-P., Espinoza, N., Bean, J. L., Teske, J. K., Benneke, B., et al. (2023). Early release science of the exoplanet wasp-39b with jwst niriss. *Nature*, 614(7949):670–675.

Flower, P. J. (1996). Transformations from theoretical hertzsprung-russell diagrams to color-magnitude diagrams: effective temperatures, bv colors, and bolometric corrections. *Astrophysical Journal v. 469, p. 355*, 469:355.

Foreman-Mackey, D., Hogg, D. W., Lang, D., and Goodman, J. (2013). emcee: the mcmc hammer. *Publications of the Astronomical Society of the Pacific*, 125(925):306.

Fortney, J. J. (2024). Characterizing exoplanetary atmospheres: New views on exoplanet composition and chemistry. *arXiv preprint arXiv:2405.04587*.

Fortney, J. J., Mordasini, C., Nettelmann, N., Kempton, E. M.-R., Greene, T. P., and Zahnle, K. (2013). A framework for characterizing the atmospheres of low-mass low-density transiting planets. *The Astrophysical Journal*, 775(1):80.

Fortney, J. J., Visscher, C., Marley, M. S., Hood, C. E., Line, M. R., Thorngren, D. P., Freedman, R. S., and Lupu, R. (2020). Beyond equilibrium temperature: how the atmosphere/interior connection affects the onset of methane, ammonia, and clouds in warm transiting giant planets. *The Astronomical Journal*, 160(6):288.

Freudling, W., Romaniello, M., Bramich, D., Ballester, P., Forchi, V., García-Dabló, C., Moehler, S., and Neeser, M. (2013). Automated data reduction workflows for astronomy-the eso reflex environment. *Astronomy & Astrophysics*, 559:A96.

Gammie, C. F. (2001). Nonlinear outcome of gravitational instability in cooling, gaseous disks. *The Astrophysical Journal*, 553(1):174.

Gardner, J. P., Mather, J. C., Clampin, M., Doyon, R., Greenhouse, M. A., Hammel, H. B., Hutchings, J. B., Jakobsen, P., Lilly, S. J., Long, K. S., et al. (2006). The james webb space telescope. *Space Science Reviews*, 123:485–606.

Gibson, N., Aigrain, S., Roberts, S., Evans, T., Osborne, M., and Pont, F. (2012). A gaussian process framework for modelling instrumental systematics: application to transmission spectroscopy. *Monthly notices of the royal astronomical society*, 419(3):2683–2694.

Greene, T. P., Bell, T. J., Ducrot, E., Dyrek, A., Lagage, P.-O., and Fortney, J. J. (2023). Thermal emission from the earth-sized exoplanet trappist-1 b using jwst. *Nature*, 618(7963):39–42.

Görtler, J., Kehlbeck, R., and Deussen, O. (2019). A visual exploration of gaussian processes. *Distill*. https://distill.pub/2019/visual-exploration-gaussian-processes.

Hawker, G. A., Madhusudhan, N., Cabot, S. H., and Gandhi, S. (2018). Evidence for multiple molecular species in the hot jupiter hd 209458b. *The Astrophysical Journal Letters*, 863(1):L11.

Haywood, R., Collier Cameron, A., Queloz, D., Barros, S., Deleuil, M., Fares, R., Gillon, M., Lanza, A., Lovis, C., Moutou, C., et al. (2014). Planets and stellar activity: hide and seek in the corot-7 system. *Monthly notices of the royal astronomical society*, 443(3):2517–2531.

Heller, R. (2019). Analytic solutions to the maximum and average exoplanet transit depth for common stellar limb darkening laws. *Astronomy & Astrophysics*, 623:A137.

Hellier, C., Anderson, D., Cameron, A. C., Delrez, L., Gillon, M., Jehin, E., Lendl, M., Maxted, P., Pepe, F., Pollacco, D., et al. (2014). Transiting hot jupiters from wasp-south, euler and trappist: Wasp-95b to wasp-101b. *Monthly Notices of the Royal Astronomical Society*, 440(3):1982–1992.

Helling, C. (2019). Exoplanet clouds. *Annual Review of Earth and Planetary Sciences*, 47(1):583–606.

Henry, G. W., Marcy, G. W., Butler, R. P., and Vogt, S. S. (1999). A transiting "51 peg-like" planet. *The Astrophysical Journal*, 529(1):L41.

Hoeijmakers, H. J., Ehrenreich, D., Heng, K., Kitzmann, D., Grimm, S. L., Allart, R., Deitrick, R., Wyttenbach, A., Oreshenko, M., Pino, L., et al. (2018). Atomic iron and titanium in the atmosphere of the exoplanet kelt-9b. *Nature*, 560(7719):453–455.

Hoeijmakers, H. J., Ehrenreich, D., Kitzmann, D., Allart, R., Grimm, S. L., Seidel, J., Wyttenbach, A., Pino, L., Nielsen, L., Fisher, C., et al. (2019). A spectral survey of an ultra-hot jupiter-detection of metals in the transmission spectrum of kelt-9 b. *Astronomy & Astrophysics*, 627:A165.

Hubeny, I., Burrows, A., and Sudarsky, D. (2003). A possible bifurcation in atmospheres of strongly irradiated stars and planets. *The Astrophysical Journal*, 594(2):1011.

Huitson, C. M., Sing, D. K., Vidal-Madjar, A., Ballester, G. E., Lecavelier des Etangs, A., Désert, J.-M., and Pont, F. (2012). Temperature–pressure profile of the hot jupiter hd 189733b from hst sodium observations: detection of upper atmospheric heating. *Monthly Notices of the Royal Astronomical Society*, 422(3):2477–2488.

Husser, T.-O., Wende-von Berg, S., Dreizler, S., Homeier, D., Reiners, A., Barman, T., and Hauschildt, P. H. (2013). A new extensive library of phoenix stellar atmospheres and synthetic spectra. *Astronomy & Astrophysics*, 553:A6.

Ikoma, M., Nakazawa, K., and Emori, H. (2000). Formation of giant planets: dependences on core accretion rate and grain opacity. *The Astrophysical Journal*, 537(2):1013.

Inaba, S., Wetherill, G. W., and Ikoma, M. (2003). Formation of gas giant planets: core accretion models with fragmentation and planetary envelope. *Icarus*, 166(1):46–62.

Johnson, J. A., Winn, J., Bakos, G., Hartman, J., Morton, T., Torres, G., Kovács, G., Latham, D., Noyes, R., Sato, B., et al. (2011). Hat-p-30b: a transiting hot jupiter on a highly oblique orbit. *The Astrophysical Journal*, 735(1):24.

Kang, H., Chen, G., Jiang, C., Palle, E., Murgas, F., Parviainen, H., Ma, Y., Fukui, A., and Narita, N. (2024). Detection of na in the atmosphere of the hot jupiter hat-p-55b. *arXiv preprint arXiv:2404.13849*.

Keles, E., Mallonn, M., von Essen, C., Carroll, T. A., Alexoudi, X., Pino, L., Ilyin, I., Poppenhäger, K., Kitzmann, D., Nascimbeni, V., et al. (2019). The potassium absorption on hd189733b and hd209458b. *Monthly Notices of the Royal Astronomical Society: Letters*, 489(1):L37–L41.

Kempton, E. M.-R. and Knutson, H. A. (2024). Transiting exoplanet atmospheres in the era of jwst. *Reviews in Mineralogy and Geochemistry*, 90(1):411–464.

Kempton, E. M.-R., Zhang, M., Bean, J. L., Steinrueck, M. E., Piette, A. A., Parmentier, V., Malsky, I., Roman, M. T., Rauscher, E., Gao, P., et al. (2023). A reflective, metal-rich atmosphere for gj 1214b from its jwst phase curve. *Nature*, 620(7972):67–71.

Kipping, D. M. (2013). Efficient, uninformative sampling of limb darkening coefficients for two-parameter laws. *Monthly Notices of the Royal Astronomical Society*, 435(3):2152–2160.

Kirk, J. (2018). *Optical transmission spectroscopy of hot Jupiter atmospheres*. PhD thesis, University of Warwick.

Kirk, J., Ahrer, E.-M., Penzlin, A. B., Owen, J. E., Booth, R. A., Alderson, L., Christie, D. A., Claringbold, A. B., Esparza-Borges, E., Fisher, C. E., et al. (2024). Bowie-align: A jwst comparative survey of aligned versus misaligned hot jupiters to test the dependence of atmospheric composition on migration history. *RAS Techniques and Instruments*, 3(1):691–704.

Kirk, J., Rackham, B. V., MacDonald, R. J., López-Morales, M., Espinoza, N., Lendl, M., Wilson, J., Osip, D. J., Wheatley, P. J., Skillen, I., et al. (2021). Access and lrg-beasts: a precise new optical transmission spectrum of the ultrahot jupiter wasp-103b. *The Astronomical Journal*, 162(1):34.

Kirk, J., Wheatley, P. J., Louden, T., Doyle, A., Skillen, I., McCormac, J., Irwin, P., and Karjalainen, R. (2017). Rayleigh scattering in the transmission spectrum of hat-p-18b. *Monthly Notices of the Royal Astronomical Society*, 468(4):3907–3916.

Kirk, J., Wheatley, P. J., Louden, T., Littlefair, S., Copperwheat, C., Armstrong, D. J., Marsh, T., and Dhillon, V. (2016). Transmission spectroscopy of the inflated exoplanet wasp-52b, and evidence for a bright region on the stellar surface. *Monthly Notices of the Royal Astronomical Society*, 463(3):2922–2931.

Kreidberg, L. (2017). Exoplanet atmosphere measurements from transmission spectroscopy and other planet-star combined light observations. *arXiv preprint arXiv:1709.05941*.

Kuzuhara, M., Tamura, M., Kudo, T., Janson, M., Kandori, R., Brandt, T., Thalmann, C., Spiegel, D., Biller, B., Carson, J., et al. (2013). Direct imaging of a cold jovian exoplanet in orbit around the sun-like star gj 504. *The Astrophysical Journal*, 774(1):11.

Lagrange, A.-M., Gratadour, D., Chauvin, G., Fusco, T., Ehrenreich, D., Mouillet, D., Rousset, G., Rouan, D., Allard, F., Gendron, É., et al. (2009). A probable giant planet imaged in the $\beta$ pictoris disk-vlt/naco deep l'-band imaging. *Astronomy & Astrophysics*, 493(2):L21–L25.

Lee, E. J. and Chiang, E. (2016). Breeding super-earths and birthing super-puffs in transitional disks. *The Astrophysical Journal*, 817(2):90.

Léger, A., Pirre, M., and Marceau, F. (1994). How to evidence life on a distant planet. *Astrophysics and Space Science*, 212:327–333.

Lin, D. N., Bodenheimer, P., and Richardson, D. C. (1996). Orbital migration of the planetary companion of 51 pegasi to its present location. *Nature*, 380(6575):606–607.

Llop-Sayson, J., Wang, J. J., Ruffio, J.-B., Mawet, D., Blunt, S., Absil, O., Bond, C., Brinkman, C., Bowler, B. P., Bottom, M., et al. (2021). Constraining the orbit and mass of epsilon eridani b with radial velocities, hipparcos iad-gaia dr2 astrometry, and multiepoch vortex coronagraphy upper limits. *The Astronomical Journal*, 162(5):181.

Lustig-Yaeger, J., Meadows, V. S., Crisp, D., Line, M. R., and Robinson, T. D. (2023). Earth as a transiting exoplanet: A validation of transmission spectroscopy and atmospheric retrieval methodologies for terrestrial exoplanets. *The Planetary Science Journal*, 4(9):170.

Madhusudhan, N. (2012). C/o ratio as a dimension for characterizing exoplanetary atmospheres. *The Astrophysical Journal*, 758(1):36.

Madhusudhan, N. (2019). Exoplanetary atmospheres: Key insights, challenges, and prospects. *Annual Review of Astronomy and Astrophysics*, 57:617–663.

Madhusudhan, N., Knutson, H., Fortney, J., and Barman, T. (2014). Exoplanetary atmospheres. *arXiv preprint arXiv:1402.1169*.

Mallonn, M., Bernt, I., Herrero, E., Hoyer, S., Kirk, J., Wheatley, P. J., Seeliger, M., Mackebrandt, F., von Essen, C., Strassmeier, K., et al. (2016). Broad-band spectrophotometry of hat-p-32 b: search for a scattering signature in the planetary spectrum. *Monthly Notices of the Royal Astronomical Society*, 463(1):604–614.

Mamajek, E. E. (2009). Initial conditions of planet formation: lifetimes of primordial disks. In *AIP Conference Proceedings*, volume 1158, pages 3–10. American Institute of Physics.

Mao, S. and Paczynski, B. (1991). Gravitational microlensing by double stars and planetary systems. *Astrophysical Journal, Part 2-Letters (ISSN 0004-637X), vol. 374, June 20, 1991, p. L37-L40.*, 374:L37–L40.

Martins, J., Santos, N., Figueira, P., Faria, J., Montalto, M., Boisse, I., Ehrenreich, D., Lovis, C., Mayor, M., Melo, C., et al. (2015). Evidence for a spectroscopic direct detection of reflected light from 51 pegasi b. *Astronomy & Astrophysics*, 576:A134.

Mayor, M., Lovis, C., and Santos, N. C. (2014). Doppler spectroscopy as a path to the detection of earth-like planets. *Nature*, 513(7518):328–335.

Mayor, M. and Queloz, D. (1995). A jupiter-mass companion to a solar-type star. *nature*, 378(6555):355–359.

McArthur, B. E., Endl, M., Cochran, W. D., Benedict, G. F., Fischer, D. A., Marcy, G. W., Butler, R. P., Naef, D., Mayor, M., Queloz, D., et al. (2004). Detection of a neptune-mass planet in the $\rho$1 cancri system using the hobby-eberly telescope. *The Astrophysical Journal*, 614(1):L81.

Mollière, P., Wardenier, J., Van Boekel, R., Henning, T., Molaverdikhani, K., and Snellen, I. (2019). petitradtrans-a python radiative transfer package for exoplanet characterization and retrieval. *Astronomy & Astrophysics*, 627:A67.

Montmerle, T., Augereau, J.-C., Chaussidon, M., Gounelle, M., Marty, B., and Morbidelli, A. (2006). 3. solar system formation and early evolution: the first 100 million years. *Earth, Moon, and Planets*, 98:39–95.

Moses, J. I., Visscher, C., Fortney, J. J., Showman, A. P., Lewis, N. K., Griffith, C. A., Klippenstein, S. J., Shabram, M., Friedson, A. J., Marley, M. S., et al. (2011). Disequilibrium carbon, oxygen, and nitrogen chemistry in the atmospheres of hd 189733b and hd 209458b. *The Astrophysical Journal*, 737(1):15.

Muñoz, A. G. and Isaak, K. G. (2015). Probing exoplanet clouds with optical phase curves. *Proceedings of the National Academy of Sciences*, 112(44):13461–13466.

Nelson, B. E., Ford, E. B., and Rasio, F. A. (2017). Evidence for two hot-jupiter formation paths. *The Astronomical Journal*, 154(3):106.

Neveu-VanMalle, M., Queloz, D., Anderson, D., Charbonnel, C., Cameron, A. C., Delrez, L., Gillon, M., Hellier, C., Jehin, E., Lendl, M., et al. (2014). Wasp-94 a and b planets: hot-jupiter cousins in a twin-star system. *Astronomy & Astrophysics*, 572:A49.

Nikolov, N., Sing, D. K., Fortney, J. J., Goyal, J. M., Drummond, B., Evans, T. M., Gibson, N. P., De Mooij, E. J., Rustamkulov, Z., Wakeford, H. R., et al. (2018). An absolute sodium abundance for a cloud-free 'hot saturn'exoplanet. *Nature*, 557(7706):526–529.

Nikolov, N., Sing, D. K., Gibson, N. P., Fortney, J. J., Evans, T. M., Barstow, J. K., Kataria, T., and Wilson, P. A. (2016). Vlt fors2 comparative transmission spectroscopy: detection of na in the atmosphere of wasp-39b from the ground. *The Astrophysical Journal*, 832(2):191.

Nikolov, N., Sing, D. K., Pont, F., Burrows, A. S., Fortney, J. J., Ballester, G. E., Evans, T. M., Huitson, C. M., Wakeford, H. R., Wilson, P. A., et al. (2014). Hubble space telescope hot jupiter transmission spectral survey: a detection of na and strong optical absorption in hat-p-1b. *Monthly Notices of the Royal Astronomical Society*, 437(1):46–66.

Nikolov, N. K., Sing, D. K., Spake, J. J., Smalley, B., Goyal, J. M., Mikal-Evans, T., Wakeford, H. R., Rustamkulov, Z., Deming, D., Fortney, J. J., et al. (2022). Solar-to-supersolar sodium and oxygen absolute abundances for a 'hot saturn'orbiting a metal-rich star. *Monthly Notices of the Royal Astronomical Society*, 515(2):3037–3058.

Nortmann, L., Pallé, E., Salz, M., Sanz-Forcada, J., Nagel, E., Alonso-Floriano, F. J., Czesla, S., Yan, F., Chen, G., Snellen, I. A., et al. (2018). Ground-based detection of an extended helium atmosphere in the saturn-mass exoplanet wasp-69b. *Science*, 362(6421):1388–1391.

Nugroho, S. K., Kawahara, H., Masuda, K., Hirano, T., Kotani, T., and Tajitsu, A. (2017). High-resolution spectroscopic detection of tio and a stratosphere in the day-side of wasp-33b. *The Astronomical Journal*, 154(6):221.

Öberg, K. I., Murray-Clay, R., and Bergin, E. A. (2011). The effects of snowlines on c/o in planetary atmospheres. *The Astrophysical Journal Letters*, 743(1):L16.

Ohno, K. and Kawashima, Y. (2020). Super-rayleigh slopes in transmission spectra of exoplanets generated by photochemical haze. *The Astrophysical Journal Letters*, 895(2):L47.

Parmentier, V., Fortney, J. J., Showman, A. P., Morley, C., and Marley, M. S. (2016). Transitions in the cloud composition of hot jupiters. *The Astrophysical Journal*, 828(1):22.

Parviainen, H. and Aigrain, S. (2015). Ldtk: limb darkening toolkit. *Monthly Notices of the Royal Astronomical Society*, 453(4):3821–3826.

Perryman, M., Hartman, J., Bakos, G. Á., and Lindegren, L. (2014). Astrometric exoplanet detection with gaia. *The Astrophysical Journal*, 797(1):14.

PHASE, C. (2003). Setting new standards with harps. *The Messenger*, 114:20.

Phillips, J. G. (1963). Otto struve 1897-1963. *Publications of the Astronomical Society of the Pacific*, pages 501–504.

Pollacco, D. L., Skillen, I., Cameron, A. C., Christian, D., Hellier, C., Irwin, J., Lister, T., Street, R., West, R. G., Anderson, D., et al. (2006). The wasp project and the superwasp cameras. *Publications of the Astronomical Society of the Pacific*, 118(848):1407.

Pollack, J. B., Hubickyj, O., Bodenheimer, P., Lissauer, J. J., Podolak, M., and Greenzweig, Y. (1996). Formation of the giant planets by concurrent accretion of solids and gas. *icarus*, 124(1):62–85.

Pont, F., Bouchy, F., Melo, C., Santos, N., Mayor, M., Queloz, D., and Udry, S. (2005). Doppler follow-up of ogle planetary transit candidates in carina. *Astronomy & Astrophysics*, 438(3):1123–1140.

Pont, F., Sing, D. K., Gibson, N. P., Aigrain, S., Henry, G., and Husnoo, N. (2013). The prevalence of dust on the exoplanet hd 189733b from hubble and spitzer observations. *Monthly Notices of the Royal Astronomical Society*, 432(4):2917–2944.

Prusti, T., De Bruijne, J., Brown, A. G., Vallenari, A., Babusiaux, C., Bailer-Jones, C., Bastian, U., Biermann, M., Evans, D. W., Eyer, L., et al. (2016). The gaia mission. *Astronomy & astrophysics*, 595:A1.

Quanz, S. P., Crossfield, I., Meyer, M. R., Schmalzl, E., and Held, J. (2015). Direct detection of exoplanets in the 3–10 $\mu$m range with e-elt/metis. *International Journal of Astrobiology*, 14(2):279–289.

Quanz, S. P., Schmid, H. M., Geissler, K., Meyer, M. R., Henning, T., Brandner, W., and Wolf, S. (2011). Very large telescope/naco polarimetric differential imaging of hd100546—disk structure and dust grain properties between 10 and 140 au. *The Astrophysical Journal*, 738(1):23.

Radica, M., Welbanks, L., Espinoza, N., Taylor, J., Coulombe, L.-P., Feinstein, A. D., Goyal, J., Scarsdale, N., Albert, L., Baghel, P., et al. (2023). Awesome soss: transmission spectroscopy of wasp-96b with niriss/soss. *Monthly Notices of the Royal Astronomical Society*, 524(1):835–856.

Rafikov, R. R. (2005). Can giant planets form by direct gravitational instability? *The Astrophysical Journal*, 621(1):L69.

Rajpaul, V., Aigrain, S., Osborne, M. A., Reece, S., and Roberts, S. (2015). A gaussian process framework for modelling stellar activity signals in radial velocity data. *Monthly Notices of the Royal Astronomical Society*, 452(3):2269–2291.

Redfield, S., Endl, M., Cochran, W. D., and Koesterke, L. (2008). Sodium absorption from the exoplanetary atmosphere of hd 189733b detected in the optical transmission spectrum. *The Astrophysical Journal*, 673(1):L87.

Rice, W., Armitage, P. J., and Hogg, D. (2008). Why are there so few hot jupiters? *Monthly Notices of the Royal Astronomical Society*, 384(3):1242–1248.

Ricker, G. R., Winn, J. N., Vanderspek, R., Latham, D. W., Bakos, G. Á., Bean, J. L., Berta-Thompson, Z. K., Brown, T. M., Buchhave, L., Butler, N. R., et al. (2015). Transiting exoplanet survey satellite. *Journal of Astronomical Telescopes, Instruments, and Systems*, 1(1):014003–014003.

Rustamkulov, Z., Sing, D., Mukherjee, S., May, E. M., Kirk, J., Schlawin, E., Line, M. R., Piaulet, C., Carter, A. L., Batalha, N. E., et al. (2023). Early release science of the exoplanet wasp-39b with jwst nirspec prism. *Nature*, 614(7949):659–663.

Samra, D., Helling, C., Chubb, K., Min, M., Carone, L., and Schneider, A. (2023). Clouds form on the hot saturn jwst ero target wasp-96b. *Astronomy & Astrophysics*, 669:A142.

Schlichting, H. E. (2014). Formation of close in super-earths and mini-neptunes: Required disk masses and their implications. *The Astrophysical Journal Letters*, 795(1):L15.

Schneider, J., Dedieu, C., Le Sidaner, P., Savalle, R., and Zolotukhin, I. (2011). Defining and cataloging exoplanets: the exoplanet. eu database. *Astronomy & Astrophysics*, 532:A79.

Seager, S. and Deming, D. (2010). Exoplanet atmospheres. *Annual Review of Astronomy and Astrophysics*, 48:631–672.

Seager, S. and Sasselov, D. D. (2000). Theoretical transmission spectra during extrasolar giant planet transits. *The Astrophysical Journal*, 537(2):916.

Sedaghati, E. (2017). Exploring alien skies: Detection and characterisation of exoplanetary atmospheres with ground-based transmission spectroscopy. *Ph. D. Thesis*.

Sedaghati, E., Boffin, H. M., Jeřabková, T., Muñoz, A. G., Grenfell, J. L., Smette, A., Ivanov, V. D., Csizmadia, S., Cabrera, J., Kabath, P., et al. (2016). Potassium detection in the clear atmosphere of a hot-jupiter-fors2 transmission spectroscopy of wasp-17b. *Astronomy & Astrophysics*, 596:A47.

Sedaghati, E., Boffin, H. M., MacDonald, R. J., Gandhi, S., Madhusudhan, N., Gibson, N. P., Oshagh, M., Claret, A., and Rauer, H. (2017). Detection of titanium oxide in the atmosphere of a hot jupiter. *Nature*, 549(7671):238–241.

Segura-Cox, D. M., Schmiedeke, A., Pineda, J. E., Stephens, I. W., Fernández-López, M., Looney, L. W., Caselli, P., Li, Z.-Y., Mundy, L. G., Kwon, W., et al. (2020). Four annular structures in a protostellar disk less than 500,000 years old. *Nature*, 586(7828):228–231.

Shporer, A. and Hu, R. (2015). Studying atmosphere-dominated hot jupiter kepler phase curves: evidence that inhomogeneous atmospheric reflection is common. *The Astronomical Journal*, 150(4):112.

Sing, D. K. (2018). Observational techniques with transiting exoplanetary atmospheres. *Astrophysics of Exoplanetary Atmospheres: 2nd Advanced School on Exoplanetary Science*, pages 3–48.

Sing, D. K., Fortney, J. J., Nikolov, N., Wakeford, H. R., Kataria, T., Evans, T. M., Aigrain, S., Ballester, G. E., Burrows, A. S., Deming, D., et al. (2016). A continuum from clear to cloudy hot-jupiter exoplanets without primordial water depletion. *Nature*, 529(7584):59–62.

Sing, D. K., Huitson, C. M., Lopez-Morales, M., Pont, F., Désert, J.-M., Ehrenreich, D., Wilson, P. A., Ballester, G., Fortney, J., Lecavelier des Etangs, A., et al. (2012). Gtc osiris transiting exoplanet atmospheric survey: detection of sodium in xo-2b from differential long-slit spectroscopy. *Monthly Notices of the Royal Astronomical Society*, 426(2):1663–1670.

Snellen, I., Albrecht, S., De Mooij, E., and Le Poole, R. (2008). Ground-based detection of sodium in the transmission spectrum of exoplanet hd 209458b. *Astronomy & Astrophysics*, 487(1):357–362.

Snellen, I. and Brown, A. (2018). The mass of the young planet beta pictoris b through the astrometric motion of its host star. *Nature Astronomy*, 2(11):883–886.

Snellen, I. A., De Kok, R. J., De Mooij, E. J., and Albrecht, S. (2010). The orbital motion, absolute mass and high-altitude winds of exoplanet hd 209458b. *Nature*, 465(7301):1049–1051.

Taylor, J., Radica, M., Welbanks, L., MacDonald, R. J., Blecic, J., Zamyatina, M., Roth, A., Bean, J. L., Parmentier, V., Coulombe, L.-P., et al. (2023). Awesome soss: atmospheric characterization of wasp-96 b using the jwst early release observations. *Monthly Notices of the Royal Astronomical Society*, 524(1):817–834.

Toomre, A. (1964). On the gravitational stability of a disk of stars. 139:1217–1238.

Traub, W. A. and Oppenheimer, B. R. (2010). *Direct imaging of exoplanets*. University of Arizona Press, Tucson.

Tsai, S.-M., Lee, E. K., Powell, D., Gao, P., Zhang, X., Moses, J., Hébrard, E., Venot, O., Parmentier, V., Jordan, S., et al. (2023). Photochemically produced so2 in the atmosphere of wasp-39b. *Nature*, 617(7961):483–487.

Tsapras, Y. (2018). Microlensing searches for exoplanets. *Geosciences*, 8(10):365.

Turrini, D., Schisano, E., Fonte, S., Molinari, S., Politi, R., Fedele, D., Panić, O., Kama, M., Changeat, Q., and Tinetti, G. (2021). Tracing the formation history of giant planets in protoplanetary disks with carbon, oxygen, nitrogen, and sulfur. *The Astrophysical Journal*, 909(1):40.

Vidal-Madjar, A., Sing, D. K., Des Etangs, A. L., Ferlet, R., Désert, J.-M., Hébrard, G., Boisse, I., Ehrenreich, D., and Moutou, C. (2011). The upper atmosphere of the exoplanet hd 209458 b revealed by the sodium d lines-temperature-pressure profile, ionization layer, and thermosphere. *Astronomy & Astrophysics*, 527:A110.

Wilson, P. A., Sing, D. K., Nikolov, N., Lecavelier des Etangs, A., Pont, F., Fortney, J., Ballester, G., López-Morales, M., Désert, J.-M., and Vidal-Madjar, A. (2015). Gtc osiris transiting exoplanet atmospheric survey: detection of potassium in hat-p-1b from narrow-band spectrophotometry. *Monthly Notices of the Royal Astronomical Society*, 450(1):192–200.

Winn, J. N., Fabrycky, D., Albrecht, S., and Johnson, J. A. (2010). Hot stars with hot jupiters have high obliquities. *The Astrophysical Journal Letters*, 718(2):L145.

Wolszczan, A. and Frail, D. A. (1992). A planetary system around the millisecond pulsar psr1257+ 12. *Nature*, 355(6356):145–147.

Wu, Y. and Murray, N. (2003). Planet migration and binary companions: The case of hd 80606b. *The Astrophysical Journal*, 589(1):605.

Wyttenbach, A., Ehrenreich, D., Lovis, C., Udry, S., and Pepe, F. (2015). Spectrally resolved detection of sodium in the atmosphere of hd 189733b with the harps spectrograph. *Astronomy & Astrophysics*, 577:A62.

Yan, F. and Henning, T. (2018). An extended hydrogen envelope of the extremely hot giant exoplanet kelt-9b. *Nature Astronomy*, 2(9):714–718.

Yip, K. H., Changeat, Q., Edwards, B., Morvan, M., Chubb, K. L., Tsiaras, A., Waldmann, I. P., and Tinetti, G. (2020). On the compatibility of ground-based and space-based data: Wasp-96 b, an example. *The Astronomical Journal*, 161(1):4.

Zieba, S., Kreidberg, L., Ducrot, E., Gillon, M., Morley, C., Schaefer, L., Tamburo, P., Koll, D. D., Lyu, X., Acuña, L., et al. (2023). No thick carbon dioxide atmosphere on the rocky exoplanet trappist-1 c. *Nature*, 620(7975):746–749.

# List of Figures